Development of Space Charge Measurement System for HVDC Cable and Joint Using Pulsed Electro-Acoustic Method

（パルス静電応力法による高圧直流ケーブルとジョイントに対する空間電荷計測システムの開発）

July, 2025

Doctor of Philosophy (Engineering)

SHAFIRA ZAHRA

シャフィラ ザラ

Toyohashi University of Technology

別紙４－１（課程博士（英文））

Date of Submission (month day, year) : 7/8/2025

Department of Electrical and Electronic Information Engineering		Student ID Number	D 229202	Supervisors	Yoshinobu Murakami Tomohiro Kawashima
Applicant's name	SHAFIRA ZAHRA				

Abstract（Doctor）

Title of Thesis	Development of Space Charge Measurement System for HVDC Cable and Joint Using Pulsed Electro-Acoustic Method

Approx. 800 words

The accumulation of space charges in polymeric insulation under high-voltage direct current (HVDC) conditions can distort the electric field, accelerate material degradation and lead to dielectric breakdown. Accurate space charge measurement is therefore essential for evaluating the reliability of HVDC insulation systems, especially in full-size power cables and accessories. Furthermore, in recent years, HVDC cables have become increasingly long to support long-distance power transmission. To achieve this, cable accessories such as joints are commonly used. However, the cable joint box, as a composite structure, is considered a potential weak point in the system. Thus, in the near future, space charge measurements in the joint box will become just as critical as that in the main body of the cable. Among various diagnostic techniques, the Pulsed Electro-Acoustic (PEA) method is widely employed due to its ability to directly measure space charge distributions under high DC stress.

In the application of PEA method, a coupling capacitor is generally used in the PEA method to superimpose a pulse voltage onto the insulation system already under high DC stress. However, for full-size cable specimens, the capacitor must be significantly large to withstand the applied high voltage, making pulse application challenging due to the cable specimen is normally as long as several meters and has large end-terminals. Moreover, this configuration introduces significant impedance and inductance between the pulse source and the specimen, which causes deterioration of the frequency characteristics of the applied pulse, leading to signal distortion and reduced measurement accuracy. Additionally, multiple reflections due to the distributed nature of the cable system can further complicate waveform interpretation. To overcome these limitations, this study proposes a method in which the cable itself serves as the pulse-coupling medium, eliminating the need for an external capacitor. In addition, in terms of accuracy improvement, the system utilizes and develops the newly proposed PEA cell, which achieves a four-fold increase in sensitivity compared to the conventional PEA cell, enabling better signal acquisition.

Based on previous improvement, a prototype PEA cell was developed by integrating the high-sensitivity polymer acoustic coupler with a 16-channel piezoelectric sensor array for space charge measurement in a cable joint model and the results will be analyzed through the signal processing required to convert the obtained waveforms into charge and electric field distributions, which can be used for further interpretation.

Chapter 1 provides background and overview of this study. Chapter 2 reviews the HVDC power transmission cable systems, space charge formation in solid polymer materials. Chapter 3 discusses how acoustic signals are generated and affected by factors such as geometry, attenuation, and dispersion during space charge measurement.

Chapter 4 discusses a method for applying pulse voltage using the cable itself as a pulse-coupling device, eliminating the need for an additional coupling capacitor. Furthermore, the conditions for accurate space charge measurement are evaluated in terms of frequency components, spatial resolution, and cable specimen length.

Chapter 5 presents the development of the newly designed PEA cell, incorporating a polymer acoustic coupler for enhanced acoustic transmission and electrical isolation. This improved cell was then applied to a full-size HVDC cable specimen with 20 mm insulation thickness using the method described in Chapter 4. Space charge measurements were conducted under DC voltages up to 50 kV. The results demonstrated that the electric field estimation error was less than 0.25 kV/mm, equivalent to 2% precision when scaled to a 250 kV operating voltage.

Chapter 6 describes the application of PEA cell in Chapter 5, incorporating a 16-channel piezoelectric sensor array cable joint model consisting of 6.6 mm XLPE and 11 mm EPDM insulation layers. Using deconvolution methods which takes into account for acoustic divergence, pulse field distribution, and attenuation, two-dimensional cross-sectional profiles of space charge, electric field, and potential were successfully visualized, revealing charge accumulation along the joint interface.

Chapter 7 presents a summary of the conclusions of this paper and future improvement of the study.

Table of Contents

List of Figures

List of Table

Chapter 1 Introduction

1.1. Background

Since the 1950s, high-voltage direct current (HVDC) cable systems have been used around the world to transmit electrical energy over long distances. Back then, the application was relatively limited mainly to very specific situations where alternating current (AC) systems weren't feasible, usually because of technical or economic constraints [1,2]. For example, submarine transmission was a classic use case as AC systems couldn't handle the reactive power losses that built up over long submarine cables, so DC became the more practical choice.

At the time, HVDC was a solution to a technical limitation—but today, the very features that once made it useful for niche cases have become crucial advantages in enabling a renewable-powered future.

In recent decades, the global energy landscape has undergone a major transformation. Driven by rising electricity demand, stricter environmental regulations, and the urgent need to combat climate change, countries are rapidly shifting from fossil fuels to renewable energy sources. This transition aligns with international goals such as the Paris Agreement in 2015 known as COP 21, driving the global shift toward renewable energy. However, one critical challenge remains for renewable energy, particularly offshore wind farms and remote solar power plants are often generated in remote locations, far from urban demand sites. Where the importance of long-distance transmission is highlighted in this scheme.

HVDC technology, once a niche solution, is now at the core of modern power transmission systems. In Europe, where national energy markets are becoming increasingly interconnected, HVDC enables the seamless transfer of renewable power across borders. A prime example is the Viking Link, a 1,400 MW HVDC interconnection between Great Britain and Denmark. Viking Link will transmit surplus energy to wherever the level of demand is higher. Because periods of high wind-energy production and high demand are unlikely to occur simultaneously in both Great Britain and Denmark.

The importance of cross-border interconnections is even more apparent for countries with limited natural resources. For instance, Singapore is turning to international energy cooperation to meet its growing demand. The Australia–Singapore Powerlink aims to deliver up to 6 GW of clean electricity from the largest renewable energy generation and battery storage hub in the Northern Territory through a 5,000 km HVDC transmission line.

So, what makes DC transmission interesting compared to AC transmission in this long-distance transmission?

One of the key advantages is efficiency. HVDC systems don't suffer from the same reactive power issues that AC systems do, especially over long distances. In HVDC transmission system there's no skin effect, no capacitive charging current and just lower-loss transmission. DC also allows for easier power flow control and disturbance management, which is particularly useful when integrating variable renewable sources such as offshore wind farms. And when voltage source converters (VSC) are used, HVDC systems can even provide reactive power support, further improving grid stability.

But HVDC isn't just about the main cables. To work reliably, these systems also depend on their accessories, particularly joints and terminations. Joints are required when the cable becomes too long to be produced in one length [3], and terminations are needed at the end of the cable circuit, as to connect the cable to substations or overhead lines. These accessories may seem secondary, but they're critical to overall system performance. In fact, Accessories may represent a weak point in HVDC cable links, especially when going to ever-higher voltages where feedback on in-service behavior is lacking [4].

At the core of both cables and their accessories is the insulation material. Historically, oil-impregnated paper insulation was the go to for HVDC systems [5]. It had a long track record of reliability, but it came with drawbacks, complex manufacturing, environmental concerns, and maintenance challenges. That led to the rise of extruded polymeric insulation, especially cross-linked polyethylene (XLPE). In comparison, where XLPE is lighter, easier to install, and more environmentally friendly. It doesn't require oil or fluid impregnation, making it a cleaner option with better mechanical properties.

However, like any technology shift, the move to polymeric insulation brought new challenges. One of the most critical is the issue of space charge accumulation [6,7].

Space charge refers to the buildup of electrical charges within the insulation material, not just on the surface. Under continuous DC voltage, these charges can become trapped or move very slowly, leading to significant distortion of the internal electric field. When this happens, the field can become uneven, with localized regions of high stress [8]. This may accelerate the aging of the insulation, and in worst cases, premature breakdown even when the applied voltage is well within the material's rated capacity.

This issue becomes even more complicated when we consider joints and terminations. These components aren't made of just one material they involve multiple dielectrics, adhesive layers, geometric transitions, and mechanical interfaces. All of these introduce discontinuities that make electric field behavior more unpredictable. The triple junctions, where different materials meet (like the interface between the main cable insulation, the joint insulation, and the semi-conductive layers), are especially prone to space charge buildup due to its complicated structure [9,10]. Unfortunately, the physics at this joint isn't yet fully understood, and small changes in material properties or geometry can lead to large differences in space charge behavior.

Although several reports have been published using computer simulations and experiments to measure and estimate the distribution of space charge in the insulation of HVDC cable joints, validation remain needed. In particular, almost no literature is available on joint insulation systems with axisymmetric two-dimensional structures, although some studies can be found on multilayer flat samples [11,12,13] and coaxial scaled joints without triple junctions. As a result, there's a growing need for direct measurement techniques that can observe and quantify space charge under real-world conditions, especially in full-size cables and joint systems.

This sets the stage for the next chapter of the work: how we can actually measure these space charges, understand their behavior, and use that knowledge to improve the design, monitoring, and lifetime prediction of HVDC systems.

1.2. Research Objective

The objective of this study is to develop a high-sensitivity PEA (Pulsed Electroacoustic) measurement system for evaluating the insulation performance of full-scale HVDC cables and joints. The main objective are:

- To establish a method that eliminates the need for an external coupling capacitor by utilizing the cable itself as a pulse coupler and analyzing how cable length influences waveform propagation to enable more practical and reliable measurements.
- To develop a new high-sensitivity PEA cell that is expected to have higher sensitivity over conventional PEA cell and conduct a study performing a space charge measurement in full size cable to evaluate the new PEA cell.
- Furthermore, to develop a 16-channel PEA array system for space charge measurement in cable joints.

The scope of the study covers system design, measurement methodology, and application to full-size cable and joint model.

1.3. Outline of the Thesis

The contents of each chapter are shown as:

Chapter 1, describes the background, objectives, and the outline of this study.

Chapter 2, provides an overview of dc power transmission cable systems, space charges formation and detection technique.

Chapter 3, provides a detailed explanation of the Pulsed Electro-Acoustic (PEA) method, including its operational principles, system design, and calibration approach. It also discusses how acoustic signals are generated and affected by factors such as geometry, attenuation, and dispersion during space charge measurement.

Chapter 4, this chapter discusses the challenges of applying the PEA method to full-size cables due to impedance and resonance effects caused by the specimen acting as a distributed element. A proposed solution eliminates the need for an external coupling capacitor by using the cable itself as a pulse coupler, and the chapter analyzes how cable length affects waveform propagation.

Chapter 5, introduces a newly developed PEA measurement cell that improves sensitivity for full-size cable testing by enhancing acoustic impedance matching using a polymer-based acoustic coupler and PVDF transducer and the application to the HVDC full-size cable as well as the signal processing to convert the acquired waveforms into charge and electric field distributions.

Chapter 6, described the developed design of the proposed PEA cell, which consists of a 16-sensor array and is adapted for the space charge measurement in cable joints, furthermore the signal processing is perform by introducing the second kind of deconvolution for calibrating the acoustic divergence, pulse stress distribution, attenuation and dispersion in cable joint.

Chapter 7, we presented the conclusions of this study along with the future recommendation for further study.

Reference

[1] G. Schmidt, B. Fiegl and S. Kolbeck, "HVDC transmission and the environment," Power Engineering Journal, vol. 10, no. 5, pp. 204-210, 1996.

[2] C. C. Diemonde, J. P. Bowles, V. Burtnyk, M. A. Lebow, E. G. Neudorf, D. Povh, E. C. Starr, C. W. Taylor, R. A. Walling, "AC-DC economics and alternatives-1987 panel session report," IEEE Transactions on Power Delivery, vol. 5, no. 4, pp. 1956-1979, 1990.

[3] J. Santana, F. Michel, S. Chupin, T. Bocquet, and M. Trefault, "HVDC & HVAC Cable Systems delivered on long length drums," presented at Jicable 2015, Paris, France, pp. 1–6, 2015.

[4] G. Teyssedre, T. T. N. Vu and S. L. Roy, "Electric Field Distribution in HVDC Cable Joint in Non-Stationary Conditions," 2021 IEEE International Conference on the Properties and Applications of Dielectric Materials (ICPADM), Johor Bahru, Malaysia, pp. 406-409, 2021.

[5] T. Katayama, T. Yamazaki, Y. Murata, S. Mashio and T. Igi, "Space charge characteristics in DC-XLPE cable after 400 kV PQ test," 9th International Conference on Insulated Power Cables (Jicable), Versailles, France, pp. 1-6, 2015.

[6] G. Mazzanti, G. Chen, J. C. Fothergill, N. Hozumi, J. Li, M. Marzinotto, F. Mauseth, P. Morshuis, C. Reed, A. Tzimas, K. Wu, "A protocol for space charge measurements in full-size HVDC extruded cables," IEEE Transactions on Dielectrics and Electrical Insulation, vol. 22, no. 1, pp. 21-34, 2015.

[7] Y. Zhou, W. Wang and T. Guo, "Space charge accumulation characteristics in HVDC cable under temperature gradient," Energies, vol. 13, no. 21, pp. 55-71, 2020.

[8] G. Chen, C. Zhou, S. Li and L. Zhong, “Space charge and its role in electric breakdown of solid insulation,” IEEE International Power Modulator and High Voltage Conference (IPMHVC), San Francisco, USA, pp. 120-127, 2016.

[9] L. A. Dissado and J. C. Fothergill, Electrical Degradation and Breakdown in Polymers, Peter Peregrinus, London, UK, 1992.

[10] B. Du (Ed.), Polymer Insulation Applied for HVDC Transmission; Springer: Singapore, 2021; ISBN 9789811597305.

[11] T. Tohmine, T. Fujitomi, H. Miyake, Y. Tanaka, Y. Ida and Y. Inoue, “Measurement of space charge accumulated in multi-layered samples composed of different insulators used in the joints of DC transmission cables,” 2017 International Symposium on Electrical Insulating Materials (ISEIM), Toyohashi, Japan, pp. 299-302, 2017.

[12] P. H. F. Bodega, Morshuis and J. J. Smit, “Space charge measurements on multi-dielectrics by means of the pulsed electroacoustic method,” IEEE Transactions on Dielectrics and Electrical Insulation, vol. 13, no. 2, pp. 272-281, 2006.

[13] T. T. N. Vu, G. Teyssedre, B. Vissouvanadin, S. L. Roy and C. Laurent, “Correlating conductivity and space charge measurements in multi-dielectrics under various electrical and thermal stresses,” IEEE Transactions on Dielectrics and Electrical Insulation, vol. 22, no. 1, pp. 117-127, 2015.

Chapter 2 HVDC Power Transmission Cable Systems, Space Charges Formation and Detection Technique

2.1. Introduction

High-voltage direct current (HVDC) transmission technology is increasingly adopted for long-distance power transmission due to its efficiency and stability advantages. HVDC cable systems, which form the backbone of these networks, rely heavily on the performance and reliability of their insulation materials. Electrical insulation failures in these systems can lead to severe malfunctions, making the integrity of the insulation crucial. This chapter begins by introducing the structure and components of HVDC cable systems. Over the years, as the power transported by DC links and their rated voltages have increased, cable systems have become longer, and AC/DC conversion technologies have evolved. Despite these advancements, mass impregnated and oil-filled insulation were the primary types used until 1999, when the first commercial HVDC polymeric cable system was deployed. Since then, polymeric cables have gained widespread use, and their adoption continues to grow. Next, we explore common failure phenomena in HVDC cable systems, with a particular focus on cable joints, where complex multilayer insulation structures are most prone to failure. Subsequently, the mechanisms of space charge formation within polymeric insulation are described as space charge accumulation is a key factor influencing the long-term reliability of polymeric HVDC cables. Finally, this chapter introduces various techniques used for measuring space charge distributions within HVDC cables, providing the foundation for the space charge measurement methods employed in the research.

2.2. AC and DC Power Transmission

AC and DC have become the most common transmission method nowadays. However, DC's widespread use began in 1882 when Pearl Street Station began supplying electric power to New York City's financial district using 30 km of underground cables. Despite this early success, DC's dominance was short-lived. As, George Westinghouse, Nikola Tesla, and others developed transformers and induction motors that made AC generation, transmission, and use superior. AC technology quickly became the dominant method for power generation, transmission, and distribution due to the simplicity of voltage conversion through transformers, minimal losses, and ease of maintenance [1,2].

Despite AC's dominance, HVAC transmission systems have several limitations that make DC transmission advantageous [~~3,~~3,4]. For instance, the inductive and capacitive properties of overhead wires and cables limit the transmission capacity and distance of AC systems [3]. For cables, the feasible transmission distance for

HVAC is typically between 40 to 100 km, depending on the system's power and voltage, but this is constrained by charging current [4]. Furthermore, HVAC transmission cannot connect two AC systems with different frequencies directly, and poor connections between two separate AC systems can result in instability or unfavorable power flow conditions.

As a result, high-voltage direct current (HVDC) transmission has emerged as a more efficient method for long-distance power transmission because it does not have problems such as skin effect on conductors, thus reducing energy losses. In addition, HVDC eliminates the need for reactive power compensation, making it more efficient for long-distance power transmission than AC systems. However, AC remains the standard for shorter distances due to its cost advantages, while HVDC systems are increasingly being used for submarine and long-distance transmission lines, such as the NEMO link, a joint venture between the National Grid in the UK and ELIA in Belgium.

Along with improvements in HVDC transmission technology, attention has shifted to the insulation materials used in HVDC cables. While traditional HVDC systems rely on oil-impregnated paper insulation, there is a growing shift, similar to that seen in AC cables, towards the use of polymer insulation due to its mechanical durability, ease of installation and environmental benefits. However, the transition to polymer HVDC cables presents new challenges, particularly those related to space charge accumulation, which can significantly affect dielectric performance and long-term reliability. Therefore, it is essential to obtain a deeper understanding of space charge behavior in polymeric insulation material to enable safe and reliable HVDC transmission.

2.3. HVDC Components: Cable and Accessories

HVDC cables are available in a range of designs, generally, it is determined by the cable insulation. The focus will be on high-voltage direct-current cables with extruded insulation, with a detailed examination of the cable structure. A brief description of various cable types (and their related insulations) will be presented. In general, the following HVDC cable typologies have been employed mainly in submarine or land-based HVDC power transmission systems [5,6,7]:

2.3.1. Mass Impregnated Nondraining (MIND) cables

At present, this cable type is used in most of HVDC applications. It consists of different layers, the composting layer are as follows:

1. Compressed or compact round conductors of copper or aluminum shaped wires;
2. Conductor semi-con of carbon-loaded paper;
3. Insulation, that is, pure cellulose paper impregnated with oil and resin;
4. Insulation semiconductive of carbon-loaded paper;
5. Metallic sheath;

6. Thermoplastic sheath;
7. Reinforcement of steel tapes (only for undersea cables);
8. Bedding (only for undersea cables);
9. Armor of steel flat wires (only for undersea cables).

Mass impregnated cable is a type of paper-oil-impregnated insulated cable, like OF cable. The conductor is shielded by oil and resin-impregnated papers; the resin provides non-draining qualities to the oil. The semiconductive conductor and insulation layers are made of carbon-loaded papers, whilst the outer layer is made of copper or aluminum tapes and/or woven fabrics. The fully impregnated cable is then lead sheathed to protect the insulation from the outside environment. The following layer is an anticorrosion layer made of extruded high-density polyethylene (HDPE).

It has track record of 500kV application and transmission capacities of up to 800 MW in a single cable, with installation depths of up to 1640 m below sea level and almost infinite transmission lengths [6,7,8]. The transmission capacity of mass-impregnated cables is constrained by the conductor temperature, the constant allowed conductor temperature is about 55˚C, which is lower than OF cable.

2.3.2. Oil-filled (OF) Cables

Fig. 2.1 Oil Filled HVDC Cable.

In comparison to mass-impregnated cables, the conductor is insulated by paper impregnated with a low-viscosity oil and contains a longitudinal channel allowing oil to flow along the cable. Additional levels are basically similar to those mentioned previously. Oil-filled cables are capable of withstanding both AC and DC voltages up to 600 kV DC. Due to the required oil flow along the cable, transmission line lengths are limited to 100 kilometers [6,7,8].

2.3.3. Polypropylene Paper Laminate (PPL, MI-PPL, PPLP)

HVDC systems with a voltage rating of 600 kV use cable systems that incorporate PPL insulation and nondraining impregnating chemicals, designed to operate at 80–90°C conductor temperatures [9]. These cables can withstand up to 60% more electrical stress, making them ideal for long, deep undersea cables. However, the technology is not yet widely established in DC systems [9].

Historically, paper-oil insulated cables dominated the HVDC market until the mid-1990s. Since then, manufacturers have shifted to extruded polymer insulation, primarily using polyethylene compounds, such as LDPE and XLPE (cross-linked polyethylene) [9,10,11,14,15,16]. DC-XLPE is the most common form of XLPE used in HVDC systems, and it is preferred for its performance under high-voltage direct current conditions. Polymeric insulation is better suited for higher operating temperatures compared to the older paper-oil insulation.

Fig. 2.2 XLPE insulated HVDC cable.

2.3.4. Cable Joint

A cable joint is defined as an insulated and fully protected connection between two or more cable sections, designed to restore the electrical, mechanical, and environmental properties of the original cable system. The main functions of a cable joint include:

1. Even distribution of electric field: To ensure reliable operation under all loading conditions, proper electric field grading is necessary to avoid excessive electric stress at insulation interfaces.
2. Elimination of voids: The joint must ensure intimate contact and eliminate voids at the interface between the cable insulation and the joint insulation body, as voids can lead to partial discharge and eventual failure.
3. Proper grounding: It is essential to provide continuity and grounding for the cable's metallic screen or sheath to safely carry charging and fault currents.
4. Mechanical and environmental protection: The joint should offer adequate protection against external mechanical damage and environmental factors (e.g., moisture, corrosion, contaminants).

High-voltage (HV) cable system joints can be categorized based on their installation context:

1. Factory joint (production joint): A joint between cable segments (extrusion lengths) created under controlled factory conditions, often during the manufacturing process of long-length cables.
2. Repair joint: A joint made to reconnect or replace a damaged cable section, typically installed in the field with full construction and repair materials.
3. Field joint (site joint): A joint assembled and installed on-site during initial cable installation, using pre-designed components to connect separate cable lengths in the field.

Prefabricated Joint

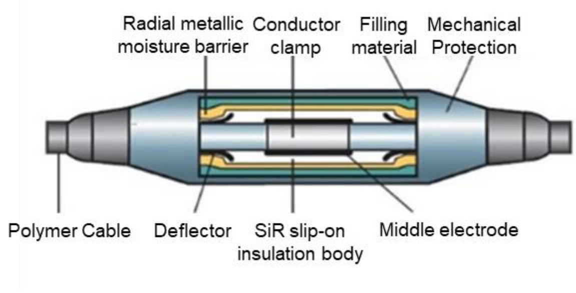

Fig. 2.3 Prefabricated joint design for HVDC land cable [29]. Reprinted with permission from © 2018 IEEE.

Cable joints come in a variety of configurations. for oil-impregnated and mass-impregnated cable joints and terminations are coiled with paper and impregnated in oil [17, 12]. At sea, the length of a cable segment can approach 100 kilometers due to the flexibility of large cable drums that can be transported on board. Factory joints are most frequently used in this situation for extruded submarine cables. Due to the limited transport capacity on land, the longest cable segment for land applications is less than 1 km. As a result, prefabricated joints are mostly used in land applications.

The prefabricated joint body composed of four different material layers which designed for HVDC (Fig. 2.3). The connector is electrically shielded by an inner deflector made of semi-conducting rubber. A continuous layer of field grading material (FGM) covers the joint body, even covering the inner deflector. Outside the FGM, an insulation of the rubber layer represents the actual joint insulation. Finally, the joint body's outer shield is composed of a semiconducting rubber screen.

Factory Joint

Typically, land cables require numerous prefabricated joints that are ready to be deployed in the field. The weight of the cable and transportation constraints limit the length of land cables that can be installed. On land, cable lengths are often shorter than in underwater installations.

Different reasons limit the length of undersea cables. They are determined by the ability to continually extrude high-quality cable over lengthy periods of time, as well as testing and storage capabilities. Installation lengths are ultimately determined by such parameters, which are under the control of the production site. As a result, flexible joints are commonly used to install joints at cable manufacturing (or factory joints) [13,14].

To employ larger cable lengths, intermediate couplings (factory joints) are required. Where an extrusion molded junction (EMJ) has been used to operate on reinforced insulation, the factory joint must be roughly the same diameter as the cable diameter.

2.3.5. Terminator

The HVDC extruded cable termination illustrated in [12] is a real combination of a conventional alternating current termination based on geometric field control with a continuous layer of FGM connecting the live electrode to the ground. The termination for 150 kV HVDC [extruded cable stated in [12] is a flexible dry type composed of separate rubber parts, including top sealing, weather-sheds, field grading adapters (FGA), and a stress relief cone. Due to the termination's design, it can be used on practically any size of cable. Additionally, the creepage distance can be adjusted easily by adjusting the amount of weather sheds and FGAs.

2.4. HVDC Cable System Failure Phenomena

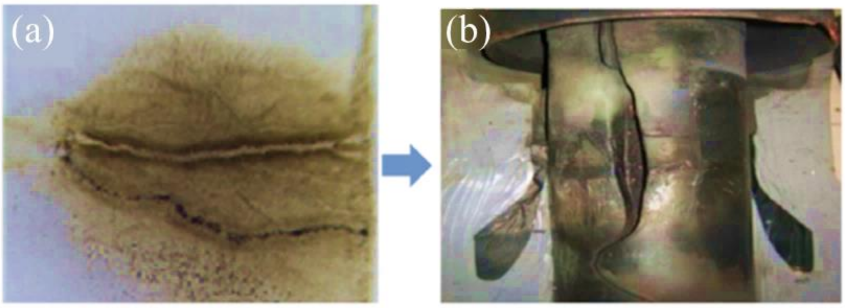

Fig. 2.4 (a) surface discharge along the interface of cross-linked polyethylene (XLPE)/ silicone rubber (SiR), and (b) breakdown caused by surface discharge [15]. Reprinted with permission from © 2024 Wiley Periodicals LLC.

Failures in HVDC cable systems often occur at interfaces, particularly in cable joints where multiple insulation layers meet. Fig. 2.4 (a) surface discharge along the interface of cross-linked polyethylene (XLPE)/ silicone rubber (SiR), and (b) breakdown caused by surface discharge [15] illustrates an example of (a) surface discharge along the interface of cross-linked polyethylene (XLPE) and silicone rubber (SiR), and (b) breakdown caused by the surface discharge [15].

Such failures are typically attributed to complex multilayer insulation coordination issues, because space charge tends to accumulate on the interfaces between the various insulating and semi conductive layers which compose HVDC cable joints, distorting the electric field distribution and fostering an increased aging and possibly premature failure of the joint [16,17].

Understanding the mechanisms of space charge formation and its impact on insulation degradation is therefore critical for improving the reliability of HVDC cable systems. In the following sections, space charge behavior in polymeric insulation and relevant detection techniques will be discussed.

2.5. Space Charge Formation in Polymer Insulation

Space charge refers to the accumulation of charge carriers (electrons or ions) within an insulating material under DC stress [16,18,19,20,]. It is an important phenomenon in high voltage direct current (HVDC) cable insulation systems, especially in polymeric materials, where even a weak electrical conduction could lead to charge movement and accumulation under prolonged electrical stress.

At high electric fields, space charge can enter the insulation rapidly, even at room temperature. Once formed, it may take several hours to decay after the applied voltage is removed. The accumulated charge does not disappear immediately; instead, it gradually dissipates depending on factors such as the type of insulation material and the temperature. Polymeric insulation generally retains charges longer than traditional lapped insulation. The dynamics of space charge accumulation can be described using the continuity equation for current density:

$$\nabla \cdot j + \frac{\partial \rho}{\partial t} = 0 \tag{2.1}$$

Where, j is the current density, ρ is the charge per unit volume (space charge density), and t is time. This equation implies that any imbalance between the inflow and outflow of charges within a region leads to charge accumulation.

The resulting space charge field, denoted as E_ρ, is related to the charge distribution according to Gauss's theorem:

$$\rho = \nabla \cdot (\varepsilon_0 \varepsilon_r E_\rho) \tag{2.2}$$

where ε_0 is the vacuum permittivity and ε_r is the relative permittivity of the insulating material.

Therefore, the total electric field E within the insulation in the presence of space charge is the sum of two components the external field E_0 (also called Laplacian field) induced by the applied voltage, and the space charge field E_ρ , as described in Equation (1.3):

$$E = E_0 + E_\rho \tag{2.3}$$

The accumulation of space charge within the insulation contributes to electric field distribution. The space charge introduces an additional electric field that superimposes on the externally applied field, leading to the field enhancement at certain location in the insulation. in some case, this contribution may high enough to initiate a breakdown. This makes space charge could be the contributor to the electrical aging process in polymeric insulation systems [21].

2.6. Space Charge Detection Technique

According to the IEEE 1732-2017 standard, the recommended techniques for space charge measurement in full-size cables are the Thermally Step Method (TSM) method and the Pulsed Electroacoustic (PEA) method. These techniques are described as follows:

2.6.1. Thermal Step Method (TSM)

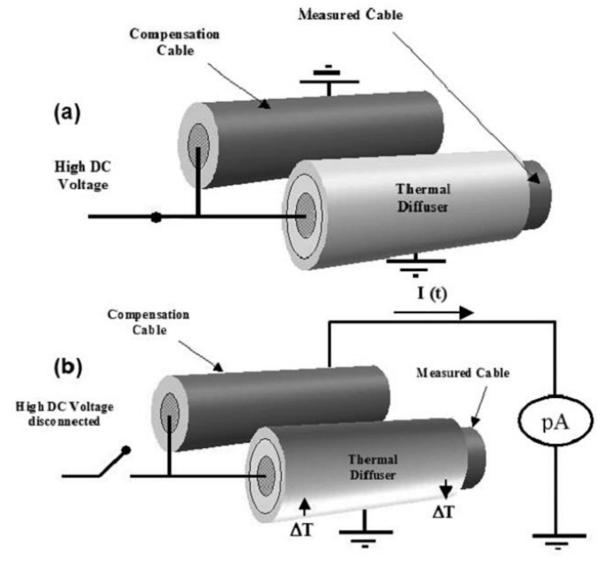

Fig. 2.5 Experimental setup for TSM under short circuit conditions [28], © 2009, IEEE.

The thermal step method (TSM) is a thermal space charge measurement technique that has been used since around 1986 [23]. Since TSM is a nondestructive methodology for determining how the electric field and space charge density are distributed over solid insulating materials. The thermal step method (TSM) is based on the propagation of a thermal wave that causes a transient local displacement in the space charge. A change in the induced charges at the electrodes reflecting it. Thus, allowing the distribution of the residual electric field and charge density throughout the sample to be determined. TSM is used on any sample with a geometry that allows the spatiotemporal temperature distribution to be computed, such as material specimens and industrial components (power cables, capacitors, printed boards, and stator windings) [26]. Since the thermal step method can be applied to cylindrical cables, it has become one of the most promising methods for non-destructive space charge measurement of full-scale cables [24].

The thermal step method usually uses heating of one sample side compared to the other by applying a constant temperature differential between the two electrodes by using a brief (100ms) laser pulse or a modulated light beam, respectively, to illuminate (and therefore heat) the absorbing sample electrode [25]. Fig. 2.5 shows the principal diagram of the thermal step method. An insulating sample is sandwiched between two electrodes. When a temperature difference of ΔT is applied to the insulating sample, a thermal wave propagates, causing a local displacement of the space charge. Since the sum of all the charges is zero, this local charge displacement generates an induced charge on the electrode. This method measures the space charge by short-circuiting two electrodes across an insulating sample and detecting the change in induced charge by measuring the current.

2.6.2. Pulse Electroacoustic (PEA) Method overview

[28] proposed the pulsed electro acoustic method. The resolution is greater, and the lowest detectable charge density is lower (higher sensitivity) than other space charge measurement methods, making it one of the most widely used space charge measurement methods today. The pulsed electro acoustic technique has been used to assess the space charge of full-size power cables, with varied study results [23].

The pulse electroacoustic method is illustrated in Fig. 2.6. To charge the insulating sample, an insulating sample is placed between electrodes and a DC voltage V DC is applied between the electrodes [26].

The PEA Method concepts is based on the Coulomb force law, which states: In the presence of resident charges, an externally applied pulse field generates a perturbing force density on the material. The charged bulk creates an acoustic wave as a result of the disturbance. A piezoelectric transducer placed on one of the electrodes then detects the acoustic signal [27]. Digital signal processing is used to extract and calibrate the space-charge profile information included in the outgoing acoustic signal. Deconvolution is used to extract the charge density distribution from the voltage signal. It should be noted that the acoustic wave is internally generated by the space charge in contrast to the pressure wave propagation methods where the pressure wave is generated externally.

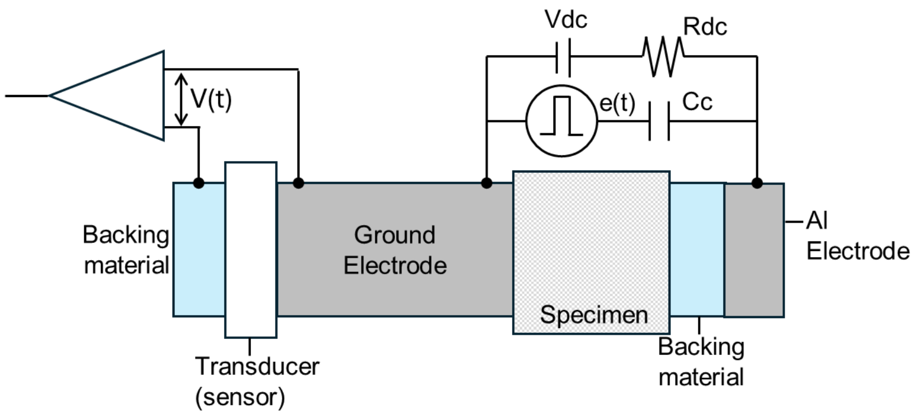

Fig. 2.6 Block diagram of the pulsed electroacoustic (PEA) method.

2.7. Summary

This chapter provides a comprehensive overview of HVDC power transmission systems with a focus on cable technologies, failure mechanisms, and space charge phenomena. It begins by contrasting AC and DC power transmission, highlighting the historical development and technical advantages that have led to the modern use of HVDC systems. The chapter then explores key components of HVDC cable systems, including various insulation technologies such as Mass Impregnated Non-Draining (MIND) cables, oil-filled cables, and polymer-based lapped thin-film cables. Accessories like cable joints and terminators are also introduced.

The chapter then shifts focus to the formation of space charges in polymer insulation, an issue critical to the long-term reliability of HVDC cables. Finally, it outlines several techniques for detecting space charges, including the Thermal Step Method (TSM) and the Pulse Electroacoustic (PEA) method, providing an overview of their principles and applications.

Reference

[1] E. Uhlman. Power Transmission by Direct Current. Springer, Berlin/Hiedelberg, 1975.

[2] W. Long and S. Nilsson, "HVDC transmission: yesterday and today," IEEE Power and Energy Magazine, vol. 5, no. 2, pp. 22-31, 2007.

[3] M. Guarnieri, "The Alternating Evolution of DC Power Transmission," IEEE Industrial Electronics Magazine, vol. 7, no. 3, pp. 60–63, 2013.

[4] M. Ramamoorty, "High voltage direct current transmission," Journal of the Institution of Engineers (India): Electrical Engineering Division, vol. 70, no. 2–3, pp. 97–103, 1989.

[5] M.P. Bahrman and B.K. Johnson, "The ABCs of HVDC Transmission Technologies," IEEE Power and Energy Magazine, vol. 5, no. 2, pp. 32–44, 2007.

[6] T. Worzyk. Submarine Power Cables. Springer, Berlin, pp. 9-50, 2009.

[7] Ray Bartnikas; K. D. Srivastava, "Design and Manufacture of Oil Impregnated Paper Insulated Power Distribution Cables," in Power and Communication Cables: Theory and Applications , IEEE, pp.243-275, 2000.

[8] E. Stern, J. Nash, C. Schoeniger, C. Bartzsch, G. Acquaotta, M. Bacchini, and A. Orini, "The Neptune Regional Transmission System 500 kV HVDC Project," CIGRE Session, Paris, France, Paper B4-118, pp. 1–8, 2008.

[9] EPRI Report No. 1008720. "DC Cable Systems with Extruded Dielectrics," Palo Alto, California, December 2004.

[10] M. Salah Khalil, "International Research and Development Trends and Problems of HVDC Cables with Polymeric Insulation," IEEE Electrical Insulation Magazine, vol. 13, no. 6, pp. 35–47, November–December 1997.

[11] R R.N. Hampton, "Some of the Considerations for Materials Operating under High-Voltage, Direct-Current Stresses," IEEE Electrical Insulation Magazine, vol. 24, no. 1, pp. 5–13, 2008.

[12] T. Sorqvist, T. Christen, M. Jeroense, V. Mondiet, and R. Papazyan, "HVDC light cable systems-highlighting the accessories," In Proceedings of the 21st Nordic Insulation Symposium (NORDIS 2009), Gothenburg, Sweden, pp. 15-17. 2009.

[13] K. Terashima, H. Suzuki, M. Hara, K. Watanabe, "Research and Development of +/-250 kV DC XLPE Cables," IEEE Transactions on Power Delivery, Vol.13, No.1, pp.7-16, 1998.

[14] K. Terashima, H. Sukuki, M. Hara and K. Watanabe, "Research and development of /spl plusmn/250 kV DC XLPE cables," IEEE Transactions on Power Delivery, vol. 13, no. 1, pp. 7-16, 1998.

[15] T. Zhang, Y. Zhang, X. Zheng, W. Lin, Z. Zhang, Z. Chi, J. Zhang, and C. Teng, "Mechanistic insights into the thermal–mechanical aging of the interface of cross-linked polyethylene/silicone rubber," Journal of Applied Polymer Science, vol. 141, no. 12, pp. 1–10, 2024.

[16] Dissado, L.A.; Fothergill, J.C. Electrical Degradation and Breakdown in Polymers; Peter Peregrinus: London, UK, 1992.

[17] Du, B. (Ed.) Polymer Insulation Applied for HVDC Transmission; Springer: Singapore, 2021; ISBN 9789811597305.

[18] N. Yoshifuji, Y. Suzuoki, S. Han, Y. Matsukawa, T. Furuta, H. Yamada, T. Mizutani and M. Ieda, "Study of space-charge characteristics in polyethylene for power cable insulation by laser-induced pressure-pulse technique," Electrical Engineering in Japan, vol. 112, no. 7, pp. 33–45, 1992.

[19] Y. Li, M. Yasuda and T. Takada, "Influence on spatial charge distribution of cross-linking agents," in Proc. 3rd Int. Conf. Prop. Appl. Diel. Mater., Tokyo, Japan, pp. 1210–1213,1991.

[20] F. H. Kreuger, Industrial High Voltage - Part II. Delft, The Netherlands: Delft Univ. Press, 1992.

[21] H. Kon, Y. Suzuoki, T. Mizutani, M. Ieda and N. Yoshifuji, "Packet-like space charges and conduction current in polyethylene cable insulation," IEEE Transactions on Dielectrics and Electrical Insulation, vol. 3, no. 3, pp. 380-385, 1996.

[22] N.H. Ahmed and N.N. Srinivas. "Review of Space Charge Measurements in Dielectrics," IEEE Transactions on Dielectrics and Electrical Insulation, Vol. 4, No. 5, pp. 644–656, 1997.

[23] Cherifi, M. Abou Dakka, and A. Toureille. "The Validation of the Thermal Step Method," IEEE Transactions on Electrical Insulation, Vol. 27, No. 6, pp. 1152–1158, 1992.

[24] P. Notingher, Jr. S. Agnel, and A. Toureille. "Thermal Step Method for Space Charge Measurements under Applied DC Field," IEEE Transactions on Dielectrics and Electrical Insulation, Vol. 8, No. 6, pp. 985–994, 2001.

[25] G.M. Sessler. "Charge Distribution and Transport in Polymers," IEEE Transactions on Dielectrics and Electrical Insulation, Vol. 4, No. 5, pp. 614–628, 1997.

[26] T. Takada. "Acoustic and Optical Methods for Measuring Electric Charge Distributions in Dielectrics," IEEE Transactions on Dielectrics and Electrical Insulation, Vol. 6, No. 5, pp. 519–547, 1999.

[27] T. Takada, T. Maeno, and Kushibe. "An Electric Stress-Pulse Technique for the Measurement of Charges in a Plastic Plate Irradiation by an Electron Beam," IEEE. Trans. Electr. Insul., Vol. 22, No. 4, pp. 497–501, 1987.

[28] C. Stancu, P. V. Notingher, F. Ciuprina, P. NotingherJr., J. Castellon, and S. Agnel, "Computation of the Electric Field in Cable Insulation in the Presence of Water Trees and Space Charge," IEEE Transactions on Industry Applications, vol. 45, no. 1, pp. 30-43, 2009.

[29] H. Ye, Z. Han, Y. Luo, Q. Zhuang, T. Fechner, H. Wang, "Design aspects on HVDC cable joints," 2018 12th International Conference on the Properties and Applications of Dielectric Materials (ICPADM), Xi'an, China, pp. 300-304, 2018.

Chapter 3 Pulse Electro Acoustic Method

3.1. Introduction

Building upon the general overview provided in Chapter 2, this chapter presents the working principle, design, and implementation of the Pulse Electro-Acoustic (PEA) method, as well as the data processing and calibration methods used in this study. Emphasis is placed on understanding acoustic generation and propagation, including the effects of geometry, attenuation, and dispersion on the acoustic signals. While this chapter focuses on the fundamental aspects of the PEA method, the application of the PEA system and the advanced signal processing techniques for full-size cable and joint models will be discussed in Chapters 5 and 6, respectively.

3.2. Overview of the PEA Measurement System

This section introduces the core configuration of the Pulsed Electroacoustic (PEA) method and the essential components of the measurement system, especially in its application to the geometrical systems.

In the pulsed electroacoustic method, consisting of devices are DC power supply, pulse generator, and measurement cell. The measurement cell itself includes several components such as :

1. **Coupling electrodes**: as the acoustic coupler and placed to connect the surface of the specimen (or cable) to the piezoelectric sensor directly and also serve as a delay line.
2. **Piezoelectric sensor**: Made of thin PVDF (polyvinylidene fluoride) film, which converts the acoustic pressure wave into an electrical signal.
3. **Backing material**: Usually made of PMMA (polymethyl methacrylate) or another material with matching acoustic impedance. Ensuring the signal propagation from the sensor (in conventional PEA). Enhancing the sensor response by reflecting acoustic waves (new PEA cell)
4. **Amplifier and signal acquisition**: The electrical signal from the piezoelectric sensor is amplified and captured on a device like an oscilloscope.

Fig. 3.1 shows a simplified diagram of the space charge measurement setup for a full-scale HVDC cable. The cable consists of the central conductor, insulation, inner and outer semi-conducting layers, and is firmly held against the A1ground electrode. Guard electrodes are placed around the main measuring region to ensure uniform electric field application during pulse excitation. In addition, due to the usage of pulse voltage application for long cables, and the coupling electrode made of aluminum. An optical link is utilized in measurement to properly separate the electronics device.

The DC voltage source V_{dc} is connected to the cable conductor through the A bias resistor R_{DC} while, pulse voltage is applied directly to the measured section of the cable's outer semiconducting layer. Further discussion regarding pulse voltage application is provided in Chapter 4. Whilst, beneath the cable is the PEA cell, an aluminum electrode detects the pressure waves generated by the vibration of charges inside the insulation. This electrode is connected to a piezoelectric transducer, and the signals are then transmitted to an absorber.

The PEA method is based on detecting pressure (acoustic) waves which are generated by the vibrations of charge carriers inside dielectric materials when a superimposed pulse voltage is applied across electrodes. When the pulse is applied, the charge-induced pressure wave propagates through the dielectric reaches a metallic grounded electrode in contact with a piezoelectric sensor. The sensor then converts the mechanical wave into an electrical signal, which can be amplified and recorded.

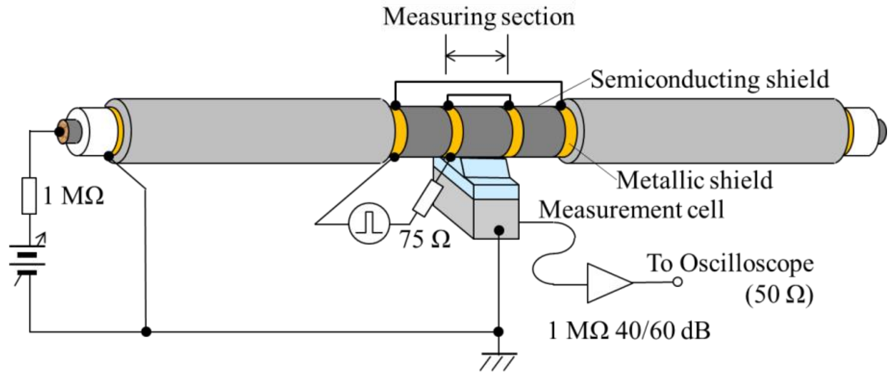

Fig. 3.1 Space charge measurement by means of PEA method in the cable.

3.3. Signal Propagation and Wave Behavior

3.3.1. Acoustic Wave Generation

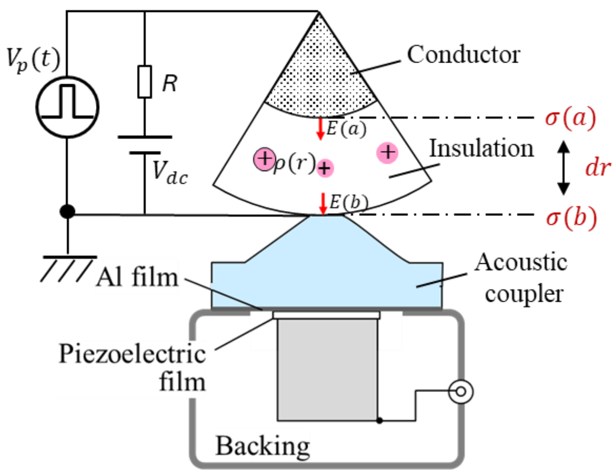

Fig. 3.2 PEA method principle for coaxial cable sample.

The application of the pulse leads to a modification of the electrostatic force distribution [1]. Fig. 3.2 shows the method for a cable specimen, the inner and outer interface between the insulation and semicon layer are a and b respectively. with thickness dr has the element space charge $\rho(r)dr$.

If a DC voltage V_{dc} is applied between both electrodes, surface charges induced on the electrodes by electric field between both electrodes, surface charges are induced on the electrodes by electric field E and the static Maxwell stress f_{mw} generated on electrodes is expressed as :

$$f_{mw} = \frac{1}{2}\varepsilon E^2 = \frac{1}{2}\varepsilon\left(\frac{V_{dc}}{r\ \ln(b/a)}\right)^2 \tag{3.1}$$

Whereas according to Lorentz law, (3.2) shows the force $\Delta f(r,t)$ induced by the pulsed electric field on the space charge ρ(r) at position dr is

$$\Delta f(r,t) = e_p(t,r)\rho(r)dr \tag{3.2}$$

where $e_p(t,r)$ is the applied pulse electric field varies through the thickness of the insulation and is expressed as

$$e_p(t,r) = V_p(t)/(r\ ln(b/a)) \tag{3.3}$$

where $V_p(t)$ is the applied pulse voltage.

In the Fig. 3.2 charges $\sigma(a)$ and $\sigma(b)$ which represent the induced surface charge at the interface between insulation and semiconducting layer given by:

$$\sigma(a) = \varepsilon_0\varepsilon_r E(a) \tag{3.4}$$

$$\sigma(b) = \varepsilon_0\varepsilon_r E(b) \tag{3.5}$$

Where $E(a)\ and\ E(b)$ are the total static interfacial electric stress at a and b, which are distributed to the applied dc voltage and the accumulated space charge in the bulk insulation. $\varepsilon_0\varepsilon_r$ are vacuum permittivity and relative permittivity, respectively. And the pulsed forced acting on this charge layer:

$$f(a,t) = \sigma(a)e_p(t,a) + \frac{1}{2}\varepsilon_0\varepsilon_r {e_p}^2(t,a) \tag{3.6}$$

$$f(b,t) = \sigma(b)e_p(t,b) + \frac{1}{2}\varepsilon_0\varepsilon_r {e_p}^2(t,b) \tag{3.7}$$

3.3.2. Acoustic Wave Propagation

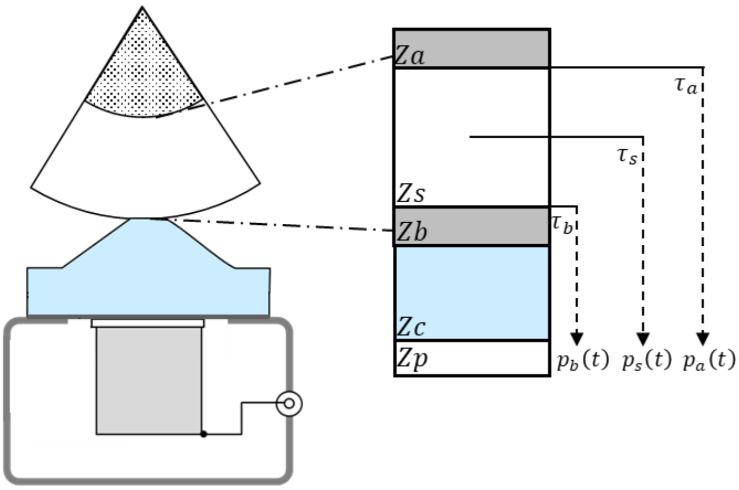

Fig. 3.3 The propagation of acoustic wave in coaxial geometry cable by means of PEA method.

During the application of the pulse voltage, the force from induced charges and space charge will result in the charge layers moving slightly. This movement launches acoustic waves that propagate in both directions, one towards the electrode and the transducer and another in the opposite direction, however only toward the piezo transducer is considered in the calculation. The acoustic waves arriving at the transducer will be detected on the other hand the opposite direction will not reach the sensor, unless they are reflected at the interface between two different media depending on the acoustic impedance. The acoustic impedance denotes as :

$$Z = \delta v \tag{3.8}$$

where δ and v are density and acoustic velocity of material, respectively. The acoustic waves arriving at the transducer are represented by $p_a(t),\ p_b(t),\ p_s(t)$, which correspond to the acoustic signals generated by the surface charge at electrode a, the bulk space charge, and the surface charge at electrode b, respectively.

$$p_a(t) = K_a \frac{\sigma(a)\, V_p(t-\tau_a)}{(a)^{1/2} ln\,(\frac{b}{a})} \tag{3.9}$$

$$p_b(t) = K_b \frac{\sigma(b)\, \mathrm{V_p}(\mathrm{t}-\tau_b)}{(b)^{1/2}\ln\left(\frac{b}{a}\right)} \tag{3.10}$$

$$p_s(t) = \frac{K_s}{ln\left(\frac{b}{a}\right)} \int_a^b \frac{\rho(r)}{r^{1/2}} V_p(t-\tau_s)dr \tag{3.11}$$

τ_a, τ_b, τ_s represent the time required by the acoustic wave initiated at each charge layer to reach the piezo electric sensor as shown at Fig. 3.3. The terms of $(a)^{1/2}$and $(b)^{1/2}$ in the equation derived from the effects of the cylindrical attenuation of the acoustic wave propagating through the cylindrical geometry. K is the transmission coefficient experienced while propagating and is expressed as

$$K_a = \frac{Zs}{Zs + Za} \cdot \frac{2Zb}{Zb + Zs} \cdot \frac{2Zc}{Zc + Zb} \cdot \frac{2Zp}{Zp + Zc} \tag{3.12}$$

$$K_b = \frac{Zb}{Zb + Zs} \frac{2Zc}{Zc + Zb} \cdot \frac{2Zp}{Zp + Zc} \tag{3.13}$$

$$K_s = \frac{Zb}{Zb + Zs} \cdot \frac{2Zc}{Zc + Zb} \cdot \frac{2Zp}{Zp + Zc} \tag{3.14}$$

Where *Za* is the acoustic impedance of the outer semiconductor at point *a, Zs* is the acoustic impedance of the cable insulation, *Zb* is the impedance of the outer semiconductor at point *b*, *Zc* is the impedance of the acoustic coupler, and *Zp* is the impedance of the PVDF sensor as shown at Fig. 3.3. Therefore, the total sound wave $p(t)$ is expressed as in Equation 3.15, which is the sum of all acoustic waves.

$$p(t) \ = \ p_a(t) + p_s(t) + p_b(t) \tag{3.15}$$

3.4. Effect of the Cylindrical Geometry and propagation to the Amplitude of Acoustic Wave

The thickness of the specimen and the geometry of the object being tested significantly influence the resolution and accuracy of the PEA measurements. Thicker materials or larger cable geometries can lead to signal attenuation, as the pressure wave must travel through a greater distance, which could reduce the intensity of the detected signal, the application of correction process is discussed in Chapter 5 and Chapter 6, whereas the following subchapter is discussing the effect of the cylindrical geometry and correction in general.

3.4.1. Cable Geometry Divergence

In coaxial geometries, it is required to correct the measured signal due to the divergence at the applied electric field $e_p(r)$ from the pulsed voltage across the sample, the electric stress for the coaxial geometry given by:

$$e_p(r) = \frac{V_p}{r \ ln(r_o/r_i)} \tag{3.16}$$

where r_o and r_i are the positions of the outer and inner screen electrodes, V_p is the applied pulse voltage. Whereas the electric stress decreases across the insulation from the inner to the outer electrode in the PEA method, thus with the variation of electric stress, the space charge density near the inner electrode will give a higher acoustic signal than the outer electrode, meaning the space charge distribution will be position dependent.

Divergence of pulse field

As the space charge only changes in the radial direction, which result in a reduction in signal intensity during the propagation to the outer sheath from the divergence of the pulsed field, the correction factor Kp can be defined as:

$$K_p = \frac{e_p(r)}{e_p(r_{out})} = \frac{r_o}{r} \tag{3.17}$$

Divergence of acoustic charge

Since the charge density is inversely proportional to the distance, the charge induced on the radius is $\frac{r_o}{r}$ greater than that on the outer screen shown as,

$$K_m = \frac{q_r}{q_0} = \frac{r_o}{r}$$

Divergence of acoustic waves

The amplitude of the acoustic waves detected at the sensor is smaller than the amplitude of the wave at the space charge location. Which, the acoustic waves magnitude reduces with the square root of the radius as they propagate towards the acoustic sensor. In order to correct the detected signal from the divergence of the acoustic waves, it written as:

$$K_g = \sqrt{\frac{r}{r_o}} \tag{3.18}$$

Geometrical correction factor

By combining all the divergence factor K_p, K_m, K_g, the total geometric divergence correction factor K_{div} is the combination of the divergence define as:

$$K_{div}(r) = \frac{r_o}{r} . \frac{r_o}{r} . \sqrt{\frac{r}{r_o}} = \frac{{r_o}^{3/2}}{r} \tag{3.19}$$

3.4.2. Acoustic Attenuation and Dispersion

As previously mentioned, in the PEA method, the measured space charge signal is obtained from acoustic waves generated due to their interaction with a transient electric field. These acoustic waves propagate across different materials before reaching the acoustic transducer. When the acoustic wave generated by inner screen propagates to outer, the amplitude of acoustic wave decreases, and its width widens. Whereas, in dielectric sample materials generally consist of lossy materials which attenuate and disperse the pressure waveform as it propagates. The expression for a planar acoustic wave $p(x,t)$ propagating through a lossy and dispersive medium can be represented as [2,3,4,9]:

$$p(x,t) = P(0,\omega)\exp(-\alpha(\omega)x)\exp(-j\beta(\omega)x) \qquad (3.20)$$

where $P(0,\omega)$ is the is magnitude of the pressure wave component at the location *x=0* (before losses), $\alpha(\omega)$ and $\beta(\omega)$ correspond to the attenuation factor and dispersion factor respectively. During propagation, $\alpha(\omega)$ cause a decrease in wave magnitude while it travels through the medium, whereas $\beta(\omega)$ affects wave speed and waveform shape. This results in the broadening of the acoustic wave, as different frequency components travel at different velocities express as:

$$\beta = \frac{c}{\omega} \qquad (3.21)$$

As, ω is the angular frequency, sound velocity *c* and phase coefficient β. By application of the fourier transform, equation (3.19) in cylindrical coordinate is transformed into:

$$p(r,\omega) = P(\omega,r_i)\exp\big(-\alpha(\omega)(r-r_i)\big)\exp(-j\beta(\omega)(r-r_i)) \qquad (3.22)$$

where $p(r,\omega)$and $P(r_i,\omega)$ are Fourier transforms of the acoustic wave at r_i and r, respectively. r can be varied from r_i to r_o, which also represent the position at the inner screen and outer screen respectively. In order to calculate the coefficients $\alpha(\omega)$ and $\beta(\omega)$*)*, the acoustic waveform at two different locations of the sample will be used. Generally, the acoustic wave generated at the $r = r_o$ and $r = r_i$ are used [4,6,10]. In this particular case acoustic transfer function *H* at *r* given by:

$$H(\omega,r) = \frac{P(\omega,r)}{P(\omega,r_i)} = \exp\big(-\alpha(\omega)(r-r_i)\big)\exp(-j\beta(\omega)(r-r_i)) \qquad (3.23)$$

Whereas, $r = r_o$ given by:

$$H(\omega,r_o) = \frac{P(r_o,\omega)}{P(r_i,\omega)} = \exp\big(-\alpha(\omega)(r_o-r_i)\big)\exp(-j\beta(\omega)(r_o-r_i)) \qquad (3.24)$$

$\alpha(\omega)$ and $\beta(\omega)$ can be derived from the following relations (which consider the geometric divergence):

$$\exp\big(-\alpha(\omega)(r_o-r_i)\big) = |H(r_o,\omega)| \Rightarrow \alpha(\omega) = -\frac{1}{r_o-r_i} ln\left|\frac{P(\omega,r_o)}{P(\omega,r_i)*\sqrt{r_i/r_o}}\right| \qquad (3.25)$$

$$\beta(\omega) = \phi\big(H(r_o,\omega)\big) \Rightarrow \beta(\omega) = \frac{1}{r_o-r_i}|\phi(\omega,r_o)-\phi(\omega,r_i)| \qquad (3.26)$$

where $\sqrt{r_i/r_o}$ correction factor in Equation (3.19) and $\phi(\omega, r_i)$ and $\phi(\omega, r_o)$ are the phase for the acoustic wave at the inner and outer semicon layer, respectively.

3.5. Data Processing in PEA Method

In space charge measurements using the PEA method, the raw signal is a convolution of the actual charge distribution and the system's transfer function. To extract the true signal from the specimen, signal post-processing is essential. Therefore, deconvolution is applied after measurement. In this study, dual-domain deconvolution approach is employed to improve accuracy and reliability.

3.5.1. Reference Signal Acquisition

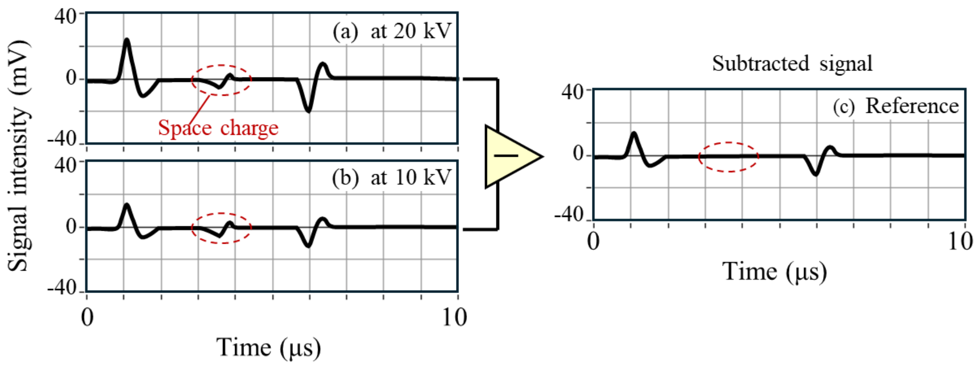

Fig. 3.4 Subtraction method to obtain reference signal.

In the deconvolution process used to reconstruct the space charge distribution, two types of signals are essential: the reference signal (also known as the impulse response) and the target signal, which contains the actual space charge information. Within the framework of the PEA (Pulsed Electroacoustic) method, the reference signal plays a critical role, as it characterizes the system's response in the absence of space charge. Conventionally, this reference is obtained by applying a pulse voltage superimposed on a low-level DC voltage to a sample that is assumed to be free of space charge. Under such conditions, the recorded signal is considered to reflect only the dielectric properties of the materials such as permittivity distribution without contributions from space charge. From this calibration signal, the reference signal is typically extracted using a window function, isolating the portion of the waveform that corresponds to the system's impulse response.

However, in this study, a different approach was employed to derive the reference signal. Instead of acquiring it through a low-voltage application on a charge-free sample, the reference signal was extracted by subtracting the waveform obtained by low DC voltage application from the waveform with high voltage application as shown in Fig. 3.4. This subtraction method isolates the system's dynamic response related solely to the applied voltage, effectively removing the space charge that has accumulated in the insulation [5,10]. The resulting signal is then used as the reference in the deconvolution process. This approach is particularly useful when it is difficult to obtain a truly charge-free reference such as in full-size cables or specimens with prior voltage application histories where residual or pre-accumulated space charge might already exist.

3.5.2. Deconvolution

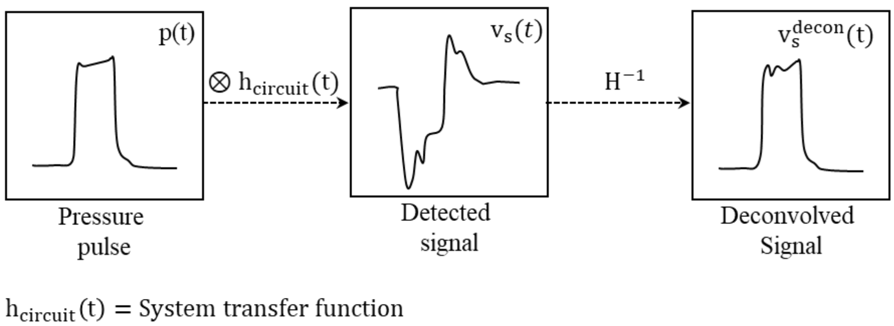

Fig. 3.5 Diagram of deconvolution process.

This chapter presents the development and implementation of a dual-domain deconvolution method to extract the true space charge distribution from raw PEA signals, which are inherently convolved with the system's transfer function. Traditional frequency-domain deconvolution, while widely used, often suffers from instability, particularly in the low-frequency spectrum, resulting in baseline shifts and artificial DC components.

To address these challenges, a combined time-frequency domain deconvolution approach was proposed [6,7] which will be used in the deconvolution process in this study. The method begins by generating target and reference signals through the subtraction procedure to obtain reference signal. These signals are then windowed with a Tukey function isolating the main acoustic peak.

In the time domain, a matrix template of the system response is constructed, and the original space charge profile is estimated via least squares minimization, providing a stable, noise-suppressed result. In parallel, frequency-domain deconvolution is performed to retain high-frequency content, albeit with inherent risks of instability.

By using dual-domain method it combines the strengths of both domains by applying a threshold frequency to merge the low-frequency content from time-domain processing with the high-frequency details obtained from frequency-domain division. This integration yields a final charge distribution that is both physically accurate and free of unwanted low-frequency artifacts.

The resulting deconvoluted signals serve as the foundation for calculating space charge distributions, electric field profiles, and potential within the insulation system. This methodology significantly enhances the reliability and resolution of space charge measurements in high-voltage insulation diagnostics.

The signal processing underpinning the dual-deconvolution technique in space charge measurement will be discussed in this article. The deconvolution output is then used to determine charge and field intensity distributions, as well as potential.

3.5.2.1. Target and Reference Signal

The signal processing stream begins with the target signal, which is acquired at various levels of applied DC voltage. The reference signal is then generated by subtracting the lower-voltage signal (assumed to represent the initial space charge-free condition) from each target signal. This subtraction isolates the additional response induced by higher voltage stress. To minimize spectral leakage and focus on the most relevant signal component, the resulting waveform is convolved with a Tukey window in the time domain. During this step, only the first peak of the waveform corresponding to the initial acoustic response is retained, while the remaining samples are set to zero. This is justified by the low noise content in the original waveform.

3.5.2.2. Time-Domain Deconvolution

Since the full frequency-domain deconvolution always leads to an unpredictable result located on its low-frequency parts, the deconvolution in time-domain is then performed. The convolution between the space charge that originally exists in the cable and the system response of the signal is expressed by equation (3.27).

$$s_{tgt} = Hs_{input} \tag{3.27}$$

Where s_{tgt} is the convolution between the original space charge and the system function. S_{input} is the original space charge and H is a template matrix constructed by time-shifting the reference signal. The shape of the template is expressed by equation (3.28).

$$H \equiv \begin{bmatrix} h_0(t_0) & \cdots & h_0(t_i) & \cdots & h_0(t_m) \\ \vdots & \ddots & \vdots & & \vdots \\ h_j(t_0) & \cdots & h_j(t_i) & \cdots & h_n(t_m) \\ \vdots & & \vdots & \ddots & \vdots \\ h_n(t_0) & \cdots & h_n(t_i) & \cdots & h_n(t_m) \end{bmatrix} \tag{3.28}$$

The combination of the template is then obtained by weighting each component inside the matrix with q_j. The result is expressed by equation (3.30).

$$s_{tgt}' = (t_i) \equiv \sum_{j=0}^{n} h_j\left(t_i\right) q_j \tag{3.29}$$

The impulses with similar distribution with the original signal are obtained by minimizing the Least Square error between the target signal and the template, as expressed by equation (3.30).

$$\sum_{i=0}^{m}\left\{s_{tgt}(t_i)-s_{tgt}'(t_i)\right\}^2=\sum_{i=0}^{m}\left\{s_{tgt}(t_i)-\sum_{j=0}^{n}h_j(t_i)q_j\right\}^2 \tag{3.30}$$

The final output is the time domain signal consisted of the distribution of impulses q_j that represents the original signal, expressed by equation (3.31). The detail of the signal processing had been discussed in the previous research which is applied to extract the reflection coefficient from human cheek skin [8].

$$\begin{pmatrix} q_0 \\ \vdots \\ q_j \\ \vdots \\ q_n \end{pmatrix} = \left(H^T H\right)^{-1} H^T \begin{pmatrix} s_{tgt}(t_0) \\ \vdots \\ s_{tgt}(t_i) \\ \vdots \\ s_{tgt}(t_m) \end{pmatrix} \tag{3.31}$$

3.5.2.3. The Time Frequency Domain Deconvolution

The calculation is started by convolving both target and reference signal with an appropriate Tukey-typed window function in order to avoid the spectral leakage. Both of the signal is then subjected into the Fourier transform and the target signal is divided by the reference signal. The result will be a noisy waveform because the division process sometimes encounters a “division by zero” which occur when the frequency components of the reference signal is really small [4,5]. A low-pass filter is then applied to reduce the number of high-frequency components in the signal. However, oftentimes, the output signal will be disturbed by an unnecessary low-frequency component in the form of a baseline or an offset because of the improper division in the Fourier domain which leads to the instability of the generated low-frequency components in the output signal.

3.5.3. Charge and Electric Field

After performing the deconvolution process, the acquired signal $q(r)$ represents the space charge intensity profile. However, since the specimen has a coaxial structure, the profile must be compensated to account for the divergence of acoustic wave propagation, as described in Equation (3.19).

$$q'(r) = A\{q(r) - B\}\sqrt{\frac{r}{r_0}} \tag{3.32}$$

Where r_0 is the outer radius of the insulation, and A is the scale factor. The factor B represents a small offset that inevitably arises from the measurement and deconvolution processes. The electric field at any point along the radius is expressed as:

$$\mathrm{E}(r) = A\int_{\mathrm{r}_0}^{\mathrm{r}} \frac{1}{\varepsilon r}\{q(r) - B\}r\sqrt{\frac{\mathrm{r}}{\mathrm{r}_0}}\,dr \tag{3.33}$$

The potential at any point along the radius is given by:

$$V(r) = -\int_{r_0}^{r} E\,(r)dr \tag{3.34}$$

3.5.4. Deconvolution application

Application of deconvolution in this research (Chapter 5 and Chapter 6) In this research, the previously described deconvolution method is applied to two main case studies:

1. **Chapter 5: Space Charge Measurement in Full-size Cable**
   This chapter presents space charge measurements in a full-size cable using a PEA cell. Deconvolution is applied to process the measured signals and retrieve the actual space charge distribution from the convolution with the system's transfer function.
2. **Chapter 6: Space Charge Measurement in Cable Joint**
   Cable joints have more complex structures due to the presence of material interfaces and triple junctions. In this chapter, deconvolution will be conducted in the type the first deconvolution to calibrate the target signal from the system transfer function and the second type of deconvolution is applied to compensate several factors such as acoustic divergence due to geometry, pulse stress distribution caused by dielectric differences, acoustic attenuation, and variations in the speed of sound.

By applying a deconvolution method in both chapters, it is expected that the obtained space charge distribution can describe the internal electrical conditions of the insulation system with sufficient accuracy for engineering analysis and diagnostics.

3.6. Summary

The Pulse Electro-Acoustic (PEA) method is a diagnostic technique used to measure space charge distributions in dielectric materials, especially in high-voltage DC cable systems. This chapter outlines the working principle of the method, where a superimposed pulse voltage generates acoustic waves through electro-mechanical interactions with space charges and induced charges in the insulation. These waves are detected by a piezoelectric sensor and analyzed to reconstruct the charge profile. The system involves components such as coupling electrodes, piezoelectric film sensors, and backing materials. The chapter also explains signal generation based on Lorentz force, acoustic wave propagation, and the impact of cylindrical geometry on wave attenuation and signal accuracy. Corrections for electric field divergence and acoustic wave decay are necessary for accurate space charge profiling in full-scale cable systems.

Reference

[1] R. Bodega, P. H. F. Morshuis and J. J. Smit, “Space charge measurements on multi-dielectrics by means of the pulsed electroacoustic method,” in IEEE Transactions on Dielectrics and Electrical Insulation, vol. 13, no. 2, pp. 272-281, 2006.

[2] R. Bodega, Space charge accumulation in polymeric high voltage DC cable systems, Ph.D. dissertation, Delft University of Technology, Delft, The Netherlands, 2006.

[3] W. Sachse and Y. Pao, “On the determination of phase and group velocities of dispersive waves in solids,” J. Appl. Phys., vol. 49, pp. 4320–4327, 1978.

[4] Y. Li, K. Murata, Y. Tanaka, T. Takada, and M. Aihara, “Space charge distribution measurement in lossy dielectric materials by pulsed electroacoustic method,” Proc. 1994 4th Int. Conf. Prop. Appl. Dielectr. Mater., vol. 2, pp. 725–728, 1994.

[5] S. Zahra, T. Kawashima, Y. Murakami, and N. Hozumi, “Small-size space charge measurement device for power cables by using electrically insulated acoustic coupler,” 2020 IEEE 3rd Int. Conf. Dielectrics (ICD), Valencia, Spain, pp. 359–362, 2020.

[6] N. Hozumi, E. B. Prastika, S. Zahra, T. Kawashima, and Y. Murakami, “Dual-domain deconvolution process applied to time-resolved quantitative dielectric measurement,” 2020 IEEE 3rd Int. Conf. Dielectrics (ICD), Valencia, Spain, pp. 347–350, 2020.

[7] E. B. Prastika, S. Zahra, X. Li, T. Kawashima, Y. Murakami, and N. Hozumi, “The application of signal processing using dual domain deconvolution for new space charge measurement method in HVDC full-size cables,” 2020 Int. Symp. Electrical Insulating Materials (ISEIM), Tokyo, Japan, pp. 277–280, 2020.

[8] E. B. Prastika, A. Imori, T. Kawashima, Y. Murakami, N. Hozumi, S. Yoshida, R. Nagaoka, and K. Kobayashi., “Acoustic impedance interpretation of cross-sectional human skin by using time and frequency domain deconvolution,” Jpn. J. Appl. Phys., vol. 59, no. SK, p. SKKB06, 2020.

[9] M. Fu, Space charge measurement in polymer insulated power cables using the PEA method, Ph.D. dissertation, University of Southampton, Southampton, U.K., 2022.

[10] X. Li, S. Zahra, T. Kawashima, Y. Murakami, and N. Hozumi, “Lock-in calibration for space charge measurement,” 2020 IEEE 3rd Int. Conf. Dielectrics (ICD), Valencia, Spain, pp. 391–394, 2020.

Chapter 4 Pulse Voltage Application in Space Charge Measurement

4.1. Introduction

To evaluate space charge behavior, non-destructive measurement techniques such as acoustic and thermal methods are commonly used. However, the pulsed electroacoustic (PEA) method is particularly widespread, as it enables direct space charge profiling by applying a pulse voltage in combination with a high DC voltage. The pulse electric field interacts to electric stress accompanied by space charge to produce acoustic pulse wave. The signal is captured by a piezoelectric device that is mounted outside the insulation [1].

In order to apply the pulse voltage together with a high DC voltage, a coupling capacitor is required. However, when a full-size cable is used as a specimen, a certain length is needed to attach terminals for high DC voltage application, increasing the capacitance of the specimen. As a result, the cable can no longer be considered a lumped capacitor, and multiple reflections may take place if the pulse voltage is applied at the terminal. In addition, the scale of the coupling capacitor may be so significant that a large inductance may be produced between the specimen and pulse voltage source, leading to the loss of frequency characteristics of the measurement system.

As full-size cables are normally tested under voltages as high as 500 - 1000 kV, depending on the rated voltage, the above problems are very significant in performing the space charge measurement. The authors proposed a suitable method for measuring the internal charge while applying a voltage to full-scale power cables [2, 3]. Our proposal does not need such a capacitor, because the cable specimen itself plays a roll of the pulse coupler. This series of studies is to find the condition required for the measurement.

However, when a finite-length cable is used as a coupler, its impedance exhibits strong frequency dependence. In this case, the cable behaves as a transmission line, and the propagation of the pulse voltage must be analyzed accordingly. When a voltage pulse is sent through the cable, it travels toward the open end. Since an open end presents an infinite impedance, the mismatch causes the signal to reflect back toward the source. These reflections do not simply disappear; instead, they travel back along the line and may interfere with the original signal.

The nature of these reflections is determined by the electrical length of the cable relative to the wavelength of the signal components. If the cable length corresponds to a specific fraction of the signal's wavelength, constructive or destructive interference may occur, a phenomenon known as resonance. Resonance can result in standing wave formation, amplification of certain frequency components, and waveform distortion such as ringing. If the length is not resonant, reflections still occur but typically cause less distortion.

Therefore, in this chapter, the influence of the cable length on waveform behavior and signal fidelity will be analyzed based on transmission line theory and pulse propagation characteristics, with a particular focus on how these effects impact the accuracy of space charge measurements in full-scale cable systems.

4.2. Voltage application in PEA method

4.2.1. Measurement System

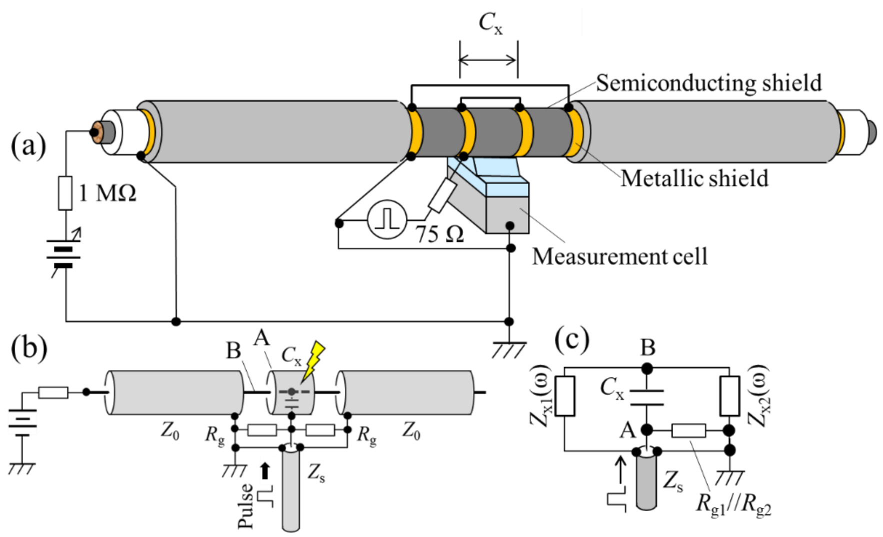

Fig. 4.1 Outline of the measurement system including the cable specimen (a) and its equivalent circuit (b), (c). R_g represents the resistance across the gap between electrodes.

Fig. 4.1 shows a schematic diagram of the space charge measurement system for full-size cable. It basically employs the principle of the pulsed electroacoustic (PEA) method. A part of the cable specimen is removed with metallic shield, and a piezoelectric device is mounted. A high voltage pulse is applied across the piezoelectric device and the shield layer. The acoustic coupler, made of polystyrene, makes it possible to apply a high voltage pulse on the shield layer whereas the piezoelectric device is kept at the ground potential. The acoustic coupler also has the ability to improve acoustic impedance matching and sensitivity due to its close acoustic impedance to the polyethylene specimen and the piezoelectric element (PVDF: polyvinylidene fluoride) which will be discussed in Chapter 5.

A DC high voltage is applied at the terminal. For acoustic coupling an oil layer is interposed between the specimen and acoustic coupler, on which the piezoelectric sensor is embedded. As the pulse voltage is applied from the ground side of the specimen, no coupling capacitor is needed. In fact, as described above, cable specimen itself plays a roll of coupling impedance.

The measurement system can be represented by an equivalent circuit as shown in Fig. 4.1 (c), in terms of the pulse response. Z_{x1} and Z_{x2} represent the impedance looked from the measuring point, depending on the frequency component. The cable specimen may make resonance, if the pulse voltage has a certain frequency component. In such a case, the impedance synthesized by Z_{x1} and Z_{x2} may be very high, so that the reduction in the voltage across C_x takes place. In addition, as the resonance corresponds to multiple reflections across the cable specimen, the shape of the applied single pulse may be disturbed because of ringing.

4.2.2. Resolution of the Measurement

Resolution of the space charge depends on the width of the pulse voltage. To simplify the analysis, the space charge distribution is assumed to follow a Gaussian function. It can be transformed into the time domain using the sound speed of cross-linked polyethylene (2000 m/s), which serves as the insulation. In this paper, two cases with half-widths of 100 ns and 400 ns are considered, corresponding to spatial widths of 200 μm and 800 μm, respectively.

4.3. Response of Pulse Width Depends on Cable Length

In order to retain a certain spatial resolution, a pulse voltage with an appropriate frequency component should be applied at the measuring point. Assuming the voltage source generates a pulse voltage with a flat frequency spectrum, the frequency spectrum at the measuring point was estimated. The equivalent circuit of the system including the specimen and feeder cable is shown in Fig. 4.1 (c). The cable specimen is considered as a distributed circuit of finite length with open ends. l_1 and l_2 are the lengths to the end terminal from the measured section. As only a short length of the cable specimen is subjected to the measurement, the measured section can be represented as a lumped capacitance C_x. The cables with l_1 and l_2 in length can be recognized as frequency dependent impedances (open stubs) Z_{x1} and Z_{x2}, respectively, when they are looked from the measuring point. The system is thus simplified as to be a circuit composed of one small capacitance and two frequency dependent impedances.

The impedance of the cable fragment with an open end and ℓ_1 in length is described as

$$Z_{x1} = Z_0 \frac{e^{j\gamma l_1} + \Gamma_1 e^{-j\gamma l_1}}{e^{j\gamma l_1} - \Gamma_1 e^{-j\gamma l_1}}, Z_{x2} = Z_0 \frac{e^{j\gamma l_2} + \Gamma_2 e^{-j\gamma l_2}}{e^{j\gamma l_2} - \Gamma_2 e^{-j\gamma l_2}}, Z_x = Z_{x1}//Z_{x2} \tag{4.1}$$

$$\gamma = \alpha + j\beta \tag{4.2}$$

where f is frequency, c is propagation speed along the cable specimen, γ is propagation constant dependent on frequency, and Z_0 is the characteristic impedance of the cable specimen. Γ_1 and Γ_2 are the reflection coefficients at the distance l_1 and l_2 from the measuring point, respectively [4,5]. Γ_1 and Γ_2 are assumed as to be 1 in this particular case. To make the calculation simple, α and β are assumed to be in proportion to frequency as

$$\alpha = 2\pi f \alpha_0, \beta = 2\pi f / c \tag{4.3}$$

When a pulse voltage is applied through a coaxial cable with a characteristic impedance Z_s, the reflection coefficient Γ at the application point (feeding point) is

$$\Gamma = \frac{(Z_x + Z_c) - Z_s}{(Z_x + Z_c) + Z_s} \tag{4.4}$$

where Z_x is the combined impedance of Z_{x1}, Z_{x2}. The applied voltage V_c across C_x is subsequently calculated by

$$\frac{V_c}{V_s} = (1 + \Gamma)\frac{-jX_c}{Z_x - jX_c} \tag{4.5}$$

$$X_c = \frac{1}{j2\pi f C_x} \tag{4.6}$$

where V_s is the voltage propagating through the feeder cable.

The length of the measured section was set to 1 m and was approximated by a 100 pF capacitor. The attenuation at both ends of the cable was assumed to be approximately 10 dB per kilometer at 1 MHz. The characteristic impedance of the sample cable was set to 50 Ω to match the coaxial communication cable used in the experiment. The surge impedance of power cables is approximately 20 Ω. If the length of the measured section and the cables on both sides are the same, the waveform shape is expected to remain approximately unchanged.

Table 4.1 Cable specimen and feeder cable specifications.

Cabel Specimen	
Capacitance at the measuring point (C_x)	100 pF
Length of the cable specimen (l_1 and l_2)	2 m, 10 m
Spatial resolution	200 μm, 800 μm
Characteristic impedance of the cable specimen (Z_0)	50 Ω
Attenuation coefficient of the cable specimen (α_0)	10 dB/MHz/km
Propagation speed of the cable specimen (c)	200 m/μs
Feeder Cable	
Characteristic impedance of the feeder cable (Z_s)	50 Ω

4.4. Comparison Between Simulated and Measured Results

Fig. 4.2,Fig. 4.3,Fig. 4.4,Fig. 4.5, show the results of simulation and measurement. Diagram (a) in each figure shows frequency characteristics of the applied voltage across C_x, and diagram (b) shows reproduced pulse waveforms in time domain. The results of experiments carried out to verify the calculation results are shown in diagrams (c) and (d). The circuit shown in Fig. 4.1(b) was constructed using RG-174/u coaxial communication cable. The characteristic impedance was 50 Ω, and the length of the section corresponding to the measured section was 1 m. The length of the cable sections at both ends was either 2 m or 10 m (with both sections having the same length in each case). The pulse applied to the semiconducting outer shield electrode was of negative polarity, so that a positive pulse voltage was applied to the conductor. A pulse voltage of approximately 200V was applied and the voltages between A-G and between B-G were measured with high impedance voltage probes across the DC to 200 MHz band, the results of which are shown in diagram (c). The differential waveform (d) shows the voltage applied between the conductor and the outer shield electrode at the measured section.

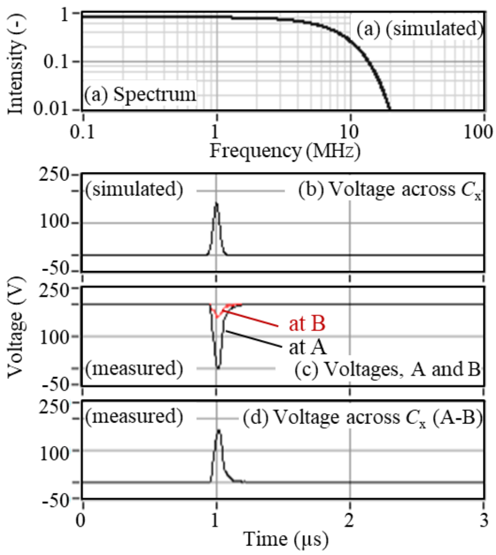

Fig. 4.2 Comparison between simulated and measured results of $l_1 = l_2$: 2 m, C_x: 100 pF, resolution: ~200 μm. (a)(b): spectrum and time-domain profiles of the voltage across C_x as simulated. (c)(d): Measured at points A and B (refer to Fig. 4.1) and their differential.

Fig. 4.2 and Fig. 4.3 show the results when the pulse width was about 100 ns. The spatial resolution is about 200 μm when multiplied by the sound speed of polyethylene, which is about 2 mm/μs. If the cable insulation is about 3 mm thick, this corresponds to a relative spatial resolution of 7 %.

Fig. 4.2 shows the case of 2 m coupling cables. The resonance frequency of the open stub formed by the coupling cable was high, and the pulse waveform applied to the measured section was not significantly different from that of the fed pulse because of repeated multiple reflections and rapid attenuation. The coupling cable acts almost as a capacitance. The voltage dividing ratio is 4/5, slightly lower than that of the input pulse. The calculated and experimental results are in good agreement.

Fig. 4.3 illustrates the case where the coupling cables were 10 m long. In the low-frequency range, the impedance of the open stub is reduced, resulting in a slightly higher signal intensity compared to Fig. 4.2. However, the effect of multiple reflections (ringing) becomes more pronounced, with a resonance point around 10 MHz. If the insulation thickness of the cable is less than approximately 3 mm, it superimposes with the signal from the conductor side, making the deconvolution process using signals from the external shielding electrode more difficult.

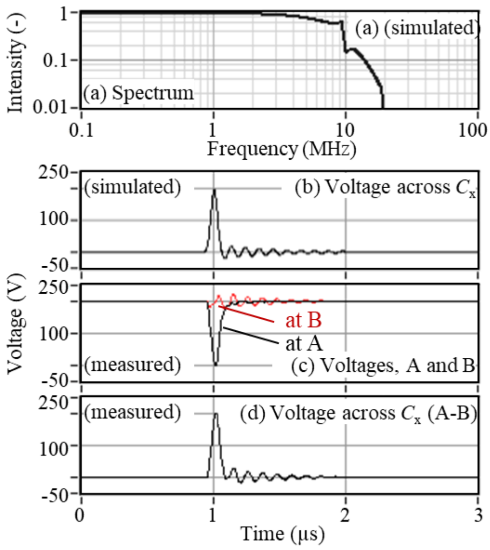

Fig. 4.3 Comparison between simulated and measured results of $l_1 = l_2$: 10 m, C_x: 100 pF, resolution: ~200 μm. (a)(b): spectrum and time-domain profiles of the voltage across C_x as simulated. (c)(d): Measured at points A and B (refer to Fig. 4.1) and their differential.

Fig. 4.4 and Fig. 4.5 show the results when the pulse width was approximately 400 ns, corresponding to a spatial resolution of 800 μm. Pulse widths of this magnitude are considered appropriate for cable insulation thicknesses of 10 mm or more. Fig. 4.4 shows the result when the coupling cable was 2 m long. As in Fig. 4.2, the resonant frequency of the open stub formed by the coupling cable is high and the shape of the waveform applied to the measured section is not significantly different from that of the applied pulse voltage due to repeated multiple reflections and rapid attenuation. The coupling cable acts almost as a capacitor, and the voltage divider ratio is about 4/5 as in Fig. 4.2, which is slightly lower than the voltage at the feeding point.

Fig. 4.5 shows the case where the coupling cable was 10 m long. The multiple reflections decayed within a time period of about the pulse width. In both cases shown in Fig. 4.4 and Fig. 4.5, when the cable insulation thickness is sufficiently greater than about 3 mm, the signals from the outer shield electrode and the inner electrode are completely separated, and the deconvolution process can be performed using the signal from the outer shield electrode. Although there is a difference in the time domain waveforms because the calculations use Gaussian waveforms as input while the experiments use pulse waveforms close to square waves, the frequency band used is narrower when the spatial resolution is low, which allows the effect of ringing to be eliminated.

Although it is considered that extremely long cable lengths is required to completely eliminate the effects of multiple reflections at both ends of the cable, in practical cases where the measured section is as short as 1 m and the attenuation coefficient is as high as 10 dB/MHz/km, a coupling cable of a few meters can provide a resolution of several hundred μm without significant ringing. In such cases, no significant resonance takes place because damping at high frequencies reduces the degree of resonance. In addition, the frequency component of the applied pulse voltage is limited so that high frequency components are not detected.

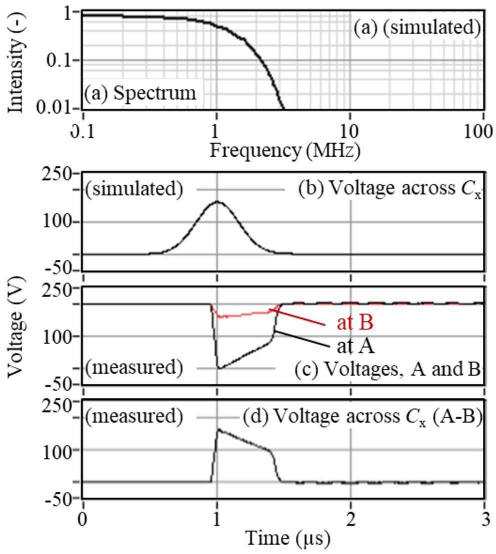

Fig. 4.4 Comparison between simulated and measured results of $l_1 = l_2$: 2 m, C_x: 100 pF, resolution: ~800 μm. (a)(b): spectrum and time-domain profiles of the voltage across C_x as simulated. (c)(d): Measured at points A and B (refer to Fig. 4.1) and their differential.

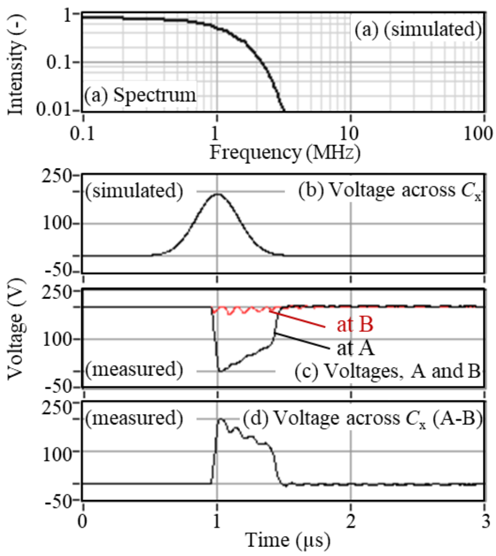

Fig. 4.5 Comparison between simulated and measured results of $l_1 = l_2$: 10 m, C_x: 100 pF, resolution: ~800 μm. (a)(b): spectrum and time-domain profiles of the voltage across C_x as simulated. (c)(d): Measured at points A and B (refer to Fig. 4.1) and their differential.

4.5. Summary

The pulsed electroacoustic method which requires a coupling capacitor to apply a sharp pulse voltage across the insulation as well as applying a high DC voltage. In order to avoid the use of the capacitor that would be very large in scale in the case of full-size cable measurement, we proposed to use the cable specimen itself as a pulse coupler. However, as the cable is finite in its length, it may work as a resonator and disturb the pulse voltage across the insulation, depending on the frequency component of the pulse voltage. A calculation in frequency domain shows that the resonance is significant when the cable is as long as 10 m. Longer cable may cause resonance at low frequency but it would be less significant because of attenuation thorough the cable specimen. A good pulse waveform across the insulation was seen when the cable length was as short as 2 m, however it is considered that too short cable specimen would lead to the reduction in the sensitivity.

Reference

[1] Y. Li, M. Yasusa, and T. Takada, "Pulsed electroacoustic method for measurement of charge accumulation in solid dielectrics," IEEE Transactions on Dielectrics and Electrical Insulation, vol. 1, pp. 118–195, 1994.

[2] N. Hozumi, H. Suzuki, T. Okamoto, K. Watanabe, and A. Watanabe, "Direct observation of time-dependent space charge profiles in XLPE cable under high electric fields," IEEE Transactions on Dielectrics and Electrical Insulation, vol. 1, no. 6, pp. 1068–1076, 1994.

[3] N. Hozumi, T. Takeda, H. Suzuki, and T. Okamoto, "Space charge behavior in XLPE cable insulation under 0.2-1.2 MV/cm dc fields," IEEE Transactions on Dielectrics and Electrical Insulation, vol. 5, no. 1, pp. 82–90, 1998.

[4] N. Hozumi and M. Hori, "Space charge measurement for full-scale HVDC cables using pulsed-electroacoustic method," Cigre Science & Engineering, no. 6, pp. 97-102, 2016.

[5] F. T. Ulaby: "Fundamentals of Applied Electromagnetics", Prentice Hall, New Jersy, ISBN 0130329.

Chapter 5 Development of A High-Sensitivity PEA System for Space Charge Measurement in Full-size HVDC Cables

5.1. Introduction

During the development of insulation materials, researchers often use sheet-type specimens or miniature cable models to assess insulating performance through space charge measurements. However, it's highly beneficial and even necessary to directly measure space charge in full-size cables. This ensures that the insulation performance observed in small-scale samples truly reflects the behavior in actual manufactured products. For this reason, the authors strongly support the importance of space charge measurements on full-size cables.

The Pulsed Electro-Acoustic (PEA) method is one of the most effective techniques for space charge analysis. It involves applying a narrow pulse voltage superimposed on a high DC voltage across the insulation. When the electric pulse field interacts with space charge, it generates an acoustic pressure wave, which is then detected by a piezoelectric sensor placed outside the insulation [1,2].

However, when testing full-scale cables, the physical length needed to connect high-voltage terminals increases the sample's total capacitance (or effectively lowers its impedance), which degrades the coupling performance. For cables longer than a few meters, the cable can no longer be treated as a simple lumped capacitor. Instead, the cable behaves more like a transmission line, where signal reflections become significant during pulse application.

Furthermore, using a large coupling capacitor introduces considerable inductance between the cable and the pulse generator, which negatively affects the system's frequency response [2]. Considering that full-size HVDC cables often operate under voltages ranging from 500 to 1000 kV, these technical challenges are especially critical for achieving accurate space charge measurements at such high ratings.

Previously, researchers at the Central Research Institute of Electric Power Industry in Tokyo, Japan, introduced a method for measuring internal space charge in full-size power cables under high DC voltage conditions [3, 4]. Their approach eliminated the need for a separate coupling capacitor by allowing the cable specimen itself to act as a pulse coupler.

However, one significant drawback of that setup was its limited sensitivity when used on full-size cables. The main issue stemmed from poor acoustic impedance matching between the sample and the piezoelectric transducer, which reduced the efficiency of acoustic wave transmission.

In this chapter, we present a newly designed measurement cell that significantly improves acoustic matching between components with differing acoustic properties. In the conventional design, an aluminum block served as the acoustic coupler. In our new PEA device, we replaced this with polystyrene an insulating material with lower acoustic attenuation and better impedance compatibility with cable insulation.

This improved configuration, combined with a polyvinylidene difluoride (PVDF) piezoelectric transducer and a metallic backing layer, enhances the transmission of acoustic energy. As a result, the device achieves much higher measurement sensitivity. Additionally, the use of a polymer-based acoustic coupler provides galvanic isolation between the measurement cell and the cable's insulation screen (outer electrode), where the high-voltage pulse is applied.

The effectiveness of this new PEA device has been successfully demonstrated through testing on a full-scale power cable.

5.2. New PEA Cell Design

In the conventional PEA system, metallic material, such as aluminum, is utilized as the acoustic coupling medium that connects the outer semi-conductive layer and the acoustic sensor, whereas it also serves as an electrode. This metal component serves a dual function: it acts as both an electrical electrode for high-voltage pulse injection and as an acoustic transmission medium. However, this design inherently introduces a significant acoustic mismatch, especially when measuring polymeric insulation systems such as polyethylene. The difference in acoustic impedance between the metal and polymer results in energy reflection and signal loss at the interface, reducing the measurement system's sensitivity and fidelity.

Moreover, when polymer-based piezoelectric material such as PVDF is used as the sensor, a similar mismatch occurs at the interface with the metallic coupler, further degrading signal intensity. The conventional method typically uses polymer backing material with an acoustic impedance close to that of the sensor to suppress internal reflections and broaden the sensor's frequency response. However, even with this design, much of the acoustic energy is transmitted to the backing, reducing the signal amplitude received by the sensor.

5.2.1. Comparison: New and Conventional Cell

Table 5.1 outlines the structure and materials used in both the proposed and conventional PEA cells, while Fig. 5.1 provides a visual diagram to clearly illustrate the differences in their composition. These serve as an overview to help readers grasp the fundamental distinctions between the two designs. The detailed explanation of the material choices and performance differences will be presented in the following subchapters.

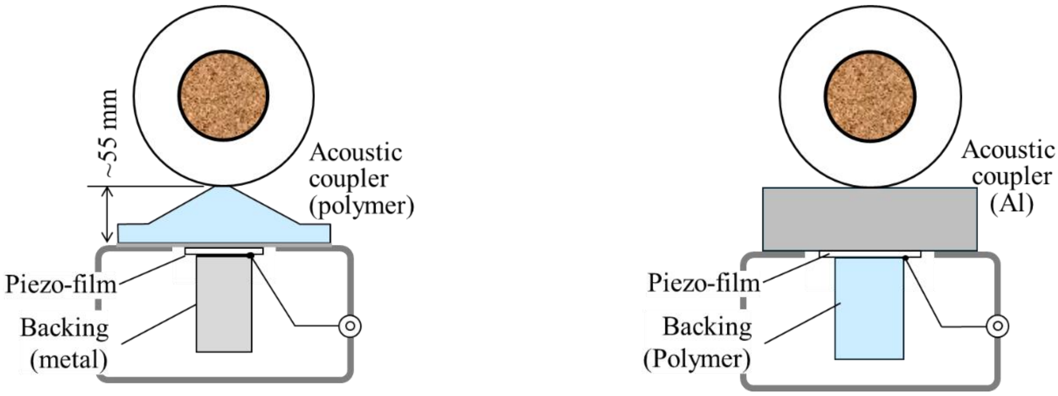

Fig. 5.1 The diagram of PEA cell by using polymeric acoustic coupler (proposed) for the space charge measurement in full size HVDC cable (left) conventional PEA cell (right).

Table 5.1 Structure and material of Proposed and conventional PEA cell.

	New	**Conventional**
Acoustic Coupler	Polymer	Aluminum
Sensor	PVDF	PVDF
Backing	Metal	Polymer

5.2.1.1. Acoustic Coupler

In the conventional method of space charge measurement, metal electrodes are used as acoustic couplers to connect the measurement system with insulating wires. The couple also plays an important role as a delay line, preventing superposition of the measurement signal with spike noise due to the pulse voltage. Although the measurement shown in this figure was obtained using the new PEA cell, the purpose is to demonstrate the necessity of an acoustic coupler functioning as a delay line before the acoustic signal reaches the transducer which will be discussed further in the next sub-chapter.

However, this approach has limitations, mainly due to the impedance mismatch between the aluminum coupling capacitor and the cable insulation. As a result, signal reflection occurs, and measurement accuracy decreases. To overcome this problem, a new method using polymer couplers has been developed and has been shown to increase sensitivity up to four times compared to metal couplers. Further details of sensitivity calculation is discussed in the next section.

In addition to enhanced sensitivity, the polymer coupler offers significant advantages in terms of electrical isolation. It provides galvanic isolation by electrically separating the measurement system from the cable's shielding layer, which allows pulse voltage to be applied while keeping the measurement system safely grounded. This setup removes the need for additional optical isolation, as was necessary in the conventional method. As a result, the measurement system becomes simpler and safer to operate under high-voltage conditions, while also delivering a clearer and more accurate signal compared to traditional metallic couplers.

This method also offers better impedance matching with the insulating material, enabling more efficient acoustic signal transmission and minimizing signal loss. As polymer, either PMMA and XLPS both were generally used as the acoustic coupler for the new PEA cell. However, in this study, XLPS was selected as the coupler material due to its acoustic properties specifically, its lower sound velocity and higher acoustic transparency compared to PMMA. While PMMA is easily available in the market and can function as an acoustic coupler, its relatively high sound velocity resulting a thicker layer to serve effectively as a delay line compare to XLPS. Which makes XLPS the more suitable choice for the measurement needs in this study, as supported by the comparison of acoustic absorption in polymers shown in Fig. 5.2. Regarding Fig. 5.2 , it is considered that the frequency band required for full-size cable measurement extends up to several MHz. Assuming an acoustic coupler thickness of about 20 mm is the least needed to avoid multiple reflections within the time window, the absorption in PMMA and PS (polystyrene) is less than 6 dB/mm. This level of absorption can be considered negligible when compared to the absorption occurring in polyethylene, which is used as the specimen.

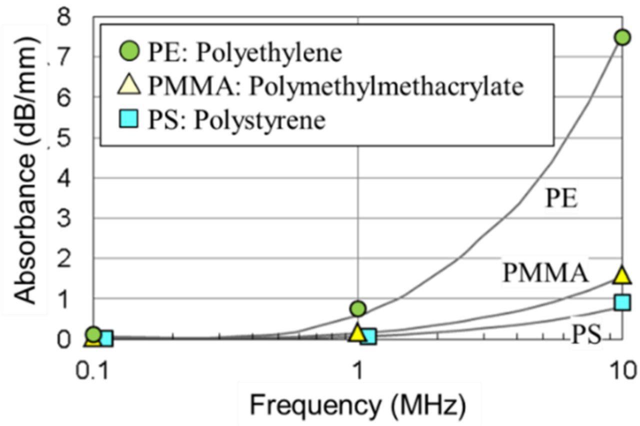

Fig. 5.2 Sound absorption coefficient of various polymer materials [1,5]. Reprinted with permission from © 2024 IEEE.

5.2.1.2. Piezoelectric sensor

The design of the acoustic sensor plays a key role for the optimum performance of the measurement cell. The transducer consists of a polarized PVDF piezo film. This Piezoelectric sensor is placed underneath the polymer acoustic coupler, as to receive the signal propagates through the coupler. 110-µm-thick PVDF film was used as the piezoelectric sensor. In addition, an aluminum film (11 µm-thick cooking foil) was used to obtain contact between the upper electrode of the PVDF sensor and the shielding box.

The thickness of the piezoelectric sensor must be small enough to achieve a desired spatial resolution while at the same time a higher thickness achieves a higher output signal magnitude, increasing the signal to noise ratio.

The induced voltage across the piezoelectric sensor is due to the integral of the existing pressure waves across its thickness. This means that to optimize the spatial resolution, the sensor thickness must be smaller than the minimum wavelength of the acoustic pressure wave across the PVDF film, whereas the wavelength is depend on the applied pulsed voltage, to achieve high spatial resolution, the sensor must be thinner than the minimum wavelength of the pressure wave in PVDF, governed by:

$$\Delta t \cdot v_{PVDF} \gg d_{PVDF} \tag{5.1}$$

Where Δt the duration of the pulse and v_{PVDF} is the acoustic velocity of piezoelectric sensor, while d_{PVDF} is the thickness of the polarized PFDV piezo film.

Additionally, increasing the sensor area also increases the RC constant, enhancing low-frequency response. It is beneficial only if the entire sensor receives the acoustic wavefront nearly simultaneously. Due to the cylindrical geometry of cables and the flat PVDF layout, acoustic waves arrive circularly, causing time delays at peripheral areas and potentially degrading spatial resolution.

5.2.1.3. Backing material

As the backing material placed behind the acoustic sensor, the conventional method usually uses a polymer, the acoustic impedance between the piezo film and the backing materials needs to be as close as possible to avoid reflections at the interface which will have an impact in the output signal. This is to reduce multiple reflections inside the sensor and to expand the frequency band of the received signal. Therefore, the signal that reaches the acoustic sensor is mostly transmitted to the backing material.

However, in the proposed method, since the acoustic matching between the acoustic coupler and the PVDF sensor is also good, a good energy transfer can be retained throughout the path from the measurement target to the sensor. In addition, if a metal having a high acoustic impedance is used as the backing material, positive reflection occurs on the back of the sensor, so that the sound pressure in the sensor can be approximately twice as high as the incident sound pressure, which will be discussed in the next subchapter. Furthermore, the acoustic coupler is a polymer of which acoustic impedance is close to the sensor, multiple reflections would be effectively reduced. As a result, signals can be received with high sensitivity in a relatively good damping condition.

5.2.2. Signal Path and Acoustic Impedance

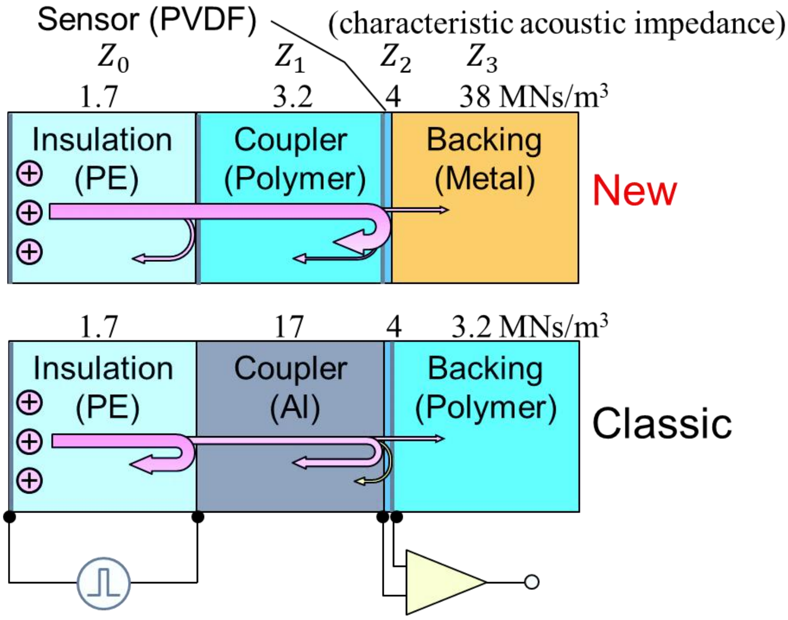

Fig. 5.3 Signal propagation in the new and the classic PEA cell.

Table 5.2 Material Characteristic of PEA cell [13]. Reprinted with permission from © 2022 IEEE.

	Material	**Sound Speed (m/s)**	**Acoustic Impedance (MNs/m^3)**
Cable	Polyethylene	2300	1.7
The New PEA Cell	Polymer	2320	2.42
	PVDF	2300	4
	Metal	2200	24.6
The Classic PEA Cell	Aluminum	6420	17
	PVDF	2300	4
	PMMA	2757	3.2

In this study, we present a novel space charge measuring technique for full-size cable samples. The pulsed electroacoustic technique is the measurement's fundamental concept, but we think it can also be used to the pressure wave method.

In the new PEA cell suggested method like which has been discussed in the previous sub chapter, the aluminum coupler is replaced with an insulating substance, such as an acrylic resin (PMMA or polystyrene). Its purpose is to provide electrical isolation between the specimen and the acoustic sensor so that a high voltage pulse may be applied across the specimen with the main body of the cable, and it acts as an acoustic coupler.

In the pulse electroacoustic method, an acoustic signal is generated in the insulation and received by a sensor fixed outside the insulation system. Fig. 5.3 shows the concept of acoustic energy transfer in a conventional method and the proposed new method. An acoustic coupler is required to be inserted between the insulation system and the measurement system. This acoustic coupler also functions as a delay line to avoid spike noise caused by high voltage pulses. In addition, since it is required with a function as an electrode to make contact with the insulating system, a metal conductor such as aluminum has conventionally been used. In such a case, if the measured object is a polymer such as polyethylene, the acoustic matching with the metal coupling medium would be downgraded due to a reflection and reduction in energy transfer rate. In addition, when a polymer piezoelectric material such as polyvinylidene fluoride (PVDF) is used as an acoustic sensor, reflection occurs at the end of metallic coupling media. As the backing material placed behind the acoustic sensor, the classic method usually uses a polymer whose acoustic impedance is close to that of the acoustic sensor. This is to reduce multiple reflections inside the sensor and to expand the frequency band of the received signal. Therefore, the signal that reaches the acoustic sensor is mostly transmitted to the backing material.

In the proposed method, a polymer such as polystyrene is used as the acoustic coupler. This improves the acoustic matching between the measurement object and the acoustic coupler itself. Since the acoustic matching between the acoustic coupler and the PVDF sensor is also good, a good energy transfer can be retained throughout the path from the measurement target to the sensor. In addition, if a metal such as lead having a high acoustic impedance is used as the backing material, positive reflection occurs on the back of the sensor, so that the sound pressure in the sensor can be approximately twice as high as the incident sound pressure. Lead is the material that is used for the proposed PEA cell due to it is sound speed, and acoustic matching has brought advantages to the improvement of the PEA cell. Brass was used before we decided to used lead, brass has higher sound speed and acoustic impedance compared with lead material. The higher sound speed made material must be thicker in order to avoid the reflection that occurred from the end of the brass. in the limited space of the PEA cell case, lead becoming more advantageous due to its lower sound speed characteristic. Therefore, thinner lead (compared with brass) can be used as the backing material and still can avoid the reflection. Since the acoustic coupler is a polymer of which acoustic impedance is close to the sensor, multiple reflections would be effectively reduced. As a result, signals can be received with high sensitivity in a relatively good damping condition.

Thus, the proposed method is expected to provide higher sensitivity than the conventional method. On the other hand, it is concerned that the acoustic attenuation of polymer coupler is larger than metal. Fig. 5.2 compares the sound absorption of various polymers. It is considered that the frequency band required for the measurement of a full-size cable is up to several MHz . Assuming the required thickness of the acoustic coupler to avoid multiple reflections appearing within the time window is about 20 mm, PMMA and PS (polystyrene) absorb less than 60 dB. Hence the absorption can be ignored if it is compared with the absorption in the polyethylene as the specimen. Thus, Polystyrene (PS) material with a small absorption is preferred as the Acoustic coupler.

If multiple reflections and acoustic absorptions are ignored, the acoustic signal having propagated through each interface as shown in Fig. 5.3 reaches the sensor and is finally reflected at the interface with the backing material. As the sensor is thin enough, the sound pressure at the sensor is represented as:

$$\frac{2Z_1}{Z_1+Z_0}\cdot\frac{2Z_2}{Z_2+Z_1}\cdot\left(1+\frac{Z_3-Z_2}{Z_3+Z_2}\right) \tag{5.2}$$

Note that PMMA is assumed as the backing material in the conventional method whereas it is used as the acoustic coupler in the proposed method. By substituting each value in the above equation and comparing the sound pressure generated inside the sensor,

$$\frac{p_{new}}{p_{conventional}} \approx \frac{2.6}{0.62} \approx 4.3 \tag{5.3}$$

By calculating the acoustic propagation through the materials, the sensitivity can be expected to increase by a factor of 4. This type of acoustic coupler is advantageous as well to apply a probing pulse voltage on the cable will be described in Pulse Voltage Application in Space Charge Measurement in Chapter 4.

5.3. Measurement Setup

5.3.1. Test Specimen

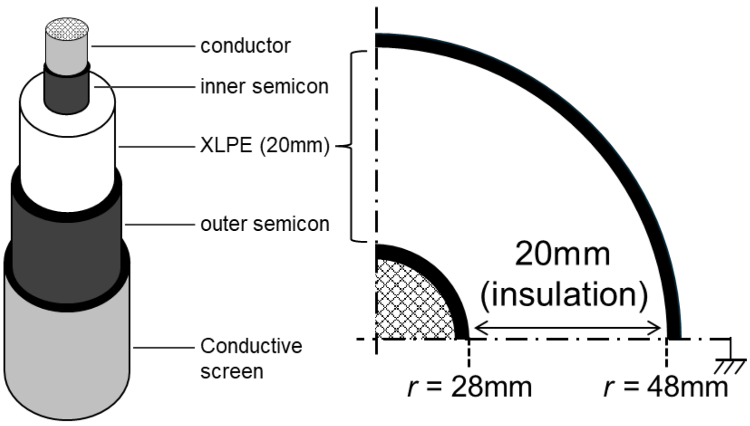

Fig. 5.4 Measured cable with 20mm thick XLPE insulation.

The cable specimen is composed of XLPE dielectric insulation, with an inner screen radius of approximately 28 mm and an outer screen radius of about 48 mm, resulting in an insulation thickness of 20 mm. This specimen is used for space charge measurement using the PEA method and is also employed to evaluate the influence of spike noise on the system, as will be discussed in the following section. The center of the cable specimen serves as the measurement region. In this area, the metallic shield layer is removed to expose the outer semi-conductive layer, enabling proper attachment of the measuring device.

5.3.2. Pulse Generator

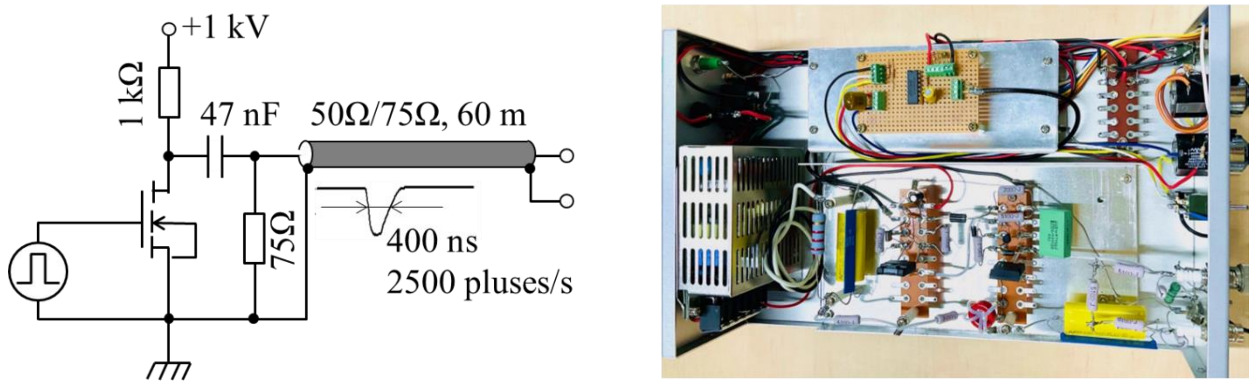

Fig. 5.5 Schematic of the pulse generator and its appearance.

Fig. 5.5 shows the schematic of the prototype pulse generator. To apply a pulse voltage to the cable insulation, a 47-nF capacitor is charged with 1 kV dc voltage. By applying an appropriate driving pulse to the gate of a field-effect transistor (Cree, C2M0080170P), drain source is short-circuited to produce −1 kV as an output. A matching resistor (50Ω/75Ω) is used to avoid multiple reflections across the feeder cable.

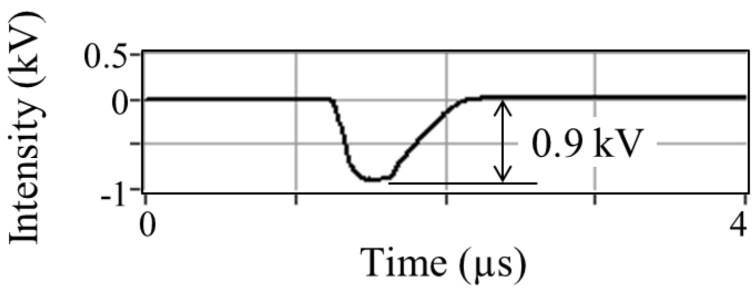

Fig. 5.6 Pulse voltage measured at the cable outer screen [13]. Reprinted with permission from © 2022 IEEE.

Fig. 5.6 shows the pulse voltage with a 75 Ω. feeder line applied to the outer screen of the cable object, with a load impedance of 90Ω. Details of the voltage application will be described in the nest section. It is seen that the pulse voltage was appropriately applied and a pulse voltage of −0.9 kV was measured at the cable outer screen.

5.3.3. Voltage Application to the Cable

Because of the semiconductive nature of the outer screen electrode, a probing pulse can be applied to the measurement section making use of the cable itself as coupling impedance, while the shield layer is kept at ground potential in terms of dc potential [4].

Fig. 5.7 shows the guard electrodes which are wound around the outer semiconducting shield on both sides of the measurement section. The guard electrodes are connected through a short wire to maintain the same potential between them. The probing pulse is applied across the gap between the guard electrode and metallic shield wrapped on the rest of the cable.

Previously, the high voltage probing pulse was applied to the measurement section via a metallic acoustic coupler. Therefore, the space charge signal had to be transmitted over an optical fiber link to ensure isolation from the ground potential [6]. In the method proposed here, since the acoustic coupler is an insulator, the pulse voltage can be applied directly to the shield layer without using an optical fiber link. The acoustic signal is boosted by a commercially available amplifier (Spectrum Instrumentation, SPA-1232), with a frequency range between dc and 10 MHz.

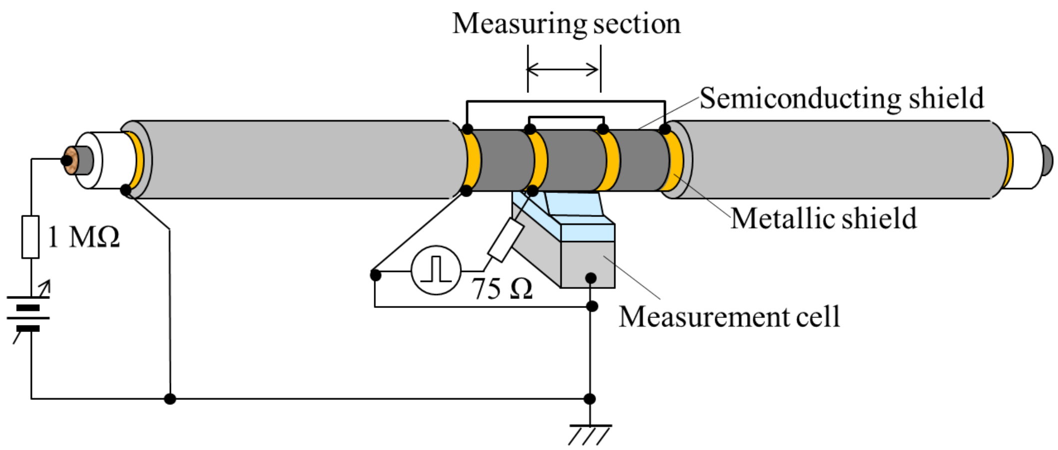

Fig. 5.7 Space charge measurement system by means of PEA method in full-size cable.

5.4. System Performance Evaluation

This section evaluates the sensitivity and signal clarity of the newly designed PEA cell compared with the conventional PEA cell. Two sets of experiments were conducted as follows:

1. Quantitative comparison of sensitivity using identical specimens and voltage conditions.
2. Waveform acquisition under high-voltage conditions using thick cable insulation to demonstrate practical applicability and spike noise suppression.

5.4.1. Sensitivity Comparison

To directly compare the sensitivity of the new and conventional PEA configurations, measurements were carried out on a 9-mm-thick polymeric insulation sample subjected to 10 kV DC bias voltage, 0.5 kV Pulse voltage and 400ns pulse width with 2500 repetition rate per second.

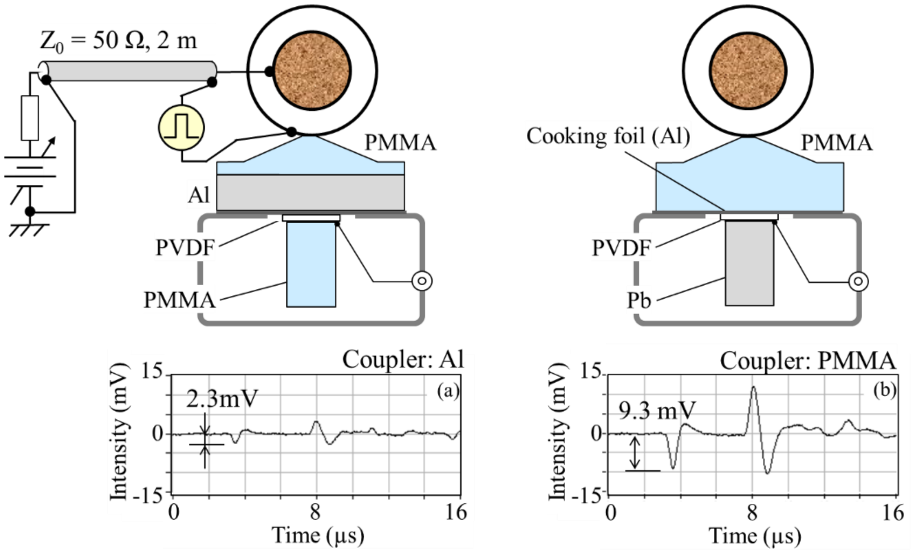

Fig. 5.8 Comparison of sensitivities of the new method (right) and the conventional method (left), using a cable with 9-mm thick insulation. DC 10 kV, pulse −0.5 kV 400 ns. PVDF: 110 μm-thick, metal backing: brass, Al coupler thickness: 30 mm. Intensity is input equivalent of the amplifier (PVDF output).
(a) Coupler: Al. (b) Coupler: PMMA [13]. Reprinted with permission from © 2022 IEEE.

In both cases, a coaxial cable was used not only to deliver the DC voltage but also as the coupling impedance for the pulse injection, ensuring minimal distortion and consistent transient behavior.

To standardize the acoustic boundary condition at the measurement interface, a PMMA spacer was introduced between the specimen and sensor stack in both systems. This guaranteed the equivalent acoustic coupling conditions and identical electrical boundary impedance for the applied probing pulse.

Each waveform was acquired via a wideband 60 dB amplifier, and the PVDF sensor output was digitized with a high-speed oscilloscope. The output voltage of the first arriving echo, corresponding to induced charge near the outer screen of the cable (ground side), was used as the sensitivity index. This first peak results from a rapid pressure change due to the displacement of space charges under the applied field.

Fig. 5.8 illustrates the comparative waveform outputs. The following observations were made, the conventional PEA configuration (with metallic coupler and PMMA backing) yielded a sensor output of 2.3mV (peak). Whereas The new PEA cell (using a polymeric coupler and lead backing) yielded a peak signal amplitude of 9.3mV under identical test conditions. This corresponds to a four-fold increase in output voltage amplitude, confirming that the new PEA cell achieves ~4× sensitivity improvement. This improvement rises primarily from:

1. Improved acoustic impedance matching which resulted in minimizing the wave reflection.
2. Enhanced piezoelectric conversion due to higher pressure transfer to the PVDF.
3. Reinforced reflective gain at the backing layer.

5.4.2. Spike Noise in HV Waveform

As previously mentioned, the acoustic coupler also serve as the delay line from the spike noise due to the pulse voltage application. A 55-mm-thick XLPS acoustic coupler (sound velocity ≈ 2400 m/s) was placed between the cable and PVDF sensor. This coupler serves as an acoustic delay line, introducing a propagation delay t_d of:

$$t_d = \frac{55\ \mathrm{mm}}{2400\ \mathrm{m/s}} \approx 20\ \mu\mathrm{s}. \tag{5.4}$$

To verify performance under realistic high-voltage conditions, the new PEA cell was tested using cross-linked polyethylene (XLPE) cable insulation with Inner screen radius ~28 mm and outer screen radius ~48 mm shows in Fig. 5.4, with −50 kV DC bias voltage, 0.9 kV Pulse voltage, 400 ns Pulse width, and 80,000 Averaging acquisitions (to suppress random noise).

The calculated delay agrees with the measured result as it delays $\approx 20\ \mu\mathrm{s}$, the delay effectively separates the acoustic signal from the initial electrical spike noise generated by pulse application. The acquired waveform, shown in Fig. 5.9, exhibits:

1. No observable overlap or ringing from the initial spike,
2. A first-peak amplitude of 4 µV at the PVDF sensor input, representing the charge density near the outer screen.

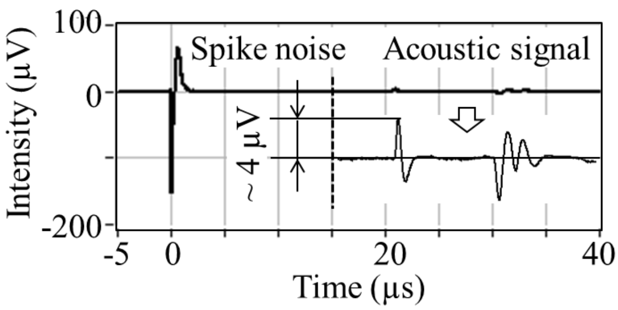

Fig. 5.9 20 mm-thick, DC 50 kV, pulse ~ 900V 400 ns. Intensity is input equivalent [13]. Reprinted with permission from © 2022 IEEE.

5.5. Signal Acquisition

The signal as acquired when a dc −50 kV and a pulse voltage of 0.9 kV with a width of 400 ns was applied to a 20-mm-thick cross-linked polyethylene (XLPE) cable insulation. 80000 acquisitions were averaged to obtain a single waveform. The outer radius of the inner screen and the inner radius of the outer screen were approximately 28 and 48 mm, respectively. A 55-mm thick XLPS block (sound velocity of about 2400 m/s) was used as the acoustic coupler.

Fig. 5.10 shows the acoustic signal waveforms obtained by applying dc 5, 10, 20, 30, 40, and 50 kV. It can be seen that the acoustic propagation time between the two screen electrodes was approximately 10μs. It is remarkable that even though the pulse voltage was not very high, the signal was clear even at a dc voltage of only −5 kV that corresponds to 0.25 kV/mm in average field strength.

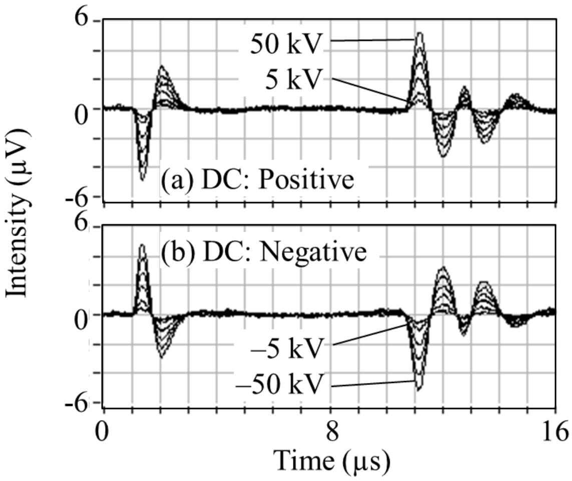

Fig. 5.10 20 Acoustic signal waveforms as acquired with 20 mm-thick insulation, applying dc 5, 10, 20, 30, 40, and 50 kV, pulse −0.9 kV 400 ns. Intensity is an input equivalent of the amplifier (PVDF output). (a) DC: positive. (b) DC: negative [13]. Reprinted with permission from © 2022 IEEE.

5.6. Signal Processing and Charge Profile Reconstruction

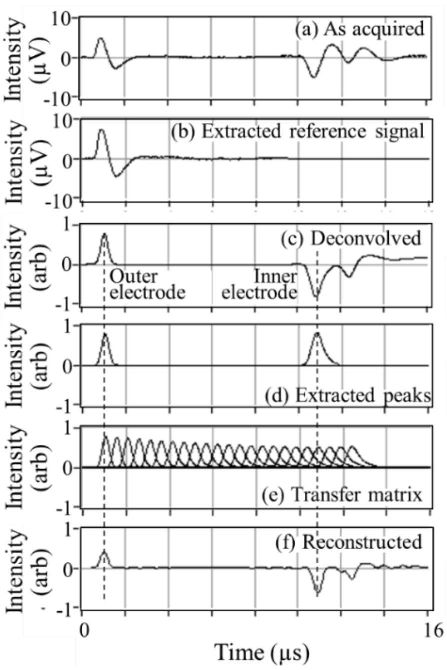

Fig. 5.11 Signal processing. (a) Reference as required. (b) Extracted reference signal. (c) Deconvolved. (d) Extracted peaks. (e) Transfer matrix. (f) Reconstructed [13]. Reprinted with permission from © 2022 IEEE.

Although the basics of signal processing can be found in the literature [6,7], we refer to Fig. 5.11 for an overview. The difference between signals before and after changing the dc voltage is attributed only to the charges on the screen electrodes, assuming that no change occurs in the space charge distribution during that time. Details are provided in [8]. The indicated waveform Fig. 5.11(a) is the waveform acquired by applying dc −50 kV and subtracting the waveform acquired immediately after the conductor was grounded. This process was done to remove the potential effect of any preexisting space charge and extract only the signals at the electrodes.

From the obtained differential signal Fig. 5.11(a), the one from the outer screen side is extracted using an appropriate window function waveform Fig. 5.11(b). This can be considered as the impulse response of the measurement system (including pulse waveform). This signal, namely $s0(r0, t)$, is proportional to the charge on the outer screen electrode, represented as

$$q_0 = \varepsilon_0 \varepsilon_r \frac{V_0}{r_0} \cdot \frac{1}{ln \frac{r_0}{r_i}} \tag{5.5}$$

where $\mathrm{r_0}$ and $\mathrm{r_i}$ are the positions of the outer and inner screen electrodes, ε_0 is the vacuum permittivity, ε_r is the relative permittivity of the cable insulation and v_0 is the equivalent applied voltage when acquiring the above reference waveform. q_0 has the same dimension as the surface charge density in the cylindrical coordinate system.

The entire signal is normalized (deconvolved) by this waveform, as it can be considered as the impulse response of the measurement system (including pulse waveform). This process results in waveform Fig. 5.11(c). In this process, the dual-domain deconvolution that combines time and frequency domain calculations has proved to be efficient, as described in [9,10].

Three peaks can be seen in waveform Fig. 5.11(c), the first peak at 0.8 μs represents the induced charge at the outer screen; the second peak at 10.4μs represents the charge at the inner screen. The third peak represents an artifact caused by the reflection at the conductor surface that should be eliminated from the analysis. Using appropriate window functions, the first and second signals, namely $s_1(r, t)$ and $s_1(r_i, t)$, are extracted as shown in diagram Fig. 5.11(d).

In the Chapter 3 has been discussed that the amplitude of an acoustic signal (sound pressure) generated at r decreases with the square root of the radius as it propagates to the outer screen, due to the divergence of the acoustic wave. Therefore, the reduction in sound pressure is represented as $(r/r_o)^{1/2}$. On the other hand, the pulsed electric field at r is r_o/r compared to that on the external electrode. Considering both the divergence of the acoustic wave and the divergence of the electric field, the sensitivity to unit charge density at position r (assuming no acoustic absorption) is represented as $(r_o/r)^{1/2}$. The charge density ratio of the inner to the outer screen is r_o/r . Considering the propagation characteristics of sound in addition, the signals from the inner and outer screen electrodes can be related as

$$S_1(r_i,\omega) = \left(\frac{r_o}{r_i}\right)^{3/2} \cdot S_1(r_0,\omega) \cdot exp(-\gamma(r_0 - r_i)) \tag{5.6}$$

$$\gamma = \alpha(\omega) + j\frac{\omega}{c(\omega)} \tag{5.7}$$

where S1 is the Fourier transform of s1, ω is the angular frequency, and α and c are frequency-dependent attenuation constant and sound velocity. The normalized spectrum of the signal detected when there is a charge of q_0 at position *r* is

$$S_2(r,\omega) = \sqrt{r/r_o} \cdot (r_o/r_i) \cdot S_1(r_0,\omega) \cdot exp(-\gamma(\omega) \cdot (r_0 - r)). \tag{5.8}$$

A component of the transfer matrix in discrete form is represented as:

$$h_{jk}(r_j,t_k) = IFT\left[\sqrt{r_j/r_o} \cdot (r_o/r_i) \cdot S_1(r_0,\omega_k) \cdot exp\left(-\gamma(\omega_k) \cdot (r_0 - r_j)\right)\right] \tag{5.9}$$

where IFT denotes inverse Fourier transform. The signal (deconvolved using s_0 as a reference signal) corresponding to the charge distribution $q(r)$ is

$$\begin{pmatrix} s_{\mathrm{tgt}}(t_1) \\ \vdots \\ s_{\mathrm{tgt}}(t_n) \end{pmatrix} \equiv \mathrm{S_{tgt}} = \begin{pmatrix} h_{11} & \cdots & h_{1m} \\ \vdots & \ddots & \vdots \\ h_{n1} & \cdots & h_{\mathrm{nm}} \end{pmatrix} \begin{pmatrix} q(r_1)/q_0 \\ \vdots \\ q(r_m)/q_0 \end{pmatrix} \equiv \mathrm{HQ} \tag{5.10}$$

Diagram Fig. 5.11(e) shows some of the components of the transfer matrix. In practice, many more components are generated so that the calculation result can be smoothly indicated. Several methods are known for solving (8) [11,12]. When the least-squares method is applied, the estimated value of the charge distribution is:

$$\widehat{\mathrm{Q}} = (\mathrm{H^T H})^{-1}\mathrm{H^T S_{tgt}}^{\mathrm{T}} \tag{5.11}$$

where *T* denotes transposition. Electric field and potential can be determined by integrating the charge distribution in the radial direction.

5.6.1. Charge and Field Profiles

Fig. 5.12 shows the measurement results of the full-scale (20 mm-thick insulation) cable at 5, 10, 20, 30, 40, and 50 kV dc. Fig. 5.12 (I) shows the results when positive dc voltages were applied to the conductor, Fig. 5.12 (II) shows the results for negative dc voltage. In both cases, the upper figure Fig. 5.12 (a) shows the calculated charge distribution at each dc voltage. Even when the dc applied voltage was as low as 5 kV, the peaks at the screen electrodes are clearly seen. The lower figure Fig. 5.12(b) shows the electric field distribution.

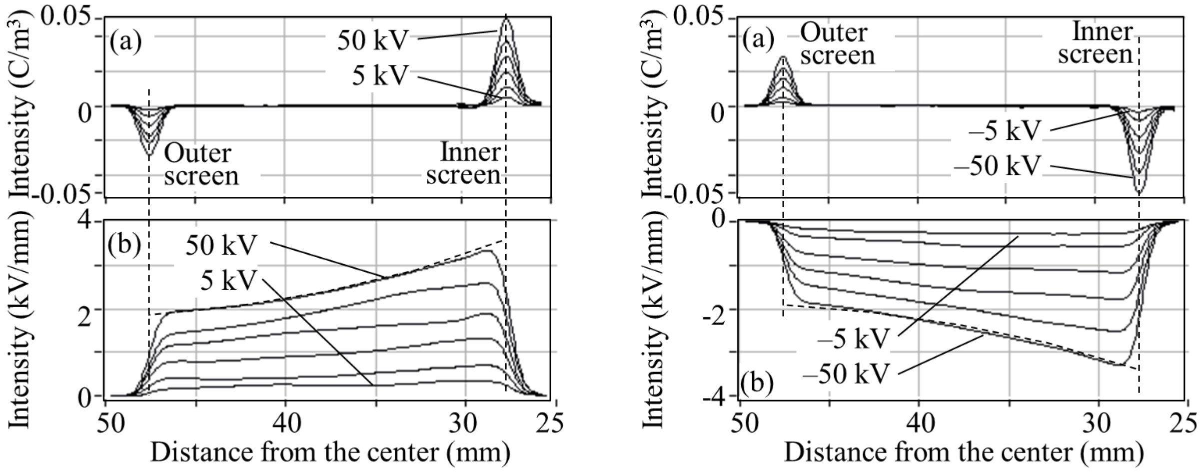

(A) Positive DC voltages

(B) Negative DC voltages

Fig. 5.12 (a) Charge density and (b) field intensity profiles at 5, 10, 20, 30, 40, and 50 kV dc voltages on the conductor. (I) Positive dc voltages. (II) Negative dc voltages [13]. Reprinted with permission from © 2022 IEEE.

The dashed line shows the calculated Laplace field at 50 kV dc. Each electric field distribution seems similar to that of the Laplace electric field.

Fig. 5.13 shows the charge density induced at inner and outer screen electrodes. Although these charges are surface charges the results measured with a finite spatial resolution have a dimension of volume charge density. Integrating each peak in the radial direction yields a dimension of surface charge density. Since there is almost no space charge in the insulation, the induced charges can be theoretically calculated assuming a Laplace field. The charge density shown in Fig. 5.13 agrees well with the value calculated assuming a Laplace field. In addition, the difference in charge density at 5 and 10 kV dc voltages is clearly discernible.

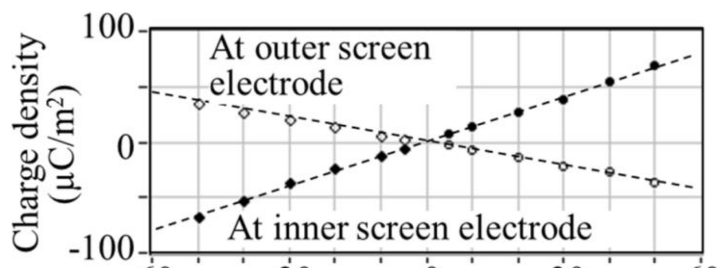

Fig. 5.13. Intensity of charges induced at inner and outer screen electrodes as a function of bias voltage. The dashed line corresponds to the Laplace field [13]. Reprinted with permission from © 2022 IEEE.

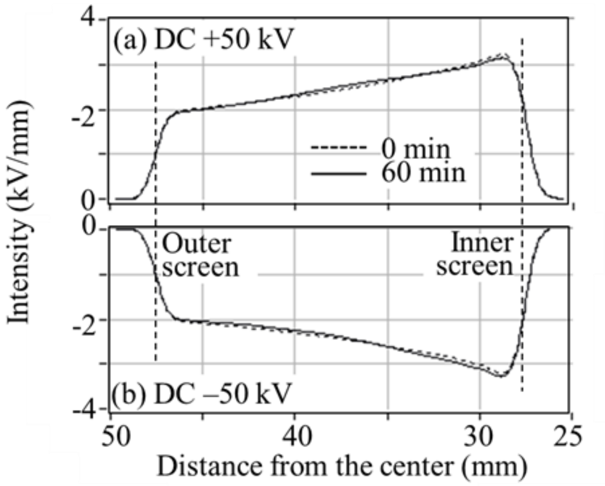

Fig. 5.14. Electric field intensity profiles at (a) +50 kV dc and (b) −50 kV dc voltages on the conductor [13]. Reprinted with permission from © 2022 IEEE.

The results shown in Fig. 5.12 and Fig. 5.13 suggest that the charge and electric field distributions can successfully be calculated even at 5 kV dc. The profiles were quite similar when negative dc voltages were applied, as indicated in Fig. 5.12 (II).

Fig. 5.14 shows the electric field distribution when +50 kV Fig. 5.14 (a) and −50 kV Fig. 5.14 (b) dc were applied to the cable conductor for 1 h, respectively, at room temperature. The solid line shows the electric field profile at 0 min, and the dashed line shows the electric field profile at 60 min. In the meantime, intermittent waveform acquisitions were performed every 15 min. As was expected, no significant change was observed because of the low applied voltage. However, the result showed the stability of the measurement including signal processing.

5.7. Summary

In this chapter A new method for measuring the space charge in full-size power cables has been proposed. The sensitivity of the new PEA cell using electrically insulative acoustic coupler was proved to be four times more sensitive compared to the conventional one using a metallic electrode as an acoustic coupler. Furthermore, since the electrically insulative acoustic coupler isolates the measuring system from the outer shielding layer of the cable, a proving pulse voltage can be applied onto the measuring section through the shielding layer while a DC high voltage is applied to the cable conductor. Data acquisition on a cable with 20 mm in insulation thickness was performed using 0.9 kV, 400 ns probing pulses with 80000 times of waveform averaging. Charge distribution and electric field distribution were successfully reconstructed by using an appropriate deconvolution technique, taking frequency dependent acoustic attenuation and dispersion into account. As a result of the experiment applying up to 50 kV DC, the accuracy of the electric field estimation was found to be 0.25 kV/mm or less, that can realize 2% of precision assuming 250 kV as an operation voltage.

Reference

[1] S. Zahra, T. Kawashima, Y. Murakami and N. Hozumi, “Small-size space charge measurement device for power cables by using electrically insulated acoustic coupler,” 2020 IEEE 3rd International Conference on Dielectrics (ICD), pp. 359–362, 2020.

[2] N. Hozumi and M. Hori., “Space charge measurement for full-scale HVDC cables Using pulsed-electroacoustic method,” Cigre Science & Engineering, no. 6, pp. 97-102, 2016.

[3] N. Hozumi, H. Suzuki, T. Okamoto, K. Watanabe and A. Watanabe, “Direct observation of time-dependent space charge profiles in XLPE cable under high electric fields,” IEEE Transactions on Dielectrics and Electrical Insulation, vol. 1, no. 6, pp. 1068–1076, 1994.

[4] N. Hozumi, T. Takeda, H. Suzuki and T. Okamoto, “Space charge behavior in XLPE cable insulation under 0.2-1.2 MV/cm dc fields,” IEEE Transactions on Dielectrics and Electrical Insulation, vol. 5, no. 1, pp. 82–90, 1998.

[5] K. Ono, “A comprehensive report on ultrasonic attenuation of engineering materials, including metals, ceramics, polymers, fiber-reinforced composites, wood, and rocks,” Appl. Sci., vol. 10, no. 7, p. 22-30, 2020.

[6] G. Rizzo, P. Romano, A. Imburgia, G. Ala, “Review of the PEA Method for Space Charge Measurements on HVDC Cables and Mini-Cables,” Energies, vol. 12, no. 18, p. 35-12, 2019.

[7] B. Vissouvanadin, T. T. N. Vu, L. Berquez, S. Le Roy, G. Teyssèdre, C. Laurent, “Deconvolution techniques for space charge recovery using pulsed electroacoustic method in coaxial geometry,” IEEE Transactions on Dielectrics and Electrical Insulation, vol. 21, no. 2, pp. 821–828, 2014.

[8] X. Li, S. Zahra, T. Kawashima, Y. Murakami and N. Hozumi, “Lock-in calibration for space charge measurement,” 2020 IEEE 3rd International Conference on Dielectrics (ICD), pp. 391–394, 2020.

[9] N. Hozumi, E. B. Prastika, S. Zahra, T. Kawashima and Y. Murakami, “Dual-domain deconvolution process applied to time-resolved quantitative dielectric measurement,” 2020 IEEE 3rd International Conference on Dielectrics (ICD), pp. 347–350, 2020.

[10] B. Prastika, S. Zahra, X. Li, T. Kawashima, Y. Murakami and N. Hozumi, “The application of signal processing using dual domain deconvolution for new space charge measurement method in HVDC full-size cables,” 2020 International Symposium on Electrical Insulating Materials (ISEIM), pp. 277–280, 2020.

[11] Y. Murkami, T. Sugiyama, T. Kasashima, M. Nagao and M. Fukuma, “Signal recovery of space charge distribution using acoustic property in PEA method,” 2015 IEEE 11th International Conference on the Properties and Applications of Dielectric Materials (ICPADM), pp. 344–347, 2015.

[12] K. Murata, Y. Li, Y. Tanaka, and T. Takada, “Recovery of acoustic signal distorted with attenuation and dispersion in pulsed electro-acoustic method,” IEEJ Trans. Fundamentals and Materials, vol. 115, no. 5, pp. 418–422, 1995.

[13] S. Zahra, S. Morita, M. Utagawa, T. Kawashima, Y. Murakami, N. Hozumi, P. Morshuis, C. Young-Il and K. Yoon-Hyoung, “Space Charge Measurement Equipment for Full-Scale HVDC Cables Using Electrically Insulating Polymeric Acoustic Coupler,” IEEE Transactions on Dielectrics and Electrical Insulation, vol. 29, no. 3, pp. 1053-1061, 2022.

Chapter 6 Space Charge Measurement in Scaled Cable Joint

6.1. Introduction

Space charge measurement is becoming the essential matter in the development process of an HVDC cable system. The cable joints that are used to connect two cables are known to be the weakest points and a defective joint could lead to a system failure. Poor installation or manufacturing process can be the cause of such defects. One of the most common reasons of cable accessory failure is electrical breakdown at the interface of two dielectric surfaces, which is a complicated phenomenon. The charge dynamic at the interface of the cable insulation and the joint body insulation is an important consideration when designing HVDC cable joint, as the space charge distribution at the cable joint is considered to be more complex than that of the cable body. Therefore, Space charge measurements are recommended to realize a reliable system and increase the security of electric power system.

Recent advancements in Pulse Electro-Acoustic (PEA) measurement technology have enabled accurate space charge measurements in full-size HVDC cable bodies [1-2]. Several studies, both experimental and simulation-based, have focused on space charge behavior in joint insulation systems [3-5]. However, literature remains limited when it comes to axisymmetric two-dimensional joint structures, despite some progress in simplified models such as multilayer flat samples [6-8] and coaxial joints without triple junctions [9-10].

As the new PEA cell has shown significant progress in term of sensitivity, it is discussed in chapter 5. This chapter describes the results of space charge measurements on a scaled cable joint model by using a newly proposed PEA cell with a 16-channel sensor array capable of automatically scanning along the joint and resulting in faster data acquisition. The distribution of the space charge along the interface between the cable and joint insulation, including the triple junction, was successfully obtained. From the results, the internal electric stress distribution was derived.

6.2. 16-Channel Array Sensor Design and Layout

Previous studies have reported improvements of the PEA cell by improving the sensitivity by 4~5 times which has been discuss in Chapter 5 Development of A High-Sensitivity PEA System for Full-Scale HVDC Cables. These improvements have resulted in an estimated electric field calculation accuracy of 0.25 kV/mm. A description of the new PEA device and signal propagation can be found in a previous report [11]. After successfully conducting a space charge measurement in a full-size cable, attempts have been made to apply this technique to measure space charge in a scaled cable joint model. However, the step of moving on from full size cable to a scaled cable joint presented some difficulties with the PEA cell. A longer time was required when measuring the space charge in a cable joint with a single sensor, resulting in time inefficiency. To address this issue, we have implemented a solution by increasing the number of sensors to measure the space charge in the cable joint. This solution, which is called a PEA cell with 16-channel sensor array, because it is made up of 16-channel piezoelectric sensor array positioned along the cable joint model. In Fig. 6.1 it is shown that the components of the PEA cell for the cable joint model is principally the same as those of the PEA cell for full-size cables we can refer to Chapter 5, except that the device is composed of 16-channel with mechanical relays for sequential scanning.

For the PEA cell with 16-channel sensor array a 180 mm long polystyrene block is used, acting as an acoustic coupler that maintains electrical isolation between the specimen and the acoustic sensor [1]. This allows us to apply a high voltage pulse to the specimen using the main body of the cable as the coupling impedance, while keeping the shielding layer at ground potential. Moreover, the trapezoidal shape is to retain the contact area between the specimen and coupler. To maintain ground potential at the sensor, a thin layer of aluminum film is used as an electromagnetic shield between the acoustic coupler and the sensor. A polyvinylidene difluoride (PVDF) piezoelectric sensor is divided into 16 segments, each with an aperture length of 10 mm and a 1 mm gap between the sensors created by removing the PVDF coating to allow each sensor to be separated from the others. A 10 mm wide metal backing is placed behind the sensor to further amplify the signal through positive reflection at the back of the sensor [1,11], each metal backing being separated by a 1 mm air gap. The scanner is approximately 175 mm long and is designed with 16 relays and a controller. The program on a personal computer controls the switching of the relays according to the timing, it allows the scanning process to be automated and sequential. A photograph of the internal and external structure of the PEA cell is shown in Fig. 6.2.

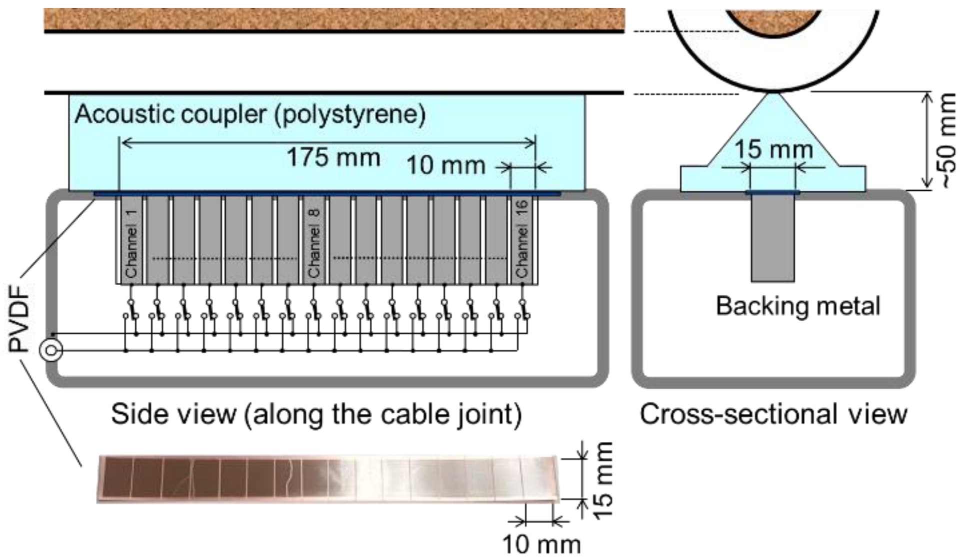

Fig. 6.1 Schematic diagram of PEA system with 16-channel sensor array, capable of scanning along the cable joint box [21]. Reprinted with permission from © 2024 IEEE.

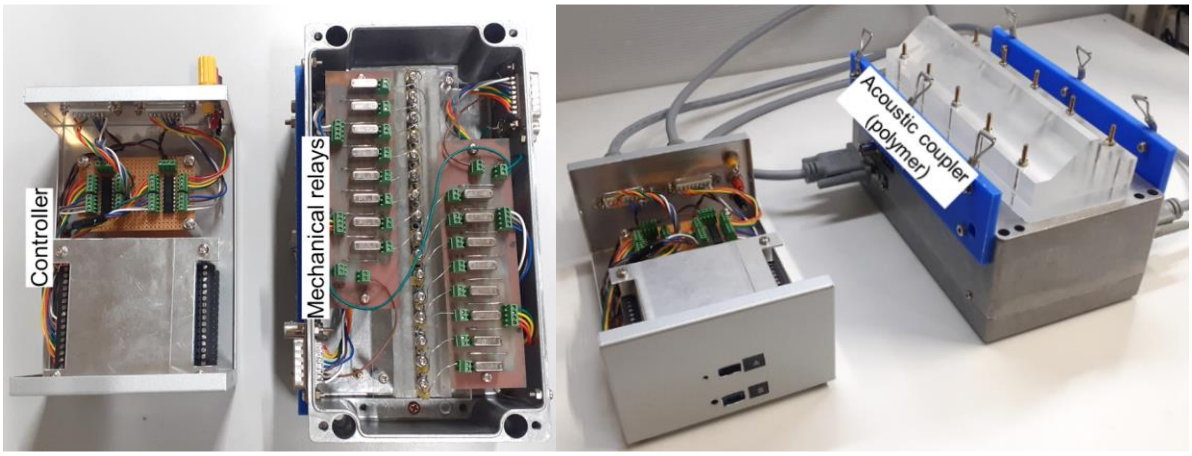

Fig. 6.2 Inside and outside view of the PEA cell completed with the controller these all are hand made in the lab [21]. Reprinted with permission from © 2024 IEEE.

6.3. Sound Field and Crosstalk Analysis in the PEA cell

Based on the previous improvement [1], a 16-channel array PEA sensor was created to measure the space charge in cable joint box. While PEA cell with 16 array sensor has been successfully assembled, the interchannel crosstalk has been unknown. Crosstalk in an image sensor could result from image-generated carriers having the ability to diffuse and be collected by a neighboring pixel which could result in invalid data. Therefore, further research is required to evaluate the PEA 16 array cell regarding crosstalk. In this study, we performed PEA measurement to evaluate the influence on the possibility of cross sound pressure detection within the PEA 16 array cell.

6.3.1. Analysis of the Receiving Sound Field

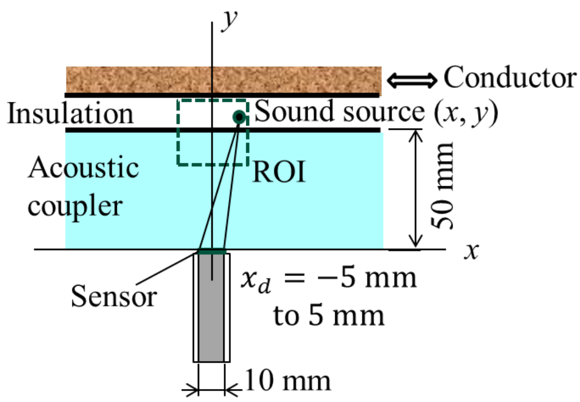

Fig. 6.3 A model for sound field analysis. ROI: Region of Interest.

As shown in the Fig. 6.3, the axial direction of the cable is *x* and the insulation thickness direction is *y*, and the two-dimensional received sound field in Cartesian coordinate system is analyzed. Since there is no significant difference in the sound velocity and acoustic impedance between the acoustic coupler and the sample, values of 2000 mm/µs as c and 2 Ns/m2 , which are close to those of polyethylene, are used as rough values.

Supposed the sound source position is (*x,y*) and the sensor extends from $x_d = -5$ mm to $+5$ mm. Assuming the impulse signal as the sound source with an estimated intensity of s_0 and a distance r from the sound source to the sensor extend (x_d), the signal detected by the sensor is:

$$s(x, y, t) \propto \int_{-x_d}^{x_d} \frac{1}{r} s_0\ (t - \frac{r}{c}) dx_d \tag{6.1}$$

$$r = \sqrt{(x - x_d)^2 - y^2} \tag{6.2}$$

The thickness of the acoustic coupler was set to 50 mm and the insulation thickness to 20 mm, and the signal intensity detected by the sensor, the signal originating from each sound source located in the region of interest (ROI), was calculated.

Fig. 6.4 shows the results of the calculation with different frequency characteristics of band-pass filters. In addition to the two-dimensional intensity profiles, the axial intensity profiles at the position directly above the acoustic coupler and at a position 10 mm above it are also shown in this figure. Each profile is normalized to the maximum intensity.

In practical signal processing, a Gaussian filter that leads to a symmetric time-directional blur is often used. If the half-width of the Gaussian filter in the time domain is 50 ns, which corresponds to a resolution of 100 µm in the thickness direction, the cutoff frequency is estimated as $\sqrt{2 \times \ln 2}/(2\pi \times 50\ \text{ns}/\sqrt{2 \times \ln 2})$, which is approximately 4.5 MHz.

Assuming a 4 - 4.5 MHz bandpass filter, the center wavelength is about 0.5 mm. The propagation distance from the sound source to the sensor differs by a maximum of about 1 mm inside the ROI, which is close to the wavelength, so interference fringes appear as shown in profile (a). If the frequency band is kept at 0.5 MHz and the frequency range is 1 - 1.5 MHz, the center wavelength is about 1.6 mm, so interference fringes are not visible as shown in profile (b), but the receiver sensitivity distribution becomes dull and the spatial resolution in the axial direction decreases. When the frequency band is set from 0.1 MHz to 4.5 MHz, there are no interference fringes and the spatial resolution in the axial direction is relatively good, as shown in profile (c).

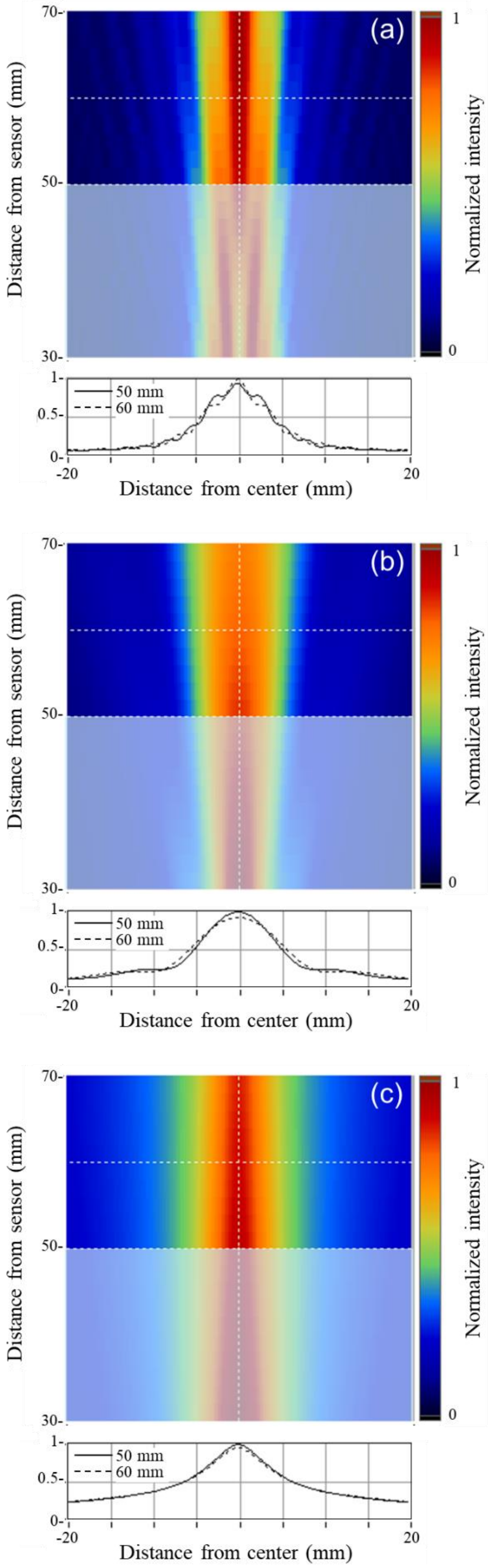

Fig. 6.4 (a) Band-pass filter with 4.0 - 4.5 MHz band width, (b) Band-pass filter with 1.0 - 1.5 MHz band width, (c) Band-pass filter with 0.1 - 4.5 MHz band width.

The results assuming a Gaussian filter with a half-width of 50 ns (standard deviation 42 ns) are shown in Fig. 6.5 The calculated results are close to those obtained assuming a bandpass filter with the frequency range from 0.1 MHz to 4.5 MHz.

The half-width of the axial intensity profile is about 10 mm, indicating that interference from adjacent sensors is generally avoided. Since the Gaussian filter passes even the DC component, its effect appears in the profile in Fig. 6.5, and the hem of the profile is wider than when a bandpass filter is applied, but the low-frequency components from sources at different axial positions do not change significantly, so it is thought that it does not have a significant effect on the spatial resolution.

To achieve conditions similar to those in the analysis, a PVDF transducer was placed in contact with an acoustic coupler and 16 sensors were scanned to measure the received sensitivity.

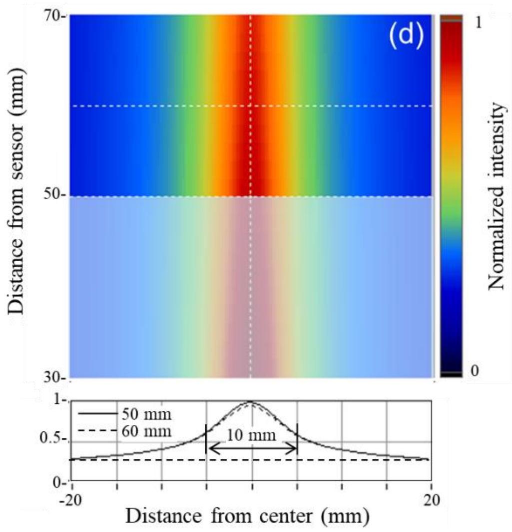

Fig. 6.5 Gaussian filter with 50 ns half width.

6.3.2. Measurement Method of Crosstalk Analysis

6.3.2.1. Application of The DC And Pulsed Voltage to the Cable Joint Model in Space Charge Measurement

The PEA method measures sound pressure generated by the interaction of a space charge and a pulsed electric field. Determining the magnitude and distribution of space charges at a cable joint is a critical process. A PEA cell array shows in Fig. 6.1, which is mechanically aligned with the measurement area and electrically connected to ground potential, is used for this measurement. The schematic diagram of the space charge measurement on a cable joint is shown in Fig. 6.11 Schematic diagram of space charge measurement system in cable joint model, with the joint box located between the cable bodies.

A cylindrical electrical conductor made of aluminum foil is wound around the cable, with the ends connected to ground potential. The guard electrode region around the measuring point is connected to a pulse generator that sends electric pulses through a 60m feeder line. When an electrical pulse is applied to the cylindrical conductor, it interacts with space charges in the insulation of the measurement section, generating acoustic signals that the PEA cell array detects to evaluate the magnitude and distribution of space charges. The acoustic signal is amplified by a commercial amplifier (Spectrum Instrumentation, SPA-1232) with a frequency range up to 10 MHz.

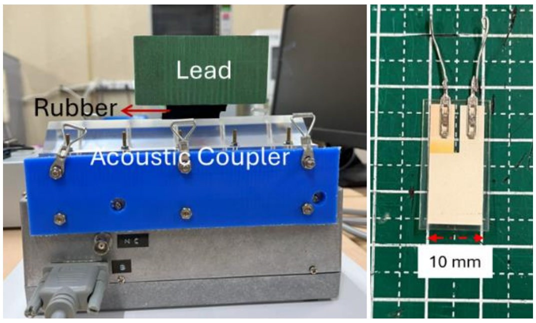

Fig. 6.6 Photograph the configuration of the PEA cell array (left), 10mm PVDF transducer (right) placed in between the rubber and acoustic coupler.

Fig. 6.6 shows the configuration of the PEA cell array in the crosstalk evaluation, where a 10 mm width and 0.11 mm thick PVDF transducer was placed between the lead and the acoustic coupler where in connection with pulse voltage. The lead was used as a weight to hold the PVDF transducer in place.

The results are shown in Fig. 6.7 Comparing the case of contact directly above the acoustic coupler and the case of contact through a 10 mm thick EPDM insulator, only the sensor directly below the transducer showed a response in both cases, and few response signals were observed from the other sensors. It proves that the cross talk between the sensor is minimum.

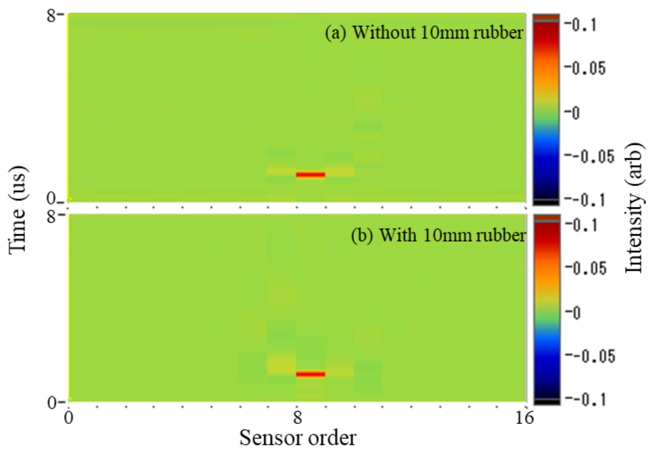

Fig. 6.7 (a) Normalized result with PVDF transducer in between lead and acoustic coupler (b) normalized result PVDF transducer in between 10mm rubber and acoustic coupler.

6.4. PEA Cell Uniformity Experiment

Uniformity among the sensors is a critical factor in the PEA array scanner, which consists of multiple sensors. Therefore, after assembling the PEA array scanner, the device is subjected to a uniformity test on a cable to assess the consistency among its channels. As we know, the PEA cell used for cable joint measurement is composed of 16 array sensors, and each sensor may exhibit different detection intensities. Hence, the uniformity test is conducted using a cable that is assumed to have a uniform composition along its length, making it suitable for evaluating the uniformity of the sensor array.

6.4.1. Measurement Test Specimen

The uniformity test is carried out on a cable with a 6mm thick insulation. It is believed that the cable's structure is uniform which consists of the same material and thickness. The uniformity test was performed in a -30kV DC and +1kV pulse. Fig. 6.8 shows the schematic diagram of the uniformity test.

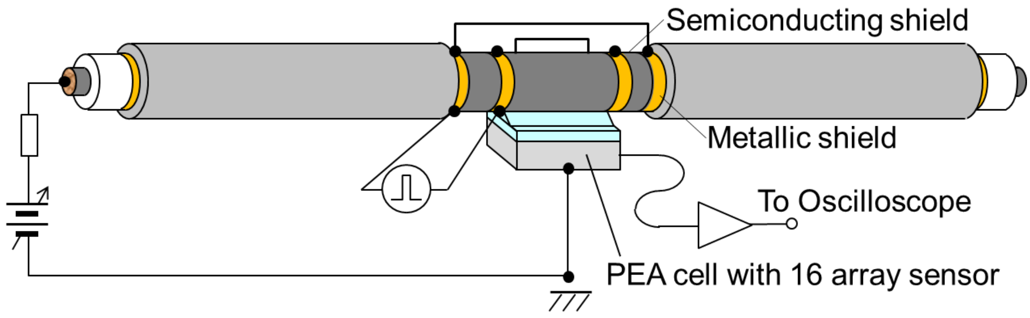

Fig. 6.8 Schematic diagram of PEA cell uniformity test.

6.4.2. Result

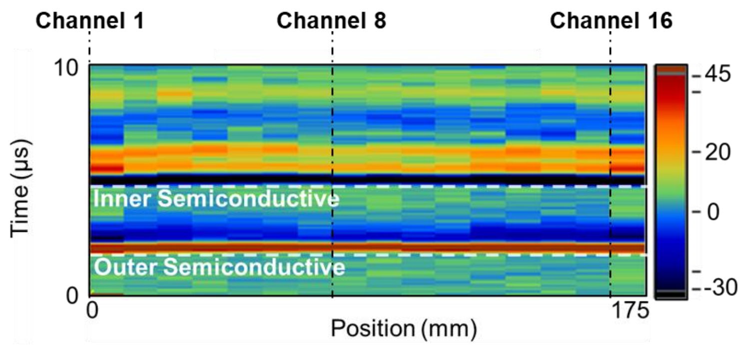

Fig. 6.9 Uniformity test result on 6mm thick cable.

It is proven that the PEA scanner is uniform by looking at Fig. 6.9. The cable's intensity was determined to be identical. The outer semiconductive layer of the cable, which is in contact with the acoustic coupler, indicated by the positive charge, exhibits uniformity of intensity across the 16 channels. The inner semiconductive layer, indicated by the negative charge layer, exhibits the same uniformity of intensity across the 16 channels. Also, Furthermore, the PEA cell is capable of detecting the signal shape originating from the conductor side. This signal appears non-uniform, which can be attributed to the strand structure of the conductor and possible internal reflections, causing the detected signal to appear distorted.

6.5. Space Charge Measurement Using the PEA Method – Experimental Setup

6.5.1. Measurement Test Specimen

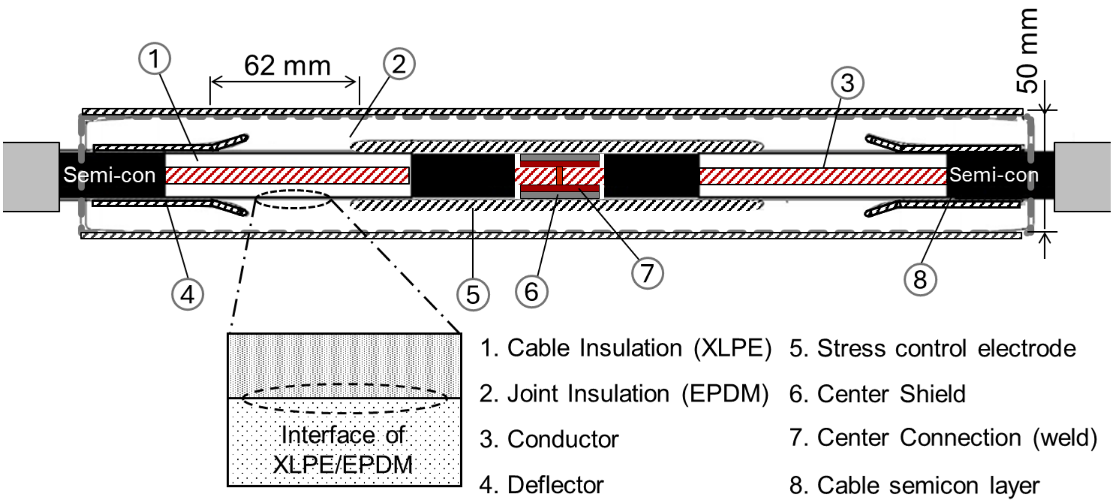

Fig. 6.10 Diagram of cable joint model box specimen.

Table 6.1 Dielectric and Acoustic Properties of Tested Materials [21]. Reprinted with permission from © 2024 IEEE.

Material	Thickness (mm)	Relative permittivity (ε_r)	Sound velocity (m/s)	Acoustic Impedance Z_a (kg/m²/s)
EPDM	11	3.0	1400	1900
XLPE	6.6	2.2	2100	

Fig. 6.10 shows the cross-section of the cable joint model, which has a diameter of 50 mm and consists of two types of insulation materials. The two dielectric materials composing the insulation of the test specimen are XLPE for the HVDC cable and EPDM for the joint. The thicknesses are 11 mm for EPDM and 6.6 mm for XLPE, respectively. The electrical properties of these materials are summarized in Table 6.1 Dielectric and Acoustic Properties of Tested Materials

6.5.2. Experimental Method

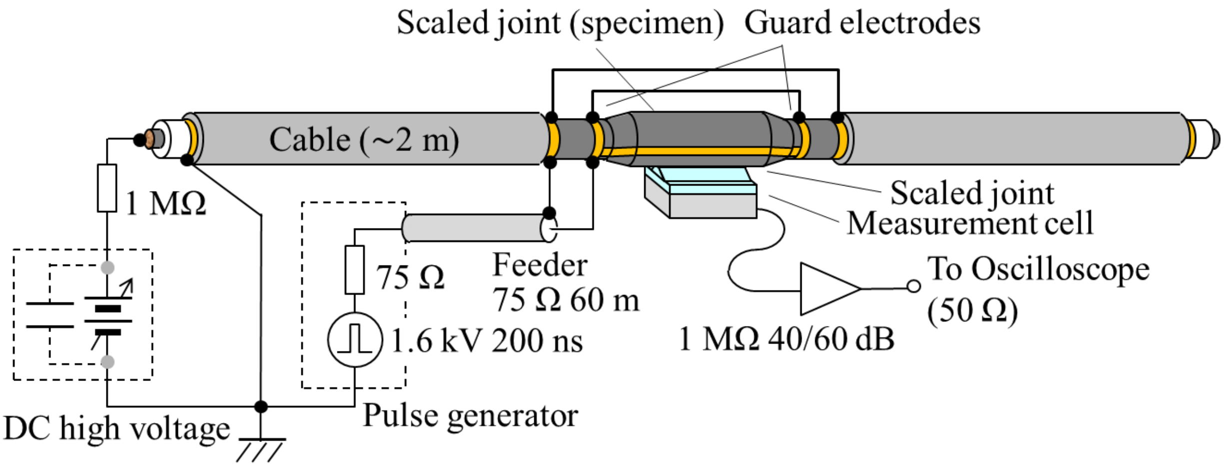

Fig. 6.11 Schematic diagram of space charge measurement system in cable joint model [21]. Reprinted with permission from © 2024 IEEE.

In this study, the scaled cable joint box specimen consists of 11 mm thick insulating rubber (EPDM) and 6.6 mm thick XLPE cable insulation. The scaled joint box was in the center, with 2-m cable length on each side. The deflector electrode is made of semi-conductive material and makes the field distribution as uniform as possible. The stress control electrode is also installed on a cable joint serves as live electrode and electric screen of the connector [12], where both the deflector and the stress control electrode are made of the same base polymer as EPDM, but with added carbon filler.

Fig. 6.11 shows a schematic representation of the space charge measurement system for a scaled cable joint model. The cable conductor is energized by a DC high-voltage source, whereas the shield layers of the cable and joint are kept at ground potential in terms of DC voltage.

An 800 V, 200 ns electrical pulse generated by the pulse generator was directly applied to the measuring region 1000 times at rate of 50 applications/second, and without employing the coupling capacitor [19,20] throughout the guard electrodes which were wound on both sides of the measuring region and connected by a wire as shown in Fig. 6.11. These electrodes were connected to a pulse generator through a 60m feeder line. The PEA cell is mounted in the measuring region in order to acoustically couple together.

Following the successful assembly of a cable joint layout system, the PEA cell is installed on the sample as shown in Fig. 6.12. The objective of this installation is to observe the accumulation of space charge at the interface of the multi-dielectric material boundary. Therefore, the PEA cell is arranged along the joint, from the deflector electrode to the stress control electrode. The acoustic signal is amplified by a commercial amplifier (Spectrum Instrumentation, SPA-1232) with a frequency range up to 10 MHz.

Upon the application of 1000 pulses to each channel and the subsequent averaging of the responses, the scanning results were collected sequentially from channel 1 to 16, taking approximately 6 minutes. Fig. 6.13 shows the photograph of the layout of space charge measurement in the cable joint model.

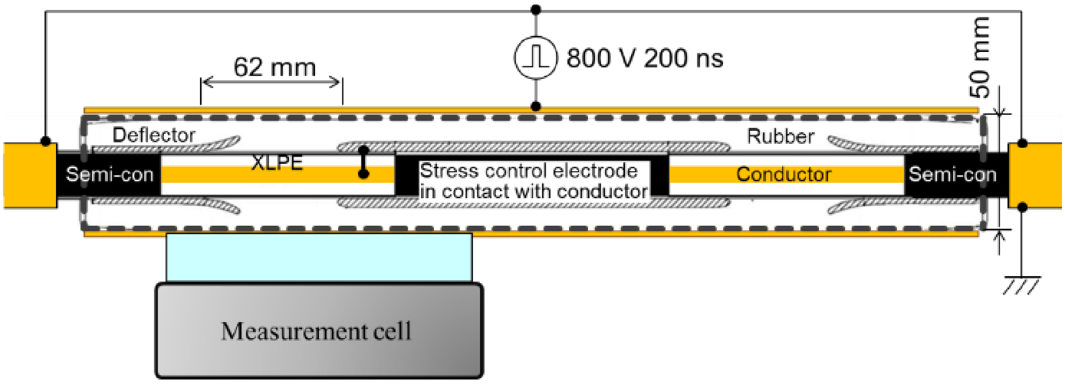

Fig. 6.12 Schematic diagram illustrating the arrangement of PEA cell onto the cable joint box [21]. Reprinted with permission from © 2024 IEEE.

Fig. 6.13 Photograph of the layout of the space charge measurement system in the scaled cable joint model [21]. Reprinted with permission from © 2024 IEEE.

6.6. Measurement Results

The acquired signal consists of 16 waveforms, combined from the scanning results obtained using the PEA cell. Fig. 6.14 (a) shows the complete acquired signal, measured from the deflector side to the steering electrode side. The deflector side corresponds to the position near 0 mm, while the steering electrode side starts from the middle. Fig. 6.14 (b) shows one of the individual waveform, specifically from the right end (channel 16, refer to Fig. 6.1), which is part of the acquired signal shown in Fig. 6.14 (a). In summary, Fig. 6.14 (a) is composed of 16 waveforms obtained from different scanning positions across the specimen.

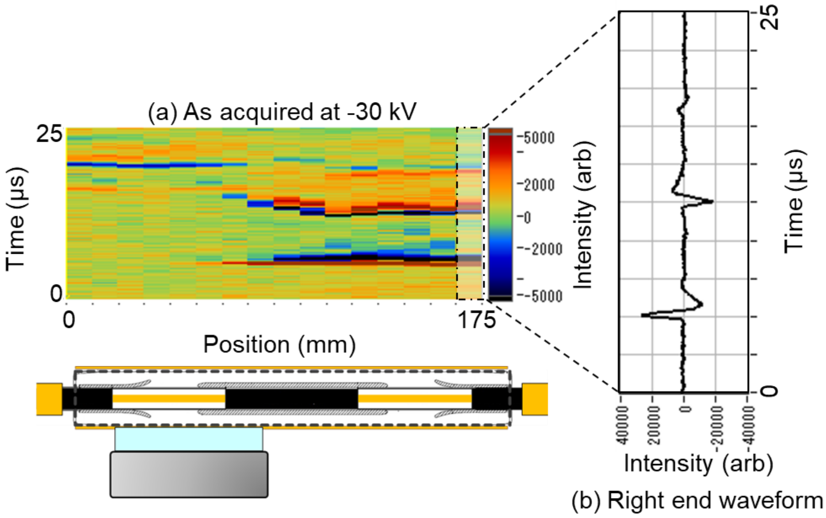

Fig. 6.14 Acquired joint box scanning result.

6.7. Signal Processing

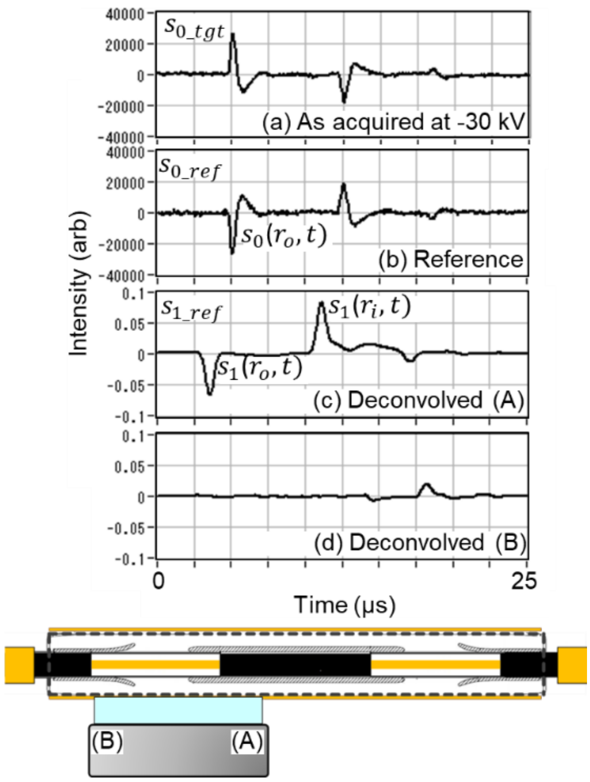

Fig. 6.15 Signal Processing (a) as acquired at -30 kV and 800 V pulse, (b) Reference signal taken by subtracting the waveform acquired at 0 kV from the signal at +30kV, (c) deconvolved (A/Channel 16), (d) deconvolved (B/Channel1) [21]. Reprinted with permission from © 2024 IEEE.

The PEA method detects a pressure wave generated by the interaction between internal charges and an external electric pulse [14], but the waveform as acquired does not directly correspond to the space charge distribution, as it has been affected by the frequency dependence of the measurement system including pulse signal and amplifier. The signal has also been affected by the acoustic propagation properties of the specimen.

An example is shown in Fig. 6.15. Waveform (a) was taken by the sensor at channel 16 located close to the center of the stress control electrode. This was acquired by applying DC -30 kV and a pulse voltage of 800 V peak between the conductor and shield screen of the joint. The first and second peaks from the left side correspond to the outer shield and stress control electrode, respectively.

Waveform (b) was taken by subtracting the waveform at 0 kV DC from the waveform at +30 kV DC in order to eliminate a potential effect from pre-existing space charges [14]. This waveform, assumed to be similar to the result when +30kV DC is applied which is composed of only induced charges on the electrodes. It was employed as a reference signal in order to perform the deconvolution processing. The first peak represents the induced charge on the outer semiconductor electrode of the joint, while the second peak represents the charge on the stress control electrode, and the last peak is an artifact due to reflection, while the time difference between the first and second peak is 7.4 microseconds.

Various deconvolution processes are required to obtain a signal corresponding to the charge distribution of the acquired signal. In this study on PEA, the deconvolution of the first kind is defined as the correction of the frequency characteristics of the measurement system, including the pulse voltage waveform and the signal detection system. Deconvolution of the second kind is defined as the correction of the signal from each point within the specimen to the detection point and involves variables such as the specimen geometry and material composition, the electroacoustic conversion coefficients, and the acoustic propagation characteristics including frequency-dependent attenuation and velocity dispersion [16,17].

Deconvolution of the first kind can be performed using waveform (b). The calibration signal $s_{0\_ref}(t)$ is obtained by applying a bias voltage V_0 and eliminating the effect of space charge caused by the charges on the outer and inner electrodes. When the outer electrode signal is separated from the reference signal without space charge, by using an appropriate window function and indicated as $s_0(r_o, t)$, it corresponds to the impulse response of the measurement system, and the magnitude is proportional to the charge that appears on the outer electrode represented as;

$$q_0(r_0, V_0) = \varepsilon_0 \varepsilon_r \frac{V_0}{r_0} \cdot \frac{1}{ln\frac{r_0}{r_i}} \tag{6.3}$$

Where r_0 and r_i are the positions of the outer and inner screenelectrodes, ε_0 is the vacuum permittivity, ε_r is the relative permittivity of the insulation and V_0 is the applied voltage during the acquisition of the above reference waveform. q_0 has the same dimension as the surface charge density in a cylindrical coordinate system. Table 6.1 shows the acoustic properties which were used in this study.

Normalizing the measured signal $s_{0\_tgt}(t)$ by $s_0(r_o,t)$ results in a signal $s_{1\_tgt}(t)$ corrected for the frequency response of the measurement system.

$$s_{1\_tgt}(t) = IFT\left[\frac{S_{0\_tgt}(\omega)}{S_0(r_o,\omega)}\right] \tag{6.4}$$

And S denote the Fourier transform of s, ω the angular frequency, IFT the Inverse Fourier transform, and t represent time.

Next, deconvolution of the second kind is performed, for which it is necessary to obtain the acoustic propagation parameters of the insulation system. The insulation system consists of two materials with different acoustic and dielectric properties. Since the insulation employed at the location of channel 16 is EPDM only, the acoustic parameters of EPDM can be obtained by extracting the signal from the two electrodes shown in waveform (c) and comparing their frequency components. This method is similar to the signal processing of the cable body presented in the previous report [1].

Waveform (c) is the reference waveform $s_{0_{ref}}(t)$ normalized by $s_0(r_o,t)$.

$$s_{1\_ref}(t) = IFT\left[\frac{S_{0\_ref}(\omega)}{S_0(r_o,\omega)}\right] \tag{6.5}$$

The signal components whose sources are the outer and inner electrodes are extracted and defined as $s_1(r_o,t)$ and $s_1(r_i,t)$, where the peak polarity has been adjusted to calculate the attenuation factor [1]. The ratio of the pulse electric field on the outer and inner electrode is r_o/r_i and the ratio of the charge densities on the outer and inner electrodes due to bias voltage is r_0/r_i. Since the acoustic energy is proportional to $r_\mathrm{i}/r_\mathrm{o}$, the sound pressure is proportional to $\sqrt{r_\mathrm{i}/r_\mathrm{o}}$. Therefore:

$$S_1(r_i,\omega) = \ (r_o/r_i)^{3/2}\cdot S_1(r_0,\omega)\cdot exp(-\gamma(\omega)\cdot(r_0-r_i)) \tag{6.6}$$

$$\gamma = \alpha(\omega) + j\frac{\omega}{c(\omega)} \tag{6.7}$$

where α and c are frequency-dependent attenuation constant and sound velocity, respectively. Thus, γ can be determined as:

$$\gamma = \ln\left[(r_o/r_i)^{-3/2}\frac{S_1(r_i,\omega)}{S_1(r_0,\omega)}\right]/(r_i-r_0) \tag{6.8}$$

Using the channel 1 signal in waveform (d), the peaks represent the outer and inner semiconductor of the cable, and the acoustic parameters of the XLPE can be estimated in a similar way.

Fig. 6.16 Two-dimensional profile of -30kV after the deconvolution of the first kind(a) shows a combination of acquired waveforms presented in a two-dimensional profile and Fig. 6.16(b) shows profile Fig. 6.16(a) after deconvolution of the first kind.

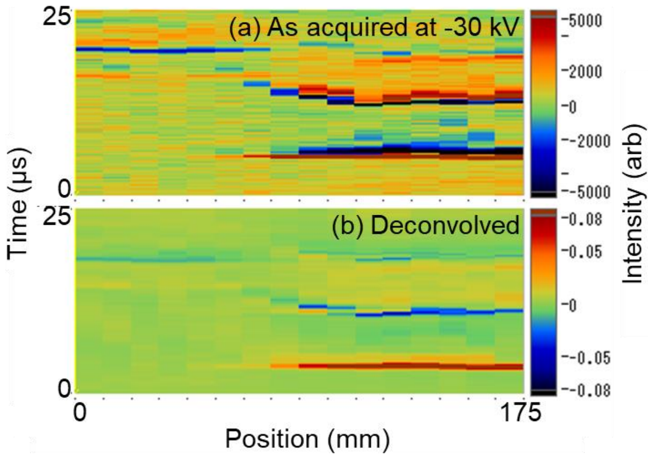

Fig. 6.16 Two-dimensional profile of -30kV after the deconvolution of the first kind [21]. Reprinted with permission from © 2024 IEEE.

Fig. 6.17 (a), (b), and (c) show the -30 kV and +30 kV profiles after the deconvolution of the first kind and the potential distribution calculated by the finite element method, respectively.

Fig. 6.17 (c) illustrates the inception and propagation of the electroacoustic pressure wave. It is assumed that a space charge is created by DC application and subjected to a pulsed electric field that is determined only by a permittivity distribution. The pressure wave propagating to the sensor is assumed to travel radially (i.e., the formation of a straight beam was assumed). The local electric field which interacts with the charge can be divided into radial and axial components, of which only the radial component produces a pressure wave propagating to the sensor. The axial component may produce a shear wave; however, it can be discriminated against because its sound speed is as low as half the pressure wave.

Finite element method (FEM) was employed to perform the field analysis. Fig. 6.17 (a), (b), and (c) compare the deconvolved intensity profiles and potential distribution calculated by FEM. Note that the profiles were up-sampled. Each point of the intensity profile was correlated with the radial component, corresponding to the local field that was calculated from the potential profile. The local charge intensity was normalized by the radial component of local field intensity

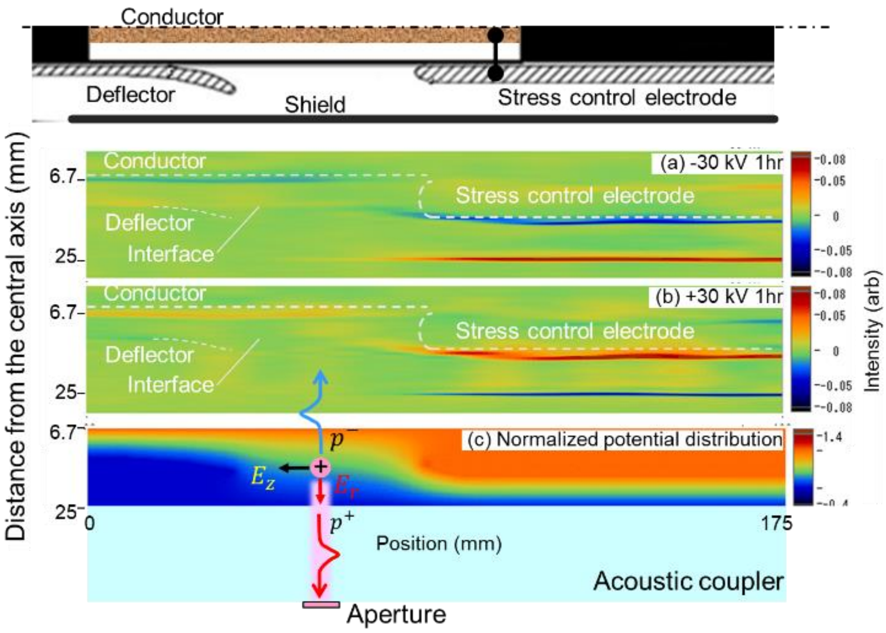

Fig. 6.17 Acoustic response profiles after applying -30 kV for 1 hr and +30 kV for 1 hr in comparison with the pulse voltage distribution obtained using a finite element method (FEM) [21]. Reprinted with permission from © 2024 IEEE.

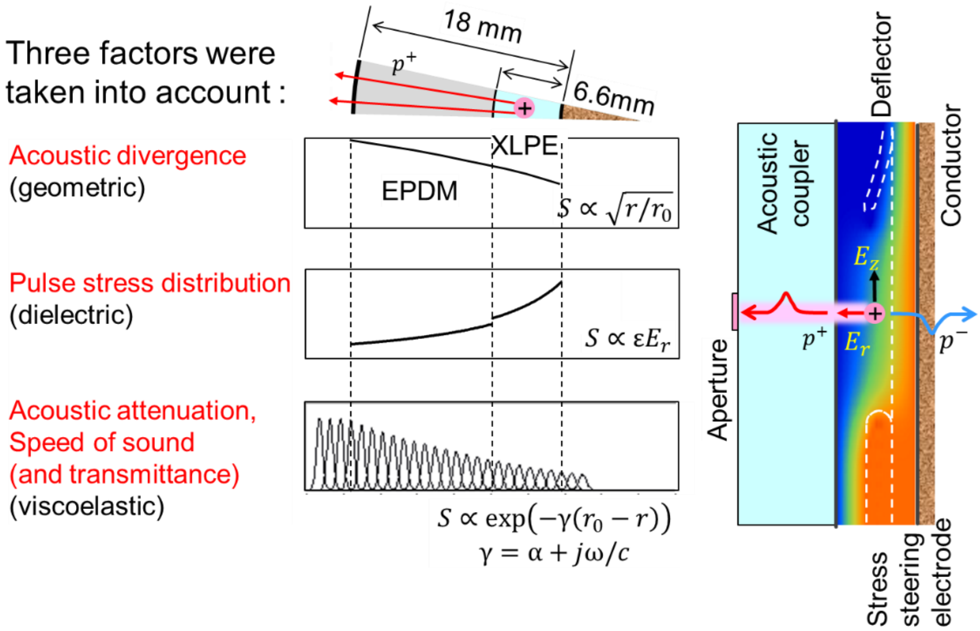

Fig. 6.18 Factors taken into account in order to construct the transfer matrix for deconvolution of the second kind [21]. Reprinted with permission from © 2024 IEEE.

Fig. 6.18 shows the process of constructing the transfer matrix from this result and the acoustic parameters determined by equation (6.7). In the absence of acoustic attenuation, the sound pressure decreases with $\sqrt{r/r_o}$ when it is generated at position r and reaches r_o in the cylindrical coordinate system. The source strength is considered to be proportional to the radial component of the pulse electric field. The acoustic propagation characteristics are taken into account, and the transfer function is calculated from each point to the outermost layer, i.e., the position of contact with the acoustic coupler.

Multi-layer structure is not considered when the sound source is inside the EPDM. When the sound source is inside the XLPE, the signal emitted from the source propagates to the outermost layer of EPDM. The signal arriving at the sensor depends on the transfer function from the sound source to the outermost layer of XLPE and the transfer function of the entire thickness of the EPDM. Since the EPDM insulation and the semiconducting deflector are based on the same polymer, they are considered acoustically uniform. In addition, we assume that the reflection at the XLPE-EPDM interface is small and not included in the components of the transfer matrix. Considering these factors, the normalized spectrum of the signal detected when there is a charge (charge density) q_0 at position (r, z) with z the coordinate along the axis of the joint is:

$$S_2(r,\omega) = \begin{cases} S_1(r_o,\omega)\, e_{pr}(r,z)\sqrt{r/r_0}exp\,\{-(r_o - r)\gamma^{EPDM}(\omega)\}, & if\ r > r_{int} \\ S_1(r_o,\omega)\, e_{pr}(r,z)\sqrt{r/r_0}exp\,\{-(r_o - r_{int})\gamma^{EPDM}(\omega) - (r_{int} - r)\gamma^{XLPE}(\omega)\}, & if\ r < r_{int} \end{cases} \tag{6.9}$$

$e_{pr}(r, z)$ is the radial component of the local pulsed electric field normalized by the pulsed electric field acting on the reference point (outer electrode in Ch.16).

r_{int} is the location of the interface between EPDM and XLPE. Thus, the discretized transfer matrix is:

$$h_{jk}(r_j, t_k, z_l) = \begin{cases} IFT\left[S_1(r_o,\omega)\, e_{pr}(r_j,,z_l)\,\sqrt{r_j/r_0}\exp\{-(r_o - r_j)\gamma^{EPDM}(\omega)\}\right], & if\ r_j > r_{int} \\ IFT\left[S_1(r_o,\omega)e_{pr}(r_j,,z_l)\sqrt{r_j/r_0}\,\exp\{-(r_o - r_{int})\gamma^{EPDM}(\omega) - (r_{int} - r_j)\gamma^{XLPE}(\omega)\}\right], & if\ r_j < r_{int} \end{cases} \tag{6.10}$$

The signal (deconvolved by using s_0 as a reference signal) corresponding to the charge distribution $q(r)$ is:

$$\begin{pmatrix} s_{1\_tgt}(t_1) \\ \vdots \\ s_{1\_tgt}(t_n) \end{pmatrix} = \begin{pmatrix} h_{11} & \cdots & h_{1m} \\ \vdots & \ddots & \vdots \\ h_{n1} & \cdots & h_{nm} \end{pmatrix} \begin{pmatrix} \dfrac{q(r_1)}{q_0} \\ \vdots \\ \dfrac{q(r_m)}{q_0} \end{pmatrix} \equiv \mathrm{HQ} \tag{6.11}$$

(9) and (10) show some of the components of the transfer matrix. In practice, many more components are generated so that the calculation result can be smoothly indicated. Several methods are known for solving (6.11) [15, 17,18]. When the least-squares method is applied, the estimated value of the charge density distribution is:

$$\widehat{\mathrm{Q}} = (\mathrm{H^T H})^{-1}\mathrm{H^T} {S_{1_{tgt}}}^{\mathrm{T}} \tag{6.12}$$

Where T denotes transposition. Electric field and potential can be determined by integrating the charge distribution in the radial direction.

6.7.1. The Result of Deconvolution Analysis

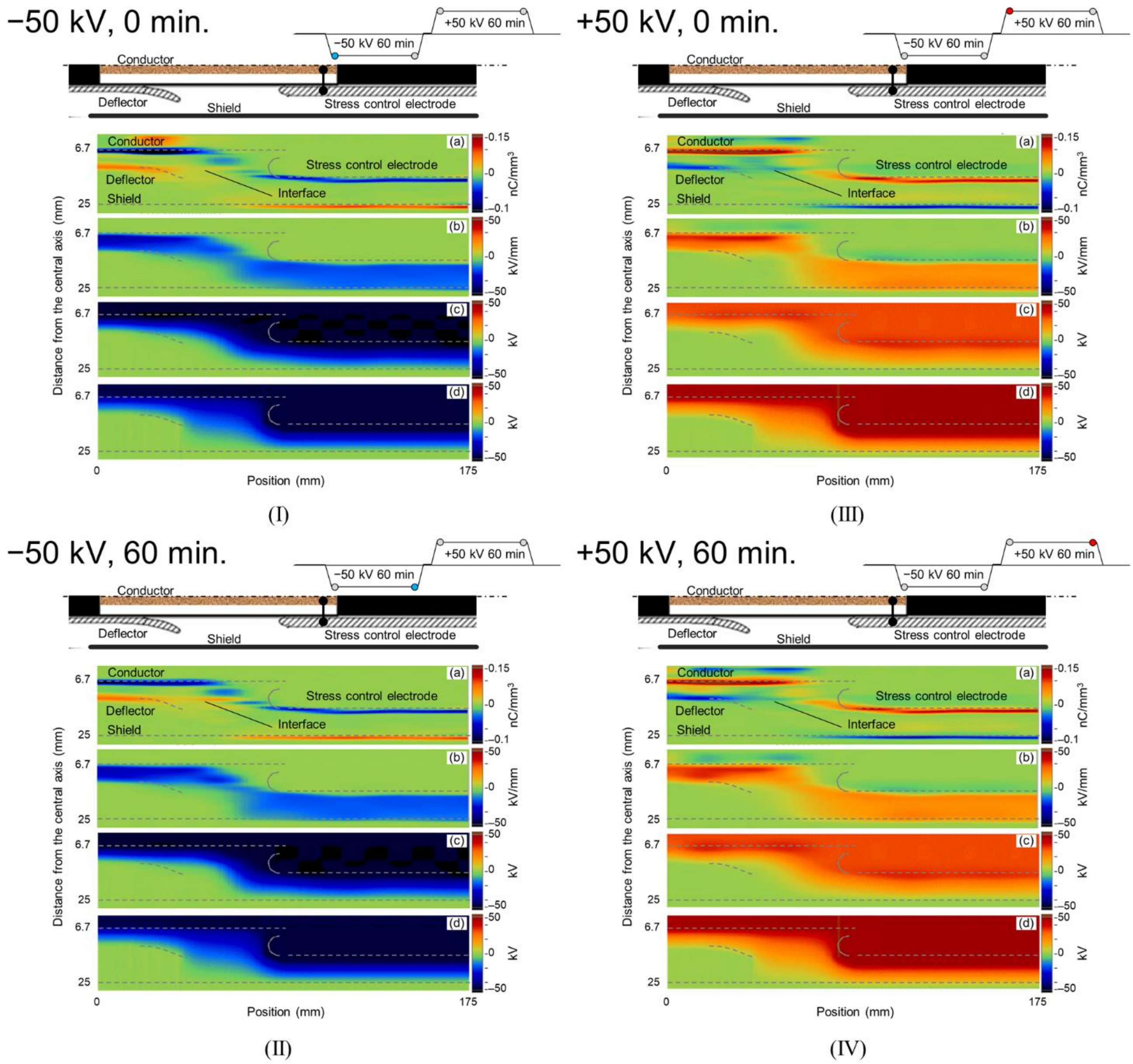

Fig. 6.19 Deconvolved 2D waveform indicated by (I), (II), (III), (IV). Completed with (a) charge distribution (b) electric field (c) potential distribution (d) FEM calculation result [21]. Reprinted with permission from © 2024 IEEE.

Fig. 6.19 shows the charge density (a), electric field (b) and potential distribution (c) after full deconvolution. Profiles I to IV show the results immediately after applying -50 kV to the conductor, after 60 minutes, immediately after applying +50 kV, and after 60 minutes, with the polarity reversal. The results obtained were up-sampled in the axial direction. This was done to make the profile smoother.

In addition to the profiles at each time, the electric field distribution assuming no space charge accumulation calculated by FEM (d) is also shown for reference.

As shown in profile I, immediately after the application of the -50kV bias voltage, we can observe the charge along the interface described in the figure, this is probably due to the difference in permittivity between XLPE and EPDM which created a charge response at the interface. Furthermore, the charge profile was almost free of space charge, the absence of any significant charge prior to the application of voltage indicates that the distribution of the electric field can be assumed to be a Laplace field.

As a result, the potential distribution is briefly similar in shape to the potential induced by the pulse voltage, which was calculated by the FEM analysis.

As shown in profile II, positive charge is distributed along the interface after a bias voltage of -50 kV has been applied for 60 minutes.

This phenomenon is known as Maxwell-Wagner type interfacial polarization, in which a discontinuity between the dielectric constant and conductivity causes an interface polarization with a certain time constant.

On the other hand, no significant charge is seen on the tip of the deflector, both shortly after and 60 min after the bias voltage application. This is due to the potential peak on the deflector shifted towards the interface, and as a result, the electric field in the XLPE region increased.

Immediately after the polarity reversal, negative charges appear relatively quickly along the interface around the deflector, as shown in profile III, followed by no significant change, as shown in profile IV.

It was expected that the transient response would be approximately symmetrical between negative and positive applications, but the present results contradict this. In other words, the time constant appears to be shorter during the formation of interfacial polarization after polarity reversal than before polarity reversal.

Thus, apart from the permittivity difference that causes an immediate interfacial charge after voltage application, the difference in charge formation under negative bias voltage and after polarity reversal can be explained by the generation of carriers due to the charge injection property that might be different depending on the polarity and the possibility that the polarity reversal occurred in the state of space charge formation, which enhances the electric field on the rubber side resulting in higher conductivity (due to the non-linearity of conductivity). However, the present experiment was terminated when the bias voltage was applied for 60 min each for negative and positive, so not enough information was available to study the electrical properties in detail. We also realize that cable joints have non-uniform and complex components. Therefore, there are still many possible improvements to optimize the results of our study.

In addition, the EPDM layer was a taped insulation, which is considered to have different electrical properties to the actual cable joint insulation system.

6.8. Summary

In this chapter, the application of the Pulse Electro-Acoustic (PEA) method for space charge measurement in cable joint models was presented. A preliminary study was conducted on a scaled joint model using a 0.8 kV, 200 ns pulse voltage with 1000 waveform averages, confirming the feasibility of the approach. A newly developed PEA cell in Chapter 5, incorporating a 16-channel piezoelectric sensor array and a polymer acoustic coupler, was introduced. Signal reconstruction was successfully performed on a cable joint model with 6.6 mm thick XLPE and 11 mm thick EPDM insulation layers, utilizing a deconvolution method that accounted for acoustic divergence, pulse field intensity, and acoustic attenuation. The resulting charge, electric stress, and potential distributions were visualized as 2D cross-sectional profiles, enabling the identification of space charge accumulation along the interface of the joint. These studies demonstrate that the application of the PEA method to full-size cable joints is not only practical but also promising for future diagnostics.

Reference

[1] S. Zahra, S. Morita, M. Utagawa, T. Kawashima, Y. Murakami and N. Hozumi, P. Morshuis, Y. Cho,Y. Kim, "Space Charge Measurement Equipment for Full-Scale HVDC Cables Using Electrically Insulating Polymeric Acoustic Coupler," IEEE Transactions on Dielectrics and Electrical Insulation, vol. 29, no. 3, pp. 1053-1061, 2022.

[2] S. Morita, N. Fuse, T. Takahashi, T. Takahashi, S. Zahra and N. Hozumi, "Space Charge Measurement of 23-mm-Thick XLPE Cable at Ambient and High Temperatures," IEEE Transactions on Dielectrics and Electrical Insulation, vol. 29, no. 4, pp. 1491-1497, 2022.

[3] T. T. N. Vu, G. Teyssedre, and S. L. Roy, "Electric field distribution in HVDC cable joint in Non-Stationary Conditions," Energies, vol. 14, no. 17, pp. 1-17, 2021.

[4] Stancu, P. V. Notingher, P. Notingher and M. Lungulescu, "Space charge and electric field in thermally aged multilayer joints model," IEEE Transactions on Dielectrics and Electrical Insulation, vol. 23, no. 2, pp. 633-644, 2016.

[5] Y. Zhan, G. Chen and M. Hao, "Space charge modelling in HVDC extruded cable insulation," IEEE Transactions on Dielectrics and Electrical Insulation, vol. 26, no. 1, pp. 43-50, 2019.

[6] T. Tohmine, T. Fujitomi, H. Miyake, Y. Tanaka, Y. Ida and Y. Inoue, "Measurement of space charge accumulated in multi-layered samples composed of different insulators used in the joints of DC transmission cables," 2017 International Symposium on Electrical Insulating Materials (ISEIM), Toyohashi, Japan, pp. 299-302, 2017.

[7] R. Bodega, P. H. F. Morshuis and J. J. Smit, "Space charge measurements on multi-dielectrics by means of the pulsed electroacoustic method," IEEE Transactions on Dielectrics and Electrical Insulation, vol. 13, no. 2, pp. 272-281, 2006.

[8] T. T. N. Vu, G. Teyssedre, B. Vissouvanadin, S. L. Roy and C. Laurent, "Correlating conductivity and space charge measurements in multi-dielectrics under various electrical and thermal stresses," IEEE Transactions on Dielectrics and Electrical Insulation, vol. 22, no. 1, pp. 117-127, 2015.

[9] P. H. F. Morshuis, R. Bodega, D. Fabiani, G. C. Montanari, L. A. Dissado and J. J. Smit, "Dielectric Interfaces in DC Constructions: Space Charge and Polarization Phenomena," 2007 IEEE International Conference on Solid Dielectrics, Winchester, UK, pp. 450-453, 2007.

[10] R. Bodega, G. Perego, P. H. F. Morshuis, U. H. Nilsson and J. J. Smit, "Space charge and electric field characteristics of polymeric-type MV-size DC cable joint models," CEIDP '05. 2005 Annual Report Conference on Electrical Insulation and Dielectric Phenomena, 2005., Nashville, TN, USA, pp. 507-510, 2005.

[11] S. Zahra, T. Kawashima, Y. Murakami and N. Hozumi, "Small-size Space Charge Measurement Device for Power Cables by Using Electrically Insulated Acoustic Coupler," 2020 IEEE 3rd International Conference on Dielectrics (ICD), Valencia, Spain, pp. 359-362, 2020.

[12] G. Mazzanti, J. Castellon, G. Chen, J.C. Fothergill, M. Fu, N. Hozumi, J.H. Lee, J. Li, M. Marzinotto, f. Mauseth, P. Morshuis, C. Reed, I. Troia, A. Tzimas, and K. Wu, "The insulation of HVDC extruded cable system joints. Part 1: Review of materials, design and testing procedures," IEEE Transactions on Dielectrics and Electrical Insulation, vol. 26, no. 3, pp. 964-972, 2019.

[13] T. Maeno and K. Fukunaga, "High-resolution PEA charge distribution measurement system," IEEE Transactions on Dielectrics and Electrical Insulation, vol. 3, no. 6, pp. 754-757, Dec. 1996.

[14] X. Li, S. Zahra, T. Kawashima, Y. Murakami and N. Hozumi, "Lock-in Calibration for Space Charge Measurement," 2020 IEEE 3rd International Conference on Dielectrics (ICD), Valencia, Spain, pp. 391-394, 2020.

[15] B. Vissouvanadin, T. T. N. Vu, L. Berquez, S. L. Roy, G. Teyssèdre and C. Laurent, "Deconvolution techniques for space charge recovery using pulsed electroacoustic method in coaxial geometry," IEEE Transactions on Dielectrics and Electrical Insulation, vol. 21, no. 2, pp. 821-828, 2014.

[16] M. Fu, G. Chen, A. E. Davies and J. Head, "Space charge measurements in cables using the PEA method:-signal data processing considerations," ICSD'01. Proceedings of the 20001 IEEE 7th International Conference on Solid Dielectrics (Cat. No.01CH37117), Eindhoven, Netherlands, pp. 219-222, 2001.

[17] B. Prastika, S. Zahra, X. Li, T. Kawashima, Y. Murakami and N. Hozumi., "The Application of Signal Processing Using Dual Domain Deconvolution for New Space Charge Measurement Method in HVDC Full-Size Cables," 2020 International Symposium on Electrical Insulating Materials (ISEIM), Tokyo, Japan, pp. 277-280,2020.

[18] N. Hozumi, E. B. Prastika, S. Zahra, T. Kawashima and Y. Murakami, "Dual-domain Deconvolution Process Applied to Time-resolved Quantitative Dielectric Measurement," 2020 IEEE 3rd International Conference on Dielectrics (ICD), Valencia, Spain, pp. 347-350, 2020.

[19] N. Hozumi, H. Suzuki, T. Okamoto, K. Watanabe and A. Watanabe, "Direct observation of time-dependent space charge profiles in XLPE cable under high electric fields," IEEE Transactions on Dielectrics and Electrical Insulation, vol. 1, no. 6, pp. 1068-1076, Dec. 1994.

[20] N. Hozumi and M. Hori., "Space charge measurement for full-scale HVDC cables Using pulsed-electroacoustic method," Cigre Science & Engineering, no. 6, pp. 97-102, 2016.

[21] S. Zahra, M. Utagawa, T. Kawashima, Y. Murakami, N. Hozumi, P. Morshuis, C. Young-Il and K. Yoon-Hyoung,"Two-Dimensional Space Charge Measurement in Cable Joint Model Using the Pulsed Electroacoustic Method," IEEE Transactions on Dielectrics and Electrical Insulation, vol. 31, no. 5, pp. 2350-2357, 2024

Chapter 7 Conclusion and Future Perspectives

In this chapter, the conclusions of the overall research that has been carried out are presented. The main focus of the study is the development of a measurement device, the improvement of the measurement system at the cable joint, as well as an alternative approach to space charge measurement on HVDC cables. The evaluation of the system was carried out taking into account the factors affecting the measurement accuracy. The main results of this research are summarized and described in the following sections.

7.1. Conclusion

Measurement Cell

In chapter 5 it was experimentally demonstrated that the sensitivity of the newly proposed measurement cell with a polymeric acoustic coupler was about four times higher than that of the conventional type that uses a metal electrode as an acoustic coupling material. Moreover, the insulating acoustic coupler has the advantage that the cable under test and the measurement system can be electrically isolated. This makes it possible to create an axial potential difference in the outer screen electrode of the cable under test while keeping the measurement system at ground potential, and consequently to apply a pulse voltage across the insulation layer at the measurement section.

Central Research Institute of Electric Power Industry has proposed a similar method of applying voltage, but since the metallic electrode was used as the acoustic coupler, an optical fiber link was used to ensure isolation between the shielding layer of the cable and the measurement system, which made the measurement system complicated. The electrically insulative acoustic coupler is believed to be a good solution.

In practical experiments, the amplifier and oscilloscope were yet connected through a fiber optic link for safety reasons, but the amplifier and optical transmitter were placed at ground potential, realizing easier power supply to these devices.

PMMA, which is easily available in the market, can be used as an acoustic coupler, however, since it has a relatively high sound velocity among polymers, it is necessary to make this part thicker in order to let it function sufficiently as a delay line to avoid the spike noise. Cross-linked polystyrene, which was used for the practical cable measurement in this study, is considered to be more suitable for this purpose because of its higher acoustic transparency and lower sound velocity compared to PMMA.

Probing Pulse

Since the spike noise cannot be removed by taking an arithmetic average of the waveforms, the pulse voltage must be kept as low as possible avoid the correlation noise. The pulse voltage used in this experiment was only 0.9 kV, which is relatively low for a measurement of this insulation thickness. On the other hand the pulse width can be freely changed to increase the spectral intensity at low frequencies. In the measurement 400 ns was preferable for realizing both good sensitivity and repetition rate.

If the pulse voltage is low, the time required to charge the capacitor in Fig. 5.5 can be shortened, and the voltage repetition frequency can be increased. As long as the spike noise can be reduced, the number of additive averages can be increased to reduce the random noise. In this experiment, we achieved 80,000 waveform averages within 50 seconds due to the high repetition rate.

Even though many times of averaging may significantly reduce the random noise, a high dynamic range should be retained in order to capture both noise and acoustic signal in each acquisition. The A/D conversion with 15-bit resolution realized an apparent sensitivity of 1.5 nV per bit in terms of PVDF sensor output whereas as high as 20 μV of noise signal was captured as well in each acquisition.

These measurement conditions were determined by try and error within the limitations of the hardware, so there is a possibility that more favorable conditions can be found. Since various signal processing has been performed for calculating the charge and electric field distribution, it is difficult to evaluate the effective sensitivity only by means of the signal-to-noise ratio of the originally acquired waveform.

Pulse Voltage Application

In the application of pulsed electroacoustic method, a coupling capacitor is basically required to apply a sharp pulse voltage across the insulation as well as applying a high DC voltage. In order to avoid the use of the capacitor that would be very large in scale in the case of full-size cable measurement, we proposed to use the cable specimen itself as a pulse coupler. However, as the cable is finite in its length, it may work as a resonator and disturb the pulse voltage across the insulation, depending on the frequency component of the pulse voltage. A calculation in frequency domain in Chapter 4 shows that the resonance is significant when the cable is as long as 10 m. Longer cable may cause resonance at low frequency, but it would be less significant because of attenuation thorough the cable specimen. A good pulse waveform across the insulation was seen when the cable length was as short as 2 m, however it is considered that too short cable specimen would lead to the reduction in the sensitivity.

Accuracy of Electric Field Estimation

The purpose of this series of experiments was to verify that sufficient sensitivity could be obtained for space charge measurement of full-scale cables. Due to the limitation of the facility a dc voltage much lower than the operating voltage was applied. Therefore, almost no space charge evolution was found. However, induced charges on the screen electrodes were clearly observed under 50 kV dc. The Laplace field in the absence of space charge was reproduced even at dc voltages lower than 50 kV, and there was no significant difference in the results even after multiple measurements. This suggests that the measurement performance was satisfactory, taking into account that the measurement system treats both induced charge and space charge in the same way.

It is remarkable that even at pulse voltage as low as 0.9 kV, the sensitivity was sufficient to calculate the charge and electric field distributions with an applied dc voltage of only 5 kV. Assuming the operating voltage to be 250 kV, this suggests that the charge distribution and electric field can be calculated with an precision better than 2%. The method will be further improved and applied to various cable samples to help evaluate insulation performance.

PEA Cell With 16 Array Sensor

The device relies on the previous improvements that have enhanced its sensitivity by a factor of four in Chapter 5. However, we found that the different compositions along the cable joint made our single-sensor PEA device not effective enough for measuring multiple points, requiring an extended time period for the measurement process. In order to deal with this issue, we have successfully created A new PEA cell composed of a 16-channel piezoelectric sensor array and coupled with a polymer acoustic coupler for the space charge measurement in cable joint. Furthermore, the results show the charge, electric stress, and potential distribution were indicated as a 2D cross-sectional profile, which allowed identification of the charge distribution along the interface of the cable joint.

7.2. Recommendations for Future Research

In this study, space charge measurements were successfully performed on a full-size HVDC cable as well as on a scaled cable joint using the proposed PEA cell, which has four times higher sensitivity than the conventional PEA cell. The measurement results at the cable joint are presented in the form of a two-dimensional charge distribution on a cross section. In order to approximate the real field conditions, space charge measurements at full-size cable joints need to be performed in the future.

The effect of temperature and time on charge accumulation was not fully evaluated in this study because the measurements were terminated after 60 minutes of DC voltage and pulse application. Therefore, long-term testing and temperature testing in PEA systems and cable joints are very important. To date, space charge measurements have been successfully performed on 23 mm thick XLPE cables under room temperature and high temperature conditions [1].

In addition, longer duration and higher voltage tests are needed to understand the charge behavior under extreme conditions at cable joints. This is important because space charge measurements on full-size XLPE cables under load cycling conditions have also been successfully performed by [2]. Therefore, further development needs to focus on full-size cable joints to complete the overall system understanding. Other important parameters, such as material conductivity, which were not included in this study, should also be investigated to gain a more complete picture of charge accumulation in HVDC joint systems.

Reference

[1] S. Morita, N. Fuse, T. Takahashi, T. Takahashi, S. Zahra and N. Hozumi, “Space Charge Measurement of 23-mm-Thick XLPE Cable at Ambient and High Temperatures,” IEEE Transactions on Dielectrics and Electrical Insulation, vol. 29, no. 4, pp. 1491-1497, 2022.

[2] S. Morita, N. Fuse, T. Takahashi, T. Matsubara, Y. Murata, S. Zahra, N. Hozumi, “Space Charge Measurement of Full-size 23-mm-thick XLPE Cables in Load Cycle Condition,” International Symposium on HVDC Cable Systems Jicable HVDC’21, no. 12, pp.1-6, 2021.

Acknowledgements

First of all, I would like to express my sincere gratitude to all those who have provided guidance, encouragement, and warm support throughout the preparation of this paper.

I am deeply grateful to Professor Yoshinobu Murakami and Associate Professor Tomohiro Kawashima of Toyohashi University of Technology for their continuous guidance and encouragement throughout the course of this research and who gave me the opportunity to pursue this Doctoral degree. Their detailed advice on the structure and content of this paper has been invaluable, and I would like to extend my heartfelt thanks to them.

I would also like to express my sincere gratitude to the examiners, Professor Hirofumi Takikawa and Professor Ryoji Inada, and Professor Kazuhiro Takahashi for their valuable advice and constructive feedback during the preparation of this thesis.

I am particularly thankful to Professor Naohiro Hozumi. His guidance, encouragement, patience, and unwavering support from beginning to end have been crucial to my academic journey. I have learned so much under his mentorship, and words cannot fully express how grateful I am to have been his student. The support and knowledge he generously shared with me have shaped both my research and personal growth. I truly believe there could not have been a better teacher for me.

I would also like to express my gratitude to LS Cable and System Co., Ltd for cooperating on this research by providing cable and joint model specimens for space charge measurements.

Special thanks to Dr. Peter Morshuis for his constant support and insightful discussions, which greatly enhanced my critical thinking and deepened my understanding of research. His guidance during journal and paper preparation, as well as his advice on navigating academic and personal challenges, has been truly invaluable.

I am equally grateful to Dr. Harry Orton for his generous support and encouragement throughout my research, PhD, and life. His friendship and thoughtful discussions about the PhD journey and life beyond academia have been a source of strength and inspiration.

I gratefully acknowledge the support of the Amano Institute of Technology Scholarship.

I am eternally thankful to my family, especially my parents, for their boundless support, wise counsel, prayers, and unconditional love. To my sisters and all of my family, thank you for your constant encouragement.

Special thanks to Mas Satwiko and Rayhan, my Indonesian fellows, for their timely help and encouragement, especially during my most critical deadlines. Meeting you both was truly a blessing in this journey.

My appreciation also goes to the members of Hozumi Lab and Kawashima Lab for their friendship, unforgettable experiences, and the valuable knowledge shared throughout my studies, which made my life in Japan much easier and more enjoyable.

To everyone I cannot mention individually whom I have met along this academic path, thank you for your kindness, support, help, and encouragement.

Publication List

PEER REVIEWED JOURNAL

1. **Shafira Zahra**, Shosuke Morita, Masaki Utagawa, Tomohiro Kawashima, Yoshinobu Murakami, Naohiro Hozumi, Peter Morshuis, Cho Young-Il and Kim Yoon-Hyoung, "Space Charge Measurement Equipment for Full-Scale HVDC Cables Using Electrically Insulating Polymeric Acoustic Coupler," IEEE Transactions on Dielectrics and Electrical Insulation, vol. 29, no. 3, pp. 1053-1061, 2022. (Chapter 5)

2. **Shafira Zahra,** Masaki Utagawa, Tomohiro Kawashima, Yoshinobu Murakami, Naohiro Hozumi, Peter Morshuis, Cho Young-Il and Kim Yoon-Hyoung, "Two-Dimensional Space Charge Measurement in Cable Joint Model Using the Pulsed Electroacoustic Method," IEEE Transactions on Dielectrics and Electrical Insulation, vol. 31, no. 5, pp. 2350-2357, 2024. (Chapter 6)

3. Shosuke Morita, Norikazu Fuse, Toshihiro Takahashi, Tsuguhiro Takahashi, **Shafira Zahra** and Naohiro Hozumi, "Space Charge Measurement of 23-mm-Thick XLPE Cable at Ambient and High Temperatures," IEEE Transactions on Dielectrics and Electrical Insulation, vol. 29, no. 4, pp. 1491-1497, Aug. 2022.

INTERNATIONAL CONFERENCE

1. **Shafira Zahra**, Tomohiro Kawashima, Yoshinobu Murakami and Naohiro Hozumi, "Small-Size Space Charge Measurement Device for Power Cables by Using Electrically Insulated Acoustic Coupler," IEEE 3rd International Conference on Dielectrics (ICD), Valencia, Spain, pp. 359-362, 2020. (Chapter 5).

2. Naohiro Hozumi, Edo Bagus Prastika, **Shafira Zahra**, Tomohiro Kawashima and Yoshinobu Murakami, "Dual-domain Deconvolution Process Applied to Time-resolved Quantitative Dielectric Measurement," 2020 IEEE 3rd International Conference on Dielectrics (ICD), Valencia, Spain, pp. 347-350, 2020.

3. Edo Bagus Prastika, **Shafira Zahra**, Xiaoxin Li, Yoshinobu Murakami, Tomohiro Kawashima, Naohiro Hozumi and Young-Il Cho, "The Application of Signal Processing Using Dual Domain Deconvolution for New Space Charge Measurement Method in HVDC Full-Size Cables," 2020 9th International Symposium on Electrical Insulating Materials (ISEIM), Tokyo, Japan, pp. 277-280, 2020.

4. Xiaoxin Li, **Shafira Zahra**, Tomohiro Kawashima, Yoshinobu Murakami and Naohiro Hozumi, "Lock-in Calibration for Space Charge Measurement," 2020 IEEE 3rd International Conference on Dielectrics (ICD), Valencia, Spain, pp. 391-394, 2020.

5. Shosuke Morita, Norikazu Fuse, Toshihiro Takahashi, Takayuki Matsubara, Yoshinao Murata, **Shafira Zahra**, Naohiro Hozumi, "Space Charge Measurement of Full-size 23-mm-thick XLPE Cables in Load Cycle Condition," International Symposium on HVDC Cable Systems Jicable HVDC'21, 2021.

6. **Shafira Zahra**, Masaki Utagawa, Tomohiro Kawashima, Yoshinobu Murakami, Naohiro Hozumi, Peter Morshuis, Young-Il Cho, and Yoon-Hyoung Kim, "Two-dimensional Space Charge

Measurement of Scaled Cable Joint Model," 2022 IEEE 4th International Conference on Dielectrics (ICD), Palermo, Italy, pp. 74-77, 2022.

7. **Shafira Zahra,** Masaki Utagawa, Tomohiro Kawashima, Yoshinobu Murakami, Naohiro Hozumi, Peter Morshuis, Cho Young-Il and Kim Yoon-Hyoung, "Two-Dimensional Space Charge Measurement of Scaled Cable Joint Model and Signal Compensation," 2023 International Symposium on Electrical Insulating Materials (ISEIM), Shimane, Japan, pp. 1-4, 2023. (Chapter 6).

8. **Shafira Zahra,** Tomohiro Kawashima, Yoshinobu Murakami and Naohiro Hozumi, "Insulation Conditions Assessment Using Time Series Analysis of Partial Discharge Waveform Characteristics," 2024 IEEE 14th International Conference on the Properties and Applications of Dielectric Materials (ICPADM), Phuket, Thailand, pp. 1-4, 2024.

9. **Shafira Zahra**, Tomohiro Kawashima, Yoshinobu Murakami, Naohiro Hozumi, Peter Morshuis, Young-Il Cho and Yoon-Hyoung Kim, "Sound Field Analysis on a 16-Channel Device for Measuring Space Charge in Cable Joint," 2024 10th International Conference on Condition Monitoring and Diagnosis (CMD), Gangneung, Republic of Korea, pp. 712-715, 2024.

10. **Shafira Zahra**, Shosuke Morita, Tomohiro Kawashima, Yoshinobu Murakami, Naohiro Hozumi, "Pulse Voltage Application in Space Charge Measurement for Full Size Cable Using Pulsed-Electroacoustic Method," 24th International Symposium on High Voltage Engineering, Nagano, Japan, 2025. (Chapter 4)

DOMESTIC CONFERENCE

1. 穂積直裕, **Shafira Zahra**, 川島朋裕, 村上義信, "絶縁性音響結合媒体を使用した電力ケーブルの新しい空間電荷測定手法と校正法,"電気学会研究会資料 誘電･絶縁材料/電線・ケーブル合同研究会, DEI-19-091〜106/EWC-19-020〜037, pp.69-72, 2019.

2. 李暁欣, **Shafira Zahra**, 川島朋裕, 村上義信, 穂積直裕, "空間電荷計測のためのロックイン較正法," 令和 2 年度 電気・電子・情報関係学会東海支部連合大会 講演論文集, No.B3-1, p.1, 2020

3. **Shafira Zahra**, 歌川真生, 川島朋裕, 村上義信, 穂積直裕, Peter Morshuis, Cho Young-Il, Kim Yoon-Hyoung, "Two-dimensional Space Charge Measurement of Scaled Cable Joint Model Using Scanning Acoustic Sensors and Electrically Insulating Acoustic Coupler," 電気学会研究会資料 誘電・絶縁材料/電線・ケーブル合同研究会, DEI21052, pp.13-16, 2021.

4. 李暁欣, **Shafira Zahra**, 歌川真生, 川島朋裕, 村上義信, 穂積直裕, "厚い絶縁材料のための空間電荷測定システム,"第 52 回 電気電子絶縁材料システムシンポジウム予稿集, No.MVP-19, pp.198-200, 2021.

5. **Shafira Zahra**, 歌川真生, 川島朋裕, 村上義信, 穂積直裕, "直流ケーブル接続箱縮小モデルの二次元空間電荷計測の検討,"令和 3 年電気学会全国大会 講演論文集, No.2-033, p.35, 2021.

6. 歌川真生，李暁欣，**Shafira Zahra**，矢田啓悟，川島朋裕，村上義信，穂積直裕，“空間電荷計測におけるロックイン較正法の成立条件に関する基礎検討,”第 52 回 電気電子絶縁材料システムシンポジウム予稿集, No.MVP-16, pp.186-189, 2021.

7. 歌川真生，李暁欣，**Shafira Zahra**，矢田啓悟，川島朋裕，村上義信，穂積直裕，“パルス静電応力法を用いた空間電荷計測におけるロックイン較正法の基礎検討,”令和 3 年 電気学会基礎・材料共通部門大会, No.2-D, p2-5, 2021.

8. Xiaoxin Li，**Shafira Zahra**，歌川真生，川島朋裕，村上義信，穂積直裕，“Space Charge Measurement System for Thick Insulating Materials,”電気学会研究会資料 誘電・絶縁材料研究会, DEI21072, pp.1-6, 2021.

9. 森田翔亮，布施則一，高橋俊裕，松原貴幸，村田義直，**Shafira Zahra**, 穂積直裕，“様々な温度 条件下における実規模厚肉ケーブルの空間電荷測定,”誘電・絶縁材料/電線・ケーブル合同研 究会, DEI-21-084 EWC-21-022 , pp. 25-30, 2021.

10. **Shafira Zahra**，川島朋裕，村上義信，穂積直裕，“多要素電極系を用いた絶縁破壊試験の簡素化と,劣化量を介した Weibull 解析,” 誘電・絶縁材料研究会/電線・ケ-ブル研究会, DEI-25-067-078/EWC-25-005-016, pp.45-48, 2025.